To the Graduate Council:
I am submitting herewith a dissertation written by Jakob D. Brisby entitled "Feasibility of Using Triton for an Aerogravity Assist." I have examined the final paper copy of this dissertation for form and content and recommend that it be accepted in partial fulfillment of the requirements for the degree of Doctor of Philosophy, with a major in Aerospace Engineering.

_____
Trevor Moeller, Major Professor

We have read this dissertation
and recommend its acceptance:

_____
Trevor Moeller

_____
Evans Lyne

_____
Zhili Zhang

_____
David Icove

Accepted for the Council:

_____
Marieke Van Puymbroeck
Vice Provost and Dean of the Graduate School

To the Graduate Council:
I am submitting herewith a dissertation written by Jakob D. Brisby entitled "Feasibility of Using Triton for an Aerogravity Assist." I have examined the final electronic copy of this dissertation for form and content and recommend that it be accepted in partial fulfillment of the requirements for the degree of Doctor of Philosophy, with a major in Aerospace Engineering.

Trevor Moeller, Major Professor

We have read this dissertation
and recommend its acceptance:

Trevor Moeller

Evans Lyne

Zhili Zhang

David Icove

Accepted for the Council:

Marieke Van Puymbroeck

Vice Provost and Dean of the Graduate School

(Original signatures are on file with official student records.)

Feasibility of Using Triton for an Aerogravity Assist

A Dissertation Presented for the

Doctor of Philosophy

Degree

The University of Tennessee, Knoxville

Jakob D. Brisby

August 2025

© by Jakob D. Brisby, 2025
All Rights Reserved.

To Maddie and Knox

Acknowledgements

First, I'd like to thank my advisor Dr. Evans Lyne who convinced me to continue pursuing my degree after unforeseen circumstances dictated a change in my plans. Without your invaluable mentorship and your continual encouragement I would have easily decided to drop out. Next, I'd like to thank Dr. Trevor Moeller for being a co-chair and Dr. Zhili Zhang and Dr. David Icove for agreeing to form the remainder of my committee.

I'd also like to thank my friends and colleagues at Applied Research Associates who allowed me to work remotely and provide a flexible work schedule so that I could juggle the workload while returning to graduate school. The continued push to develop simulation capabilities at work gave me familiarity with coding that proved to be a valuable asset when I needed to develop my own atmospheric trajectory program.

Next, I'd like to thank my family who always encouraged me to keep pushing forward even when life seemed to overwhelm. Most of all, I would like to thank Samantha Murrell for putting up with me and keeping me (somewhat) sane while working at least full time and pursuing my Ph.D. It has been a chaotic and stressful return to graduate school and I would not have made it through without you.

Abstract

Analysis of using Triton as a viable target for aerogravity assist maneuvers has not previously been thoroughly explored. The current research provides detailed analysis to determine vehicle configurations and atmospheric entry conditions that could allow for successful aerogravity assist at Triton to capture into orbit about Neptune. Simulated trajectories of inflatable decelerators capable of producing lift were used to estimate vehicle conditions departing Triton. Typical high-thrust, interplanetary trajectories yield Triton atmospheric entry velocities in the range of 3 km/s to 13 km/s. Using these entry velocities numerical simulations were conducted for a vehicle similar to the aeroshell in the LOFTID test. Results from the simulations include parameter sweeps of entry conditions for a number of atmospheric flight scenarios including ballistic, lifting, maneuvering, and jettisoning. Although tenuous, Triton's atmosphere does provide enough energy dissipation and aerodynamic control for selected scenarios to perform an aerogravity maneuver without violating the overall heating constraints on the vehicle or penetrating too deeply into the atmosphere. However, the calculated peak corridor widths are only about 0.48° , requiring further investigation to widen the corridor and confirm feasibility.

Table of Contents

1 Introduction **1**

1.1 Dissertation Layout 1

1.2 Goals of this Research 2

1.3 Motivation 2

2 Background **4**

2.1 Previous Work 7

2.2 Setup and Scoping 9

3 Triton Properties **15**

4 Vehicle Considerations **23**

4.1 Ballute Background 23

4.2 LOFTID Aeroshell 25

5 Methodology **28**

5.1 Simulation Setup 28

5.1.1 Triton Physical Parameters 29

5.1.2 Vehicle Initial Position and Velocity 29

5.1.3 Initial Vehicle Orientation 30

5.1.4 POST Workflow 30

5.1.5 Code Development 31

5.1.6 Aerodynamic Heating 36

6 Results **38**

6.1 Ballistic Trajectories 41

6.2 Lifting Trajectories 48

6.3 Maneuvering Trajectories 48

6.4 Jettisoning Trajectories 59

7 Conclusions **69**

Bibliography **71**

A Turn Angles **85**

A.1 Pure Gravitation Assist 85

A.2 Aerogravity Assist 86

A.2.1 2-D, Equatorial Plane 86

A.2.2 Extended to 3-D 88

B Arrival Velocity **91**

B.1 Neptune and Triton Arrival Velocities 91

C Code Workflow **94**

Vita **97**

List of Tables

3.1 Physical Properties 16

3.2 Surface pressures on Triton 19

3.3 Atmospheric Comparisons 19

4.1 LOFTID Vehicle Parameters 27

6.1 Range of Entry Conditions 41

B.1 Probe Velocities at Arrival to Neptune System With Respect to Neptune 92

B.2 Probe Velocities at Arrival to Neptune System With Respect to Triton 92

List of Figures

2.1 Simplified diagram of a 2D, equatorial aerocapture maneuver. 5
2.2 Simplified diagram of a 2D, equatorial aerogravity assist maneuver. . 6
2.3 Diagram displaying the boundaries that define an entry corridor. . . . 6
2.4 Left: Range of characteristic energy (C_3) needed to enter into the transfer ellipse. Right: Vehicle velocity at arrival to the Neptunian system. 11
2.5 Inertial velocity along with minimum and maximum entry velocities for Neptune and Triton as a function of direct transit time. 12
2.6 Diagram of relative velocity vectors during the Triton approach. . . . 12
2.7 Post-AGA Neptune-centered velocity as a function of alignment of $V_{\infty,o}$ with Triton's velocity vector (180-ϕ). 14

3.1 Image of Triton taken by Voyager II. 16
3.2 Total Mass Density Developed from Strobel and Zhu. 20
3.3 Mass Density Developed from Strobel and Zhu compared to previous aerogravity assist study. 20
3.4 Body length required for each flow regime as a function of altitude as defined by lines of constant Kn. 22
3.5 Kn bounds for a vehicle with a 6 m diameter. 22

4.1 Diagram of the inflated LOFTID aeroshell. 26
4.2 Axial and normal force coefficients of the LOFTID RV 27

5.1 Time history plots of velocity and altitude for a vehicle entering Triton's atmosphere at 5 km/s and angle of -52.0°. Solid black lines represent the POST trajectory while the blue circles are what were produced from the newly developed code. 32
5.2 Time history plots of velocity and altitude for a vehicle entering Triton's atmosphere at 5 km/s and angle of -54.0°. Solid black lines represent the POST trajectory while the blue circles are what were produced from the newly developed code. 33
5.3 Comparison of the components of acceleration in the inertial frame for a vehicle entering Triton's atmosphere at 5 km/s and angle of -54.0°. Black lines represent the gravitational component while the blue line is the aerodynamic component. 34

6.1 Ballistic trajectory results showing outbound hyperbolic velocity, minimum altitude, and turn angle for lines of constant entry velocity and entry angle. 43
6.2 Peak heating for the ballistic trajectories. 44
6.3 Components of the potential peak heating rate in Triton's atmosphere for velocities between 3 km/s and 12 km/s above 10 km altitude. . . . 45
6.4 Change in minimum altitude as a function of ballistic coefficient for $V_{En} = 4.0$ km/s 46
6.5 Change in minimum altitude as a function of ballistic coefficient for $V_{En} = 5.0$ km/s 46
6.6 Change in minimum altitude as a function of ballistic coefficient for $V_{En} = 6.0$ km/s 47
6.7 Change in minimum altitude as a function of ballistic coefficient for $V_{En} = 7.0$ km/s 47

6.8 Non-maneuvering, full lift down trajectory results showing outbound hyperbolic velocity, minimum altitude, and turn angle for lines of constant entry velocity and entry angle. 49
6.9 Non-maneuvering, full lift up trajectory results showing outbound hyperbolic velocity, minimum altitude, and turn angle for lines of constant entry velocity and entry angle. 50
6.10 Non-maneuvering, peak heating. 51
6.11 Corridor width for a target outbound excess speed of 2.0 km/s. . . . 52
6.12 Corridor width for a target outbound excess speed of 3.0 km/s. . . . 53
6.13 Corridor width for a target outbound excess speed of 4.0 km/s. . . . 54
6.14 Corridor width for a target outbound excess speed of 5.0 km/s. . . . 55
6.15 Corridor width for a target outbound excess speed of 6.0 km/s. . . . 56
6.16 Corridor width for a target outbound excess speed of 7.0 km/s. . . . 57
6.17 Corridor width as a function of atmospheric entry velocity for lines of constant outbound excess speed. 59
6.18 Outbound excess velocity as a function of cut time for lines of constant entry angle and entry velocities of 3 and 4 km/s. 61
6.19 Outbound excess velocity as a function of cut time for lines of constant entry angle and entry velocities of 5 and 6 km/s. 62
6.20 Outbound excess velocity as a function of cut time for lines of constant entry angle and entry velocities of 7 and 8 km/s. 63
6.21 Outbound excess velocity as a function of cut time for lines of constant entry angle and entry velocities of 9 and 10 km/s. 64
6.22 Outbound excess velocity as a function of cut time for lines of constant entry angle and entry velocities of 11 and 12 km/s. 65
6.23 Outbound excess velocity as a function of cut time for lines of constant entry velocity and entry angles of -52.0° and -53.0°. 66
6.24 Outbound excess velocity as a function of cut time for lines of constant entry velocity and entry angles of -54.0° and -55.0°. 67

6.25 Minimum altitude as a function of cut time for lines of constant entry velocity and entry angles of -52.5°and -54.0°. 68

A.1 Turn angle diagram from pure gravitational assist. 85

A.2 Contour plot of turn angle (δ) for $h = [0, 1029]\,km$ and $V_\infty = [3, 14]\,\frac{km}{s}$. 87

A.3 Turn angle diagram from aerogravity assist. 89

Nomenclature

Abbreviations

ADEPT	Adaptable Deployable Entry and Placement Technology
AGA	Aerogravity Assist
ARC	Ames Research Center
CFD	Computational Fluid Dynamics
DEV	Deployable Entry Vehicles
DSMC	Direct Simulation Monte Carlo
GNC	Guidance, Navigation, and Control
HIAD	Hypersonic Inflatable Aerodynamic Decelerator
I/O	Input/Output
IRVE	Inflatable Re-Entry Vehicle Experiments
JPL	Jet Propulsion Laboratory
LaRC	Langley Research Center
LOFTID	Low-Earth Orbit Flight Test of an Inflatable Decelerator
MAnE	Mission Analysis Environment

MHD	Magnetohydrodynamics
MSFC	Marshall Space Flight Center
NAIF	Navigation and Ancillary Information Facility
NASA	Nation Aeronautics and Space Administration
POST	Program to Optimize Simulated Trajectories
RSS	Radio Science System
RV	Re-Entry Vehicle
SEP	Solar Electric Propulsion
SPICE	Spacecraft Planet Instrument Camera-matrix Events
TCW	Theoretical Corridor Width
TPS	Thermal Protection System
ULA	United Launch Alliance
UVS	Ultraviolet Spectrum
VTM	Volatile Transport Modeling

Variables

α	Angle of attack
β	Bank angle
δ	Turn angle of probe's excess velocity vector
ΔV	Change in velocity
$\dot{\vec{R}}_I$	Derivative of probe's radial distance from planet's center
$\dot{\vec{V}}_I$	Derivative of probe's velocity
$\dot{q}_c$	Stagnation point convective heating rate
γ_{En}	Atmospheric entry angle
γ_I	Inertial flight path angle
λ	Mean free path
μ_N	Neptune gravitational parameter
μ_{Tr}	Triton gravitational parameter
$\nu_{\infty,i}$	Inbound true anomaly
$\nu_{\infty,o}$	Outbound true anomaly
ϕ	Angle between Triton velocity vector and probe velocity vector at departure
ϕ_c	Geocentric latitude
ψ	Central angle between longitude at atmospheric entry and longitude at atmospheric exit
ρ_∞	Freestream density

ρ_{Surf}	Atmospheric density at the surface
θ_{En}	Longitude at atmospheric entry
θ_{Ex}	Longitude at atmospheric exit
θ_I	Inertial longitude
θ_i	Angle between Triton velocity vector and probe velocity vector at arrival
$\vec{A_B}$	Vehicle acceleration from aerodynamic forces in the body frame
$\vec{A_I}$	Vehicle acceleration from aerodynamic forces
$\vec{F_I}$	Aerodynamic forces
$\vec{G_I}$	Vehicle acceleration from gravitational forces
$\vec{R_I}$	Probe's initial radial distance from planet's center
$\vec{V_I}$	Probe's initial velocity
Az_I	Inertial azimuthal angle
A	Vehicle reference area
AU	Astronomical Unit
BC	Ballistic coefficient
C_3	Characteristic energy
C_A	Coefficient of axial force
C_D	Coefficient of drag force
C_L	Coefficient of lift force

C_N	Coefficient of normal force
C_Y	Coefficient of yaw
D	Drag force
d	Molecular diameter
H_{Atmo}	Atmoshperic height
J	Non-spherical gravity coefficient
k	Atmospheric dependent heat-transfer coefficient
Kn	Knudsen Number
L	Lift force
l	Characteristic length
m_{veh}	Vehicle mass
n	Number density
P_{Surf}	Atmospheric pressure at the surface
$R_{P,in}$	Inbound periapse radius
$R_{P,out}$	Outbound periapse radius
R_P	Periapse radius
R_{Tr}	Triton orbital radius
V	Velocity
$V_{@R_N,Eq}$	Inertial velocity at Neptune atmospheric interface
$V_{\infty,@N}$	Arrival velocity with respect to Neptune

$V_{\infty,@Tr}$	Arrival velocity with respect to Triton
$V_{\infty,in}$	Inbound hyperbolic velocity
$V_{\infty,Max}$	Probe arrival velocity at Triton when moving in the opposite direction as Triton
$V_{\infty,Min}$	Probe arrival velocity at Triton when moving in the same direction as Triton
$V_{\infty,out}$	Outbound hyperbolic velocity
V_{En}	Atmospheric entry velocity
V_{Esc}	Escape velocity
$V_{Max@Atmo,En}$	Probe velocity at Neptune atmospheric entry in the opposite direction as the rotating atmosphere
$V_{Min@Atmo,En}$	Probe velocity at Neptune atmospheric entry in the same direction as the rotating atmosphere
$V_{N,Rotation}$	Neptune rotational velocity
V_{Orb}	Orbital velocity
$V_{P,i}$	Neptune centric probe velocity pre-AGA
$V_{P,o}$	Neptune centric probe velocity post-AGA
V_{Tr}	Triton orbital velocity

Chapter 1

Introduction

1.1 Dissertation Layout

The current chapter, Chapter 1, will discuss the goals and motivation for this research. This will include highlights from a few previous works that provide some background as to how the overall idea was formulated. This will be followed immediately by Chapter 2 section whose purpose is to describe how an AGA differs from other maneuvers, provide more detailed information on the previous works that led to the decisions for pursuing the current research, and present preliminary research that was used to find the most favorable conditions for enabling the Triton AGA maneuver. Next, Chapter 3 will focus on the physical properties of Triton and data used to define its atmospheric profile because the feasibility of the aerogravity assist maneuver is wholly dependent on an accurate, up-to-date, atmospheric model. Chapter 4 will provide an overview of vehicles considered for this study including blunt body re-entry capsules and high-speed decelerators. Chapter 5 will cover how the trajectories were simulated. This will include off-the-shelf software used and development of my own atmospheric trajectory code. Next, Chapter 6 will discuss results for the various types of trajectories that were simulated. Chapter 7 will give final thoughts of the feasibility of of using Triton for the focus of an aerogravity assist and the potential for future

work. Readers can also find more discussion of turn angles, arrival velocities, and equations used for development of the atmospheric trajectory code in the Appendix.

1.2 Goals of this Research

The objective of this project is to determine the feasibility of using Triton to perform an aerogravity assist (AGA) to capture a spacecraft into orbit about Neptune. This maneuver combines a 'gravitational slingshot' with aerodynamic forces to alter the vehicle's trajectory. Drag forces allow the vehicle to reduce its velocity by dissipating energy; if the vehicle is capable of producing lift, it can also adjust its heading using lift to augment the turn produced by gravity alone. It is expected that if such a maneuver is found to be possible, the strategy could be used to deliver more mass into an orbit about Neptune than could be achieved using a propulsive orbital insertion or a Neptune aerocapture.

1.3 Motivation

The Neptune system has long been considered a high-priority candidate for further exploration, having been visited only once during the 1989 flyby of Voyager II. Although not selected, there have been recent proposals made for Discovery[1] and Flagship[2] class missions to Neptune system. Due to Neptune's distance being 30 AU from Earth, missions targeting the Neptune system suffer from a combination of excessive flight times (on the order of decades) and high energy requirements. In order to make missions to the Neptune system more desirable, it is necessary to minimize flight time while capturing into orbit using as little propellant as possible.

Aerocapture, the use of aerodynamic drag to capture an inbound spacecraft at a target planet, has long been considered as a means to substantially reduce the propellant requirements for orbital insertion. Benefits of using aerocapture for orbital insertion has been the focus of many trade studies for mission architectures targeting

a variety of planets, including the Neptune system[3–10]. Studies conducted in 2004[3, 5] estimated that missions to Neptune could deliver 1.4 times the amount of mass into orbit when an aerocapture is used compared to a traditional propulsive-only insertion. In the 20 years since those studies technological advances could even increase the effectiveness of aerocapture.

However, it is the author's belief that Triton provides a unique opportunity to employ an AGA which could rival, or even out-perform, the effectiveness of a Neptunian aerocapture. Due to Triton's nearly retrograde orbit, aerocapture using Neptune's atmosphere into an orbit well-suited for subsequent manipulation via Triton flybys requires an entry opposite to the direction of Neptune's rotation, resulting in atmosphere-relative entry speeds of 28 km/s to 32 km/s. This results in a far more severe aerothermal environment than entries in the same direction as Neptune's rotation, where atmospheric entry velocities range from 23 km/s to 26 km/s[7].

Preliminary studies[11, 12] revealed that Triton's very tenuous atmosphere would not provide enough energy dissipation for an AGA using vehicles with high ballistic coefficients (capsules). However, the study suggested the maneuver is possible when combined with trailing inflatable drag devices known as ballutes. These studies concluded by suggesting future research should include "low ballistic coefficient aeroshells, such as those with inflatable skirts"[12] which are preferable to trailing ballutes. In late 2022, an aeroshell matching this description was successfully flight tested by NASA and was called the Low-Earth Orbit Flight Test of an Inflatable Decelerator (LOFTID). The LOFTID aeroshell is the platform which the current study will use to perform an analysis of the feasibility of an AGA at Triton to capture a spacecraft into orbit about Neptune.

Chapter 2

Background

Large amounts of energy are required to reach planets in the outer solar system. As a consequence, vehicles propelled through traditional high-thrust boosters are going to have high excess velocities upon arrival. Capturing into stable orbits at these bodies requires a spacecraft to adjust its velocity vector typically through propulsive ΔV maneuvers. Another way for a spacecraft to alter its velocity vector is by plunging into a planet's atmosphere and leveraging the vehicle's aerodynamics. However, these atmospheric maneuvers are still only theoretical and have never been attempted during actual missions.

Three techniques to leverage aerodynamics during mission planning are referred to as aerobraking, aerocapture, and aerogravity assist. Aerobraking is slightly different than the other two because a spacecraft performs an aerobrake after it has already been captured into orbit. The purpose of an aerobrake maneuver is to adjust its orbit by reducing its energy through drag forces, thereby lowering its apoapsis altitude. Aerocapture and aerogravity assist (AGA) are performed when the spacecraft is still on its hyperbolic trajectory. Aerocapture is the correct term for using the atmosphere of the capturing planet to dissipate enough energy so the spacecraft is no longer in a hyperbolic trajectory but in an elliptical orbit. Aerogravity assist is the focus of the current work and is coined for a maneuver that uses the gravitational well and

atmosphere of some celestial body but allows the spacecraft to maintain a hyperbolic trajectory with respect to the assisting body. Simplified diagrams displaying the differences between aerocapture and aerogravity assist can be seen in Fig. 2.1 and Fig. 2.2.

When performing an AGA it is necessary to define a theoretical corridor width (TCW). Finding this corridor width requires defining a set of entry conditions that will provide a suitable outbound trajectory. In addition, the atmospheric flight will typically have other constraints to ensure the survivability of the vehicle such as a minimum altitude limit and structural loading and heating from the aerodynamics. It is reasonable to be conservative with minimum altitude limit to avoid impacting the planetary surface or unknown geologic features since detailed topography may be unavailable prior to arrival. Because the atmospheric trajectories happen at high velocities aerodynamic heating is also a concern. The edges of the entry corridor are known as the overshoot and undershoot boundaries and are displayed in Fig. 2.3.

The overshoot boundary is simply defined as the shallowest entry angle needed to achieve the desired outbound conditions. This boundary can be found by flying the

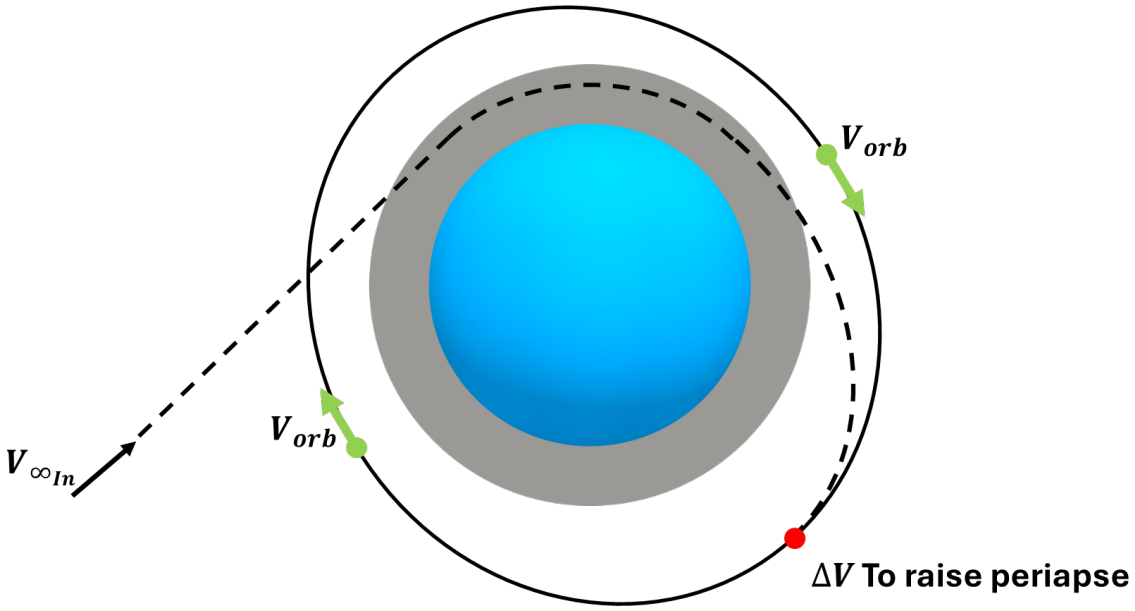


Figure 2.1: Simplified diagram of a 2D, equatorial aerocapture maneuver.

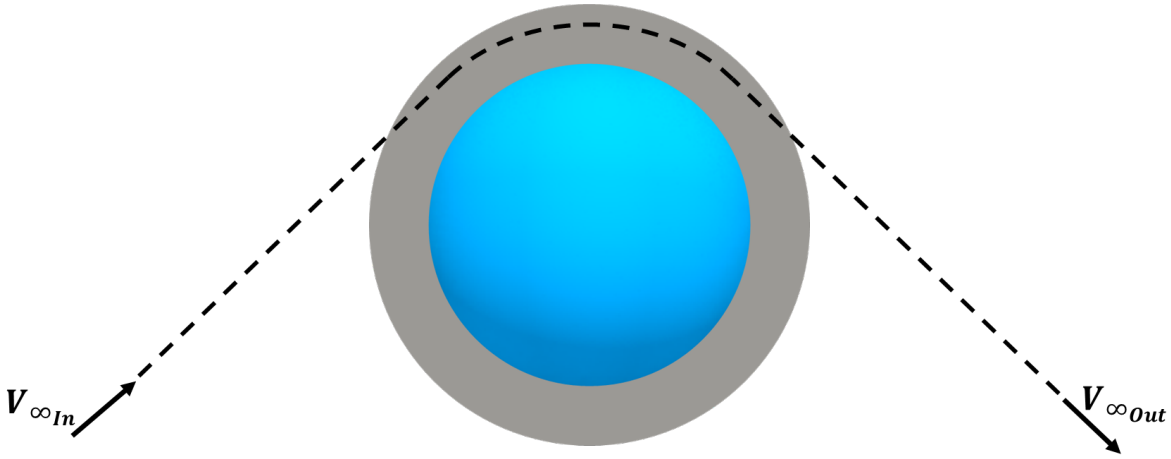


Figure 2.2: Simplified diagram of a 2D, equatorial aerogravity assist maneuver.

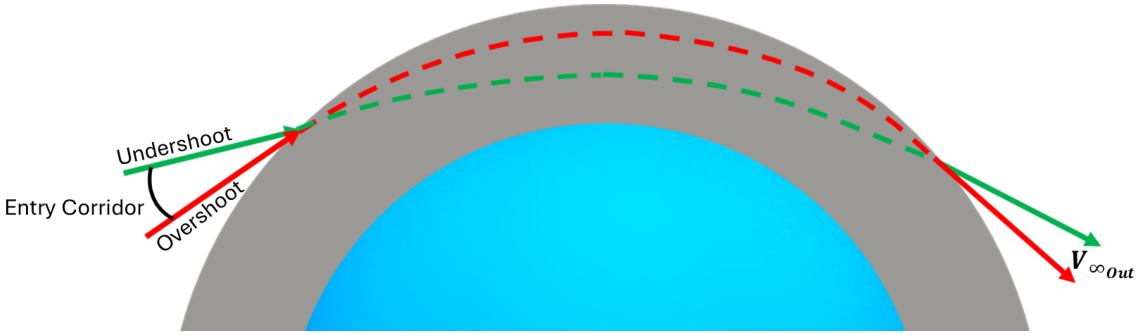


Figure 2.3: Diagram displaying the boundaries that define an entry corridor.

vehicle at an angle of attack, generating lift. However, this must be done at a bank angle of 180°, pointing the direction of the lift vector towards the planetary surface.

The undershoot boundary is the steepest allowable entry angle that can be flown while staying within the previously mentioned altitude, heating, and deceleration constraints. Initially, the undershoot boundary can be found by flying the vehicle at full lift-up orientation. The undershoot can also be varied by allowing the vehicle to maneuver under certain conditions. During the atmospheric trajectory if the vehicle hasn't dissipated enough energy to meet the desired outbound conditions, it may be necessary to perform some maneuver that will allow further energy reduction. While the vehicle is flying at maximum lift it may bank the lift vector about its relative velocity vector to maintain magnitude of the lift vector but change its direction. As long as the vehicle stays above the minimum altitude limit and below the aerodynamic heating and structural loading limits, any number of these maneuvers can be completed to stay low in the atmosphere and dissipate enough energy to meet the desired outbound conditions.

2.1 Previous Work

Benefits of using an aerocapture for orbital insertion has been the focus of many trade studies for mission architecture. One such study by Hall et. al.[3] looked at orbital insertion for missions to Venus, Mars, Jupiter, Saturn, Titan, Uranus, and Neptune. The cost of orbital insertion via chemical propulsion was compared to aerobraking and aerocapture maneuvers. For the majority of mission designs studied aerocapture was shown to enhance the mission by increasing the deliverable mass and decreasing transit time. A few missions to Jupiter, Saturn, Titan, Uranus, and Neptune were even shown to only be achievable through aerocapture. However, the study also concluded that there are instances, although very few, where aerocapture delivers less mass to the target than propulsive orbital insertion. This happens to be the case when the required ΔV for inserting to the parking orbit is low but the

atmospheric entry velocity is high. This means the mass savings gained by decreasing the propulsive ΔV requirements must go to bolstering the thermal protection system (TPS) because the aerodynamic heating will be more severe.

An early trade study by Noca and Bailey[4] compared transfers to Neptune using combinations of chemical propulsion, solar electric propulsion (SEP), gravitational fly-bys, and aerocapture using either the Delta IV H or Atlas 551. Noca and Bailey[4] demonstrated how the flight times can be reduced by combining different methods but the methods result in large C_3 values and high inertial entry velocities at Neptune. C_3, also referred to as the characteristic energy, is a term commonly used to represent the amount of energy needed to enter into an interplanetary transfer ellipse[13]. The most favorable scenario they reached for the Delta IV H was using SEP for the Earth-to-Neptune transfer orbit with an aerocapture at Neptune. The cruise time to Neptune was 10.2 years, inertial entry velocity of 29 km/s, and an orbital payload mass of 790 kg.

A companion study on the aerocapture system was presented by Lockwood[5] and focused on designing an aeroshell that could successfully complete a mission when considering a variety of factors including flight time to Neptune, net mass delivered, entry velocity, aerodynamic requirements (L/D, TCW), and aeroheating. The study was a multi-disciplinary effort involving NASA staff from Ames Research Center (ARC), the Jet Propulsion Laboratory (JPL), Johnson Space Center (JSC), Marshall Space Flight Center (MSFC), and led by Langley Research Center (LaRC). This study was able to design a mission architecture using an aeroshell with a mass fraction around 40-45% for the aerocapture as opposed to nearly 60% for a traditional propulsive orbital insertion. Ultimately, using aerocapture was shown to be capable of delivering 40% more mass into orbit about Neptune than similar launch vehicle that uses only propulsion systems[5].

More recent studies conducted by Girija et al.[9, 10] present results of a thorough analyses of aerocapture at Neptune to include an orbit sufficient to conduct scientific observations on Triton. The analysis included aerodynamic, GNC, heat loading

considerations, and suggests a hybrid propulsive-aerocapture at Neptune, and using a pathfinder probe sent ahead of the main vehicle by several weeks to transmit atmospheric data before the main vehicle reaches its aerocapture intercept point.

In 2004, Ramsey and Lyne[11, 12] proposed using an aerogravity assist (AGA) at Triton to capture a spacecraft into orbit about Neptune. The use of a Triton AGA instead of a direct aerocapture in Neptune's atmosphere would greatly reduce the atmospheric entry speed, since the spacecraft would not enter as deeply into Neptune's gravity well and could be traveling roughly in the same direction as Triton's motion. This same method was proposed for use at Titan for orbital capture about Saturn at least as early as 1990[14]. Numerous studies since that time have explored the concept more fully for the Saturn system, evaluating guidance and control, aerothermal heating, and other issues[7, 11, 12, 14–20]. Because of its high atmospheric density coupled with a large-scale height and weak gravitational field, Titan is an ideal location for such a maneuver, and studies have indicated that low L/D, capsule-type configurations would likely be sufficient.

Triton, however, has an atmospheric density four orders of magnitude lower than Titan, making a successful AGA much more challenging. Largely as a result of this low atmospheric density, previous work[11, 12, 15] indicated that a capsule would probably not be sufficient but a probe tethered to an inflatable drag device known as a ballute might execute the maneuver successfully.

2.2 Setup and Scoping

It was important to understand the range of potential arrival conditions to the Neptunian system to find reasonable input values for the Triton atmospheric simulations and constrain the output values that were needed. A Hohmann transfer was used to define the slowest arrival conditions. Since the Hohmann transfer uses the smallest ΔV to transfer between coplanar orbits it also means long flight times.

This type of transfer from Earth to Neptune yields an arrival V_∞ of approximately 4.1 km/s and a flight time of about 30 years.

With this in mind, fellow graduate student, Allison Carroll, was able to generate some preliminary trajectories using a software called Mission Analysis Environment, or MAnE[21]. MAnE is well-suited to for high-level interplanetary mission design due to its ease of use and ability to optimize trajectories based on user defined constraints. These constraints include various departure and arrival conditions, flight times, and even deep space maneuvers. However, when determining the heliocentric trajectory the models utilize a patched-conic approach assuming only a heliocentric gravitational component [22]. A caveat to this is when a propulsive maneuver is required at a solar system body during the trajectory. Then the propulsive requirements and spacecraft motion are adjusted. By its own admission[22], MAnE is not well-suited to describe encounters with planetary satellites, but it can provide trajectories to the sphere of influence of said planet.

MAnE was used to generate interplanetary trajectories with flight times as low as 12 years and up to the 30 years. The arrival velocities were then used to estimate minimum and maximum atmospheric entry velocities at Neptune and Triton. The minimum entry velocities occur when the vehicle is moving in the same direction as the planet's orbital and rotational motion. Conversely, a retrograde insertion results in higher relative velocities seen by the vehicle and produces the maximum entry velocities.

Plots showing the launch energy calculated by MAnE needed to enter into the transfer ellipse along with the arrival velocity at the Neptunian system are shown in Fig. 2.4. The filled, black circles represent direct Earth to Neptune trajectories while the filled, blue diamonds represent Earth to Neptune trajectories utilizing a gravitational assist at Jupiter. Additionally, the launch dates for the 24 to 30 year direct transits were in mid to late June of 2031, the 20 and 22 year direct transits require launch dates in early to mid June of 2032, and all the Jupiter assist transits were calculated for launch dates in mid April of 2032. For the direct transit

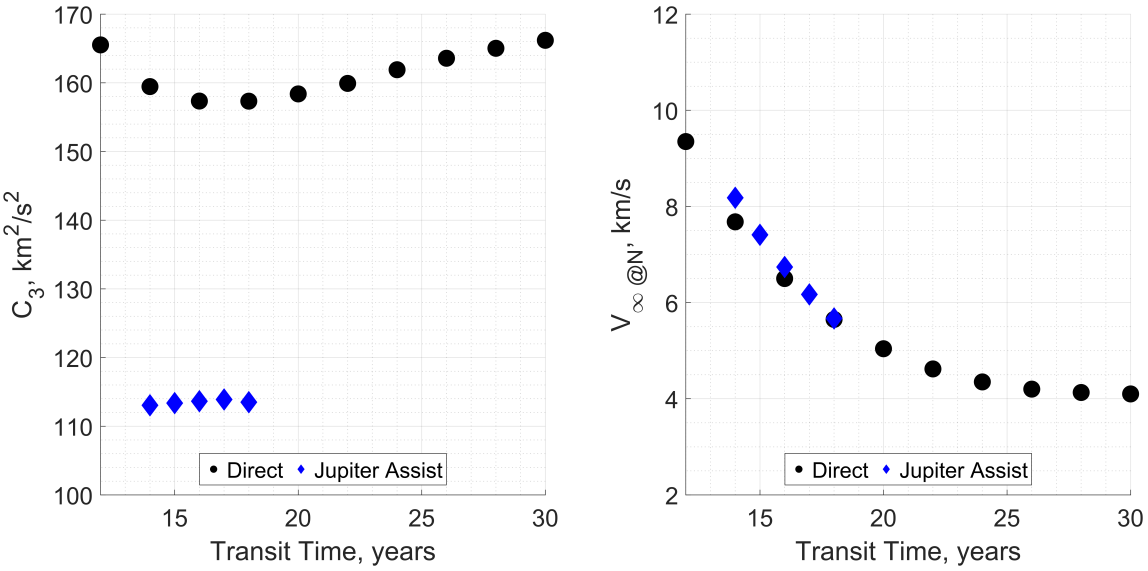


Figure 2.4: Left: Range of characteristic energy (C_3) needed to enter into the transfer ellipse. Right: Vehicle velocity at arrival to the Neptunian system.

transfer, the inertial velocity at Neptune are shown in Fig. 2.5 with the corresponding minimum and maximum entry velocities as a function of transit time.

The atmospheric entry speed at Triton depends on the probe's arrival excess speed at the Neptune system as well as the relative alignment of the probe's velocity vector and Triton's orbital motion at the time of the intercept (θ_i). The diagram shown in Fig. 2.6[23] shows relative orientations of Triton's orbital velocity vector (V_{Tr}) and the probe's velocity vectors at Triton's orbital distance before ($V_{P,i}$) and after ($V_{P,o}$) the AGA maneuver in the Neptune reference frame. The inbound and outbound hyperbolic velocity vectors in Triton's reference frame are also shown as $V_{\infty,in}$ and $V_{\infty,out}$, respectively. The probe's change in velocity from performing the AGA is labeled as ΔV and is the same in either reference frame. Prior to the AGA maneuver, the angle between Triton's velocity vector and the probe's Neptune-centric velocity vector is shown as θ_i. The turn angle achieved in the Triton reference frame is labeled as δ and is the angle between the vectors $V_{\infty,in}$ and $V_{\infty,out}$. Lastly, ϕ is shown to be the angle between Triton's velocity and the probe's outbound velocity

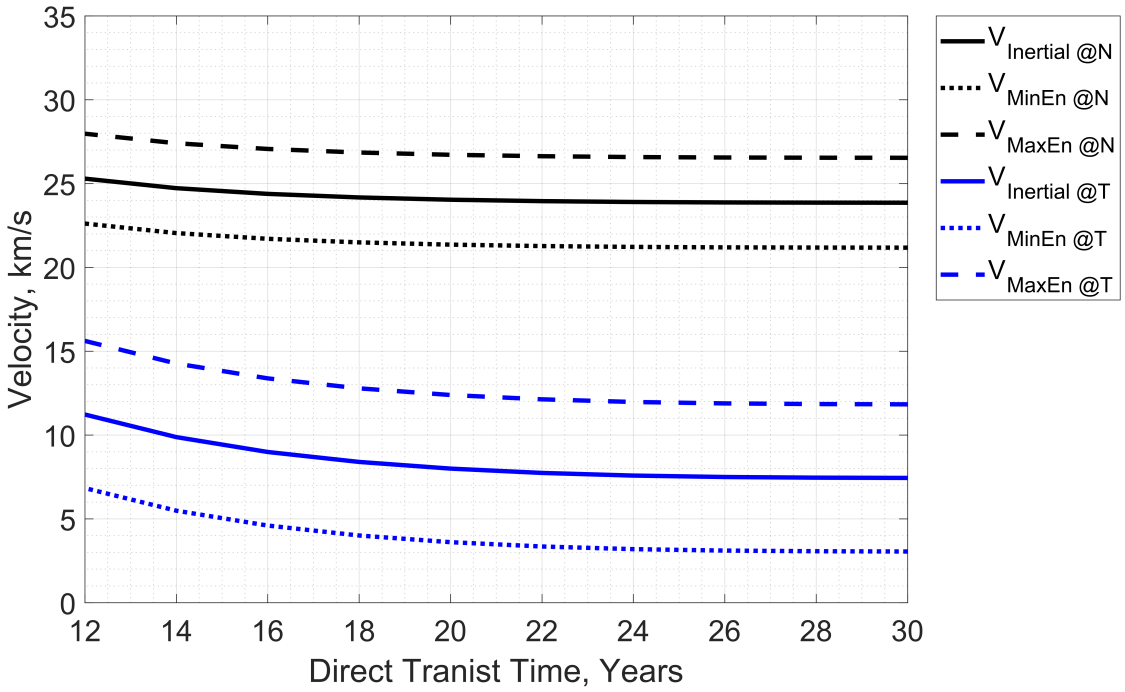


Figure 2.5: Inertial velocity along with minimum and maximum entry velocities for Neptune and Triton as a function of direct transit time.

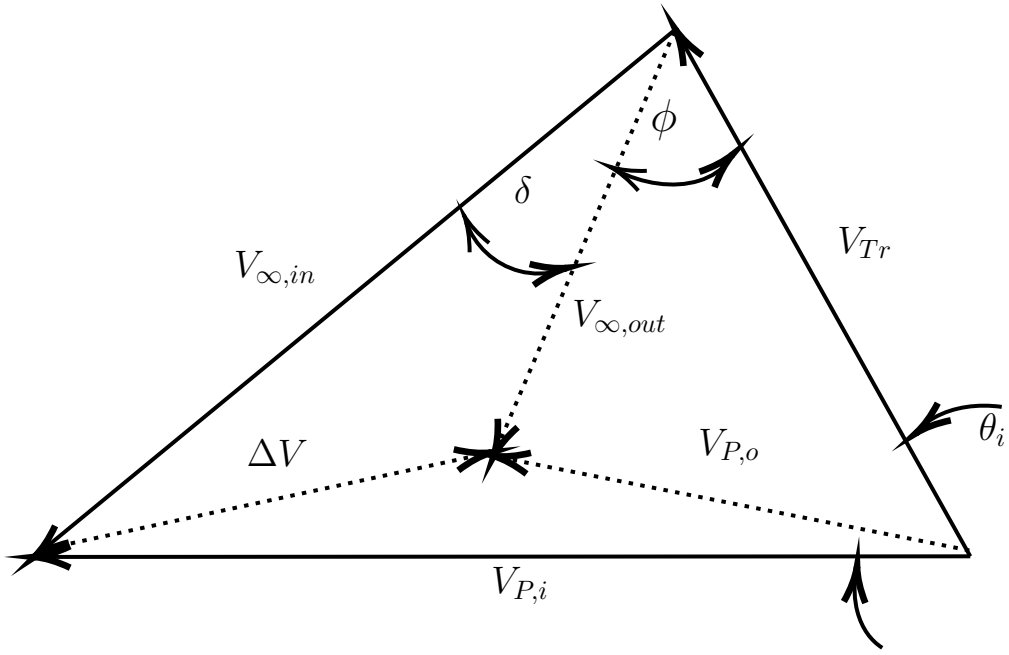


Figure 2.6: Diagram of relative velocity vectors during the Triton approach.

with respect to Triton. Discussions on calculating δ for gravitational assist with, and without, atmospheric drag can be found in Appendix A.

Based on prior studies of Neptune aerocapture in conjunction with reasonable limits on the anticipated aerothermal heating, we considered Triton atmospheric entry speeds ranging from 3.0 km/s to 14.0 km/s [5]. Hyperbolic excess speeds close to the higher end of that bounds will have a smaller window of relative angles in which a capture will happen.

We can also determine reasonable boundaries for the outbound velocity from the Triton-AGA that will capture into the Neptune system. Using Eq. 2.1, the escape velocity at Triton's orbital distance is ~6.2 km/s.

$$V_{Esc} = \sqrt{\frac{2\mu_N}{R_{Tr}}} \tag{2.1}$$

Subtracting Triton's orbital velocity of ~4.39 km/s from the escape velocity at Triton's orbital distance gives a velocity of 1.81 km/s. Any object leaving Triton with a hyperbolic excess velocity at or below 1.81 km/s will capture into the Neptune system regardless of its direction of travel. If instead, we sum Triton's orbital velocity and the escape velocity, we find a velocity of 10.59 km/s. Without further intervention, any object leaving Triton with this higher hyperbolic excess speed will never capture into the Neptune system. Any object departing Triton with a hyperbolic excess speed between 1.81 km/s and 10.59 km/s may capture into the Neptune system (again without intervention) depending on the direction it is traveling relative to Neptune. A plot showing the relative angles for capturing into Neptune's system is shown in Fig. 2.7.

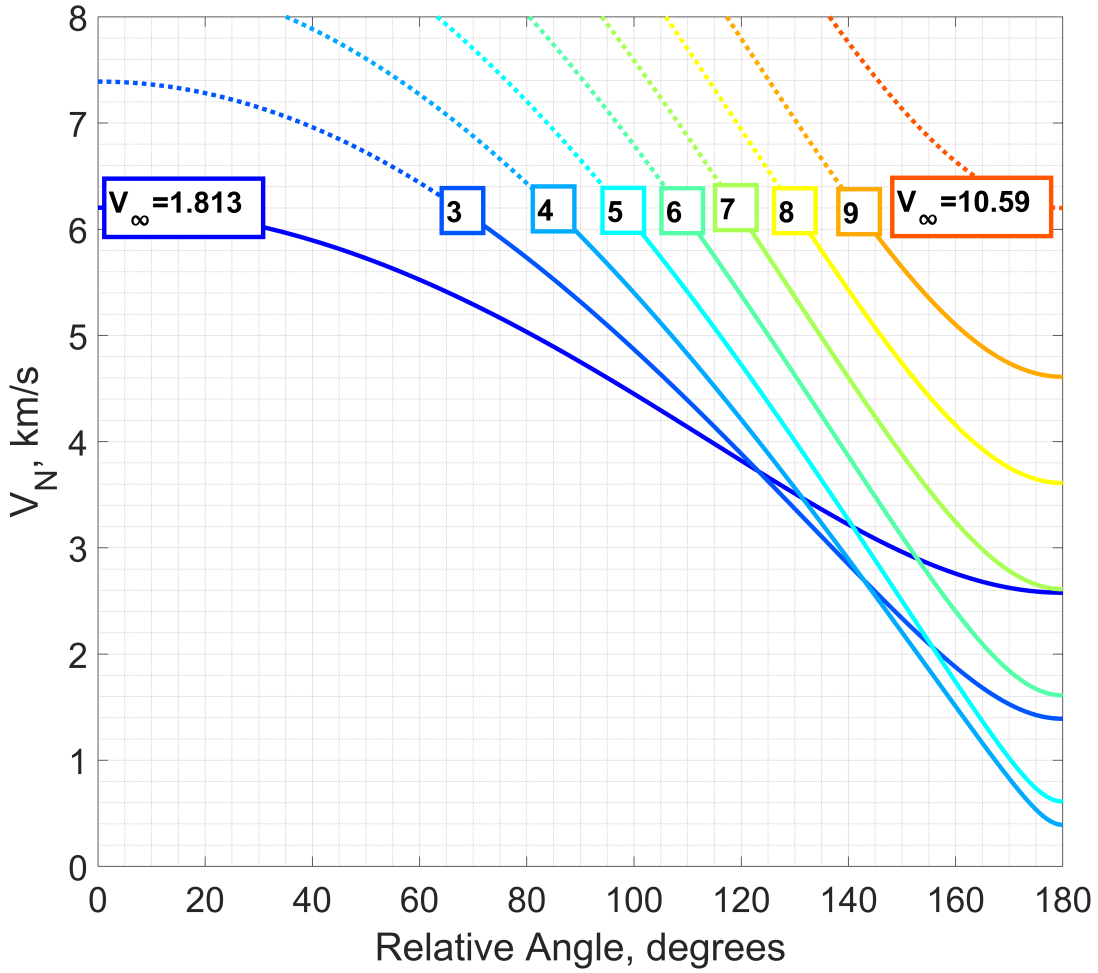


Figure 2.7: Post-AGA Neptune-centered velocity as a function of alignment of $V_{\infty,o}$ with Triton's velocity vector (180-ϕ).

Chapter 3

Triton Properties

Triton, originally discovered by William Lassell in 1846, is the largest moon orbiting Neptune and is an interesting but challenging candidate for employing an aerogravity assist maneuver. Reasons that make Triton amenable to an AGA are its nearly retrograde orbit, an atmosphere dominated by diatomic nitrogen, and a lack of prominent surface variation[24].

Due to Triton's nearly retrograde motion with respect to Neptune, the target capture orbit would need to be traveling in roughly the same direction as Triton. Lastly, minimal surface variation allows for deeper penetration into Triton's atmosphere with reduced risk of impacting protruding surface features leading to relaxed corridor width constraints. In addition, Triton is tidally locked in its orbit about Neptune with a period of about 5.87 days with an orbital velocity of 4.39 km/s. An image of Triton taken by Voyager II[25] is shown in Fig. 3.1, while other physical properties about Triton and Neptune can be found in Table 3.1.

One of the largest uncertainties about Triton is the state of its tenuous atmosphere. Due its distance from Earth (∼30 AU) Triton's atmosphere has only been observed by spacecraft once. Prior to the Voyager II flyby, all that was known about Triton's atmosphere was that it contained N_2 and CH_4 which were observed through the infrared spectrum. Voyager II passed the Neptune-Triton system on August 25, 1989

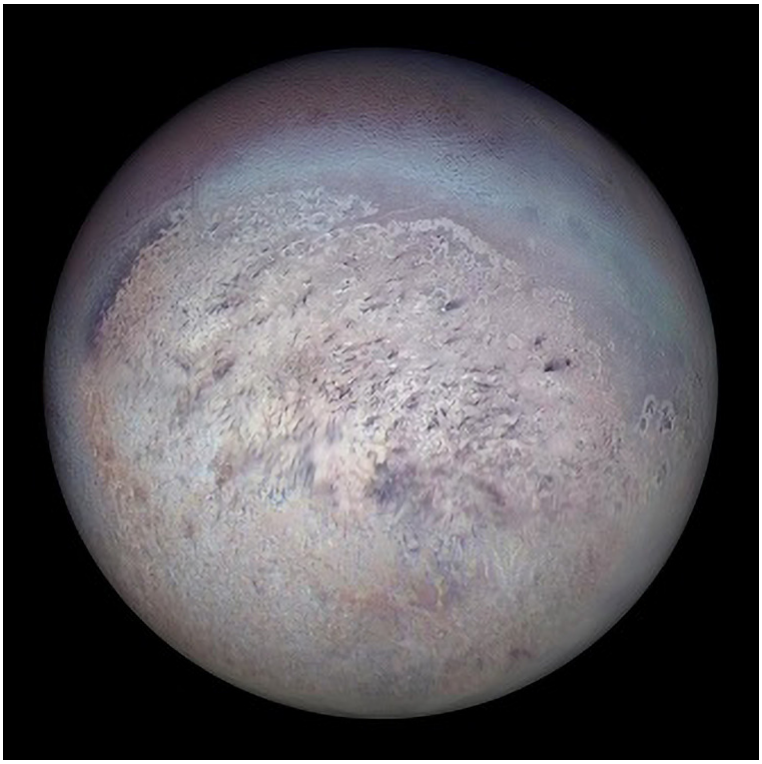


Figure 3.1: Image of Triton taken by Voyager II[25].

Table 3.1: Physical Properties

	Triton	Neptune
Focal Point	Neptune	Sun
Mass, kg	2.139E+22	1.024E+26
Radius, km	1352	24770
μ, km^3/s^2	1.428E+03	6.835E+06
Period, days	5.876E+00	6.019E+04
Distance From Focal Point, km	3.548E+05	4.496E+09
Sphere of Influence, km	1.196E+04	8.659E+07
Orbital Velocity, km/s	4.390	5.430
Escape Velocity, km/s	1.450	23.49
Orbital Eccentricity	0.0	0.0097
Inclination w.r.t. Ecliptic, degrees	129.8	1.77
Obliquity to Orbit, degrees	0.0	28.32

and captured measurements of Triton's atmosphere using its Radio Science System (RSS) [26] and Ultraviolet Spectrometer (UVS) [27]. Occultation measurements taken by the RSS and UVS made it possible to construct initial altitude profiles of temperature and number densities of N_2 and CH_4. In addition to the presence of N_2 and CH_4, Triton's atmosphere contains trace amounts of carbon monoxide and other hydrocarbons[28]. In short, an occultation happens when one body passes in front of another, blocking all of the light from the distant body. Light from the distant body is then scattered by the occulting body. Stellar occultations happen when a body passes in front of a bright star and solar occultations are when the light from our Sun is blocked. Radio occultations occur when spacecraft transmit radio signals to penetrate an atmosphere or ring system [29]. Occultation measurements can be used to reveal properties such as body size and atmospheric profiles of species abundance, temperature, pressure, and density [29, 30]. For a thorough explanation of occultation techniques for planetary atmospheres it is recommended to review the discussion by Elliot and Olkin [30]. Conditions for occultation measurements for Triton are rare. As such, there have only been a few measurements taken since the Voyager II flyby. Detailed analysis of the Voyager II measurements are reported by Broadfoot[27], Yelle[31], and Krasnopolsky[32]. A number of papers have been published detailing the results of the occultations since the Voyager II measurements [33–38]. In addition, there have been others that have attempted to use the occultation data to build numerical models of Triton's atmosphere [28, 39].

In general, it is accepted that Triton's atmosphere is very cold. The temperature at the surface is reported to be $\sim$38 K in the surface frost[27, 31, 32, 34, 40] and 50-57 K in the surface dark areas [34]. Models from Elliot[34] and Krasnopolsky[32] show a slight decrease in temperature to 37 K when increasing altitude to 10 km. Above 10 km the temperature does increase and has been reported to be approximately 102 K near an altitude of 600 km [32, 33]. Triton's atmosphere is also highly rarefied having a mass density at the surface on the order of 10^{-4} kg/m^3 which is roughly equivalent to Earth's atmospheric density at an altitude of about 66 km. The surface

pressures are also very low and have been a source of contention as indicated by the variability in reported values. Surface pressures from various studies were compiled by Oliveira et al. [37] and Bertrand et al. [41], and have been recreated in Table 3.2. Additionally, Table 3.3 shows how Triton's atmospheric composition and surface properties compare to Earth and Titan. Recent observations and volatile transport modeling (VTM)[41, 42] do not agree with the spike in surface pressures reported for the occultations that occurred in 1995 and 1997 and seem to imply a more stable atmosphere than previously believed.

The previous atmosphere model used by Ramsey and Lyne [11, 12, 15, 44] was developed using the pressure as a function of altitude presented by Elliot [45]. The current research uses an updated model based upon more recent information based on stellar occultations and computational models[28, 37, 39, 41, 46].

The density profile chosen to implement was taken from Strobel et al. [39]. The profile designated as Triton-3 was shown to provide the best agreement with observed measurements of tangential N_2 column number density [39] and was therefore chosen for this study. The digitized profile begins at an altitude of 2km and extends to ~1000 km and shows a density range of 1.34E-04 kg/m^3 to 1.1E-13 kg/m^3. Since the density spans several orders of magnitude Fig. 3.2 is shown with the x-axis on a logarithmic scale. An advantage of this density profile compared to the one used in previous Triton-AGA studies is the extended altitude. As a source of comparison, the density from Strobel [39] below 150 km altitude is plotted with the profile used previously by Ramsey and Lyne and is shown in Fig. 3.3. After quantifying the density profile it was important to characterize the possible flow regimes. This is normally calculated using the Knudsen number (Kn) shown in Eq. 3.1

$$Kn = \frac{\lambda}{l} \tag{3.1}$$

Table 3.2: Surface pressures on Triton

Date	Surface Pressure (Pa)	Reference
25-Aug-1989	1.4 ± 0.2	Gurrola [43]
14-Aug-1995	1.7 ± 0.1	Olkin et al. [33]
18-Jul-1997	$2.28\ ^{+0.54}_{-0.36}$	Elliot et al. [34], Oliveira et al. [37]
	2.68 ± 0.34	
04-Nov-1997	2.11 ± 0.02	Elliot et al. [36]
21-May-2008	$1.38\ ^{+1.24}_{-0.44}$	Oliveira [37]
05-Oct-2017	1.41 ± 0.04	Oliveira [37]

Table 3.3: Atmospheric Comparisons

Quantity	Earth	Titan	Triton
N_2	78%	97%	99.9723%
CH_4	0.0002%	3%	0.00359%
H_2	0.0001%	0.2%	0.01841%
CO_2	0.0384%	0.0010%	-
C_2H_6	0.0002%	0.002%	-
C_2H_4	0.0004%	0.0010%	-
N	-	-	0.00531%
H	-	-	0.00041%
P_{Surf} (Pa)	101325	150	1.6
ρ_{Surf} (kg/m^3)	1.225	-	1.34E-4

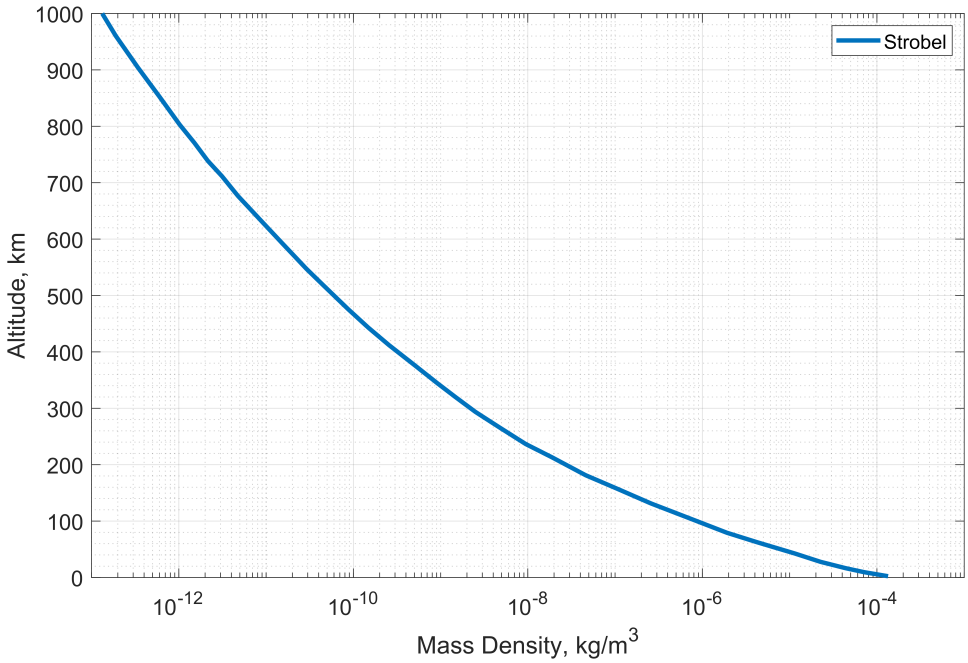


Figure 3.2: Total Mass Density Developed from Strobel and Zhu[39].

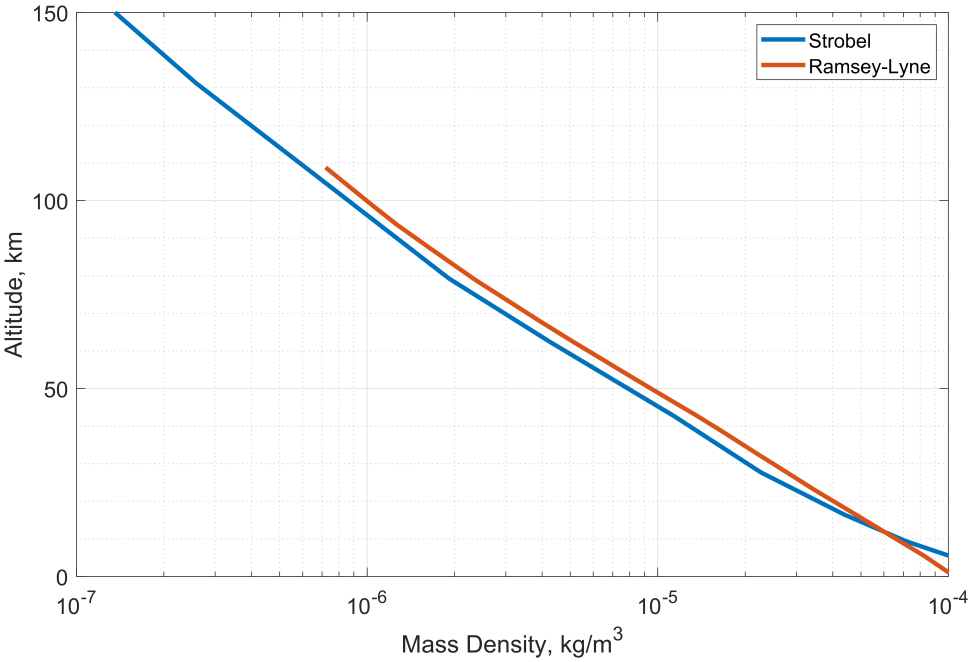


Figure 3.3: Mass Density Developed from Strobel and Zhu[39] compared to previous aerogravity assist study[11, 12, 15].

where λ is the mean free path for the collision of molecules and l is the vehicle's characteristic length. The mean free path was determined using Eq. 3.2

$$\lambda = \frac{1}{\sqrt{2}\pi d^2 n} \tag{3.2}$$

where d is the molecular diameter and n is the number density. It should also be noted that Eq. 3.2 uses the assumption of a high average velocity. Diatomic nitrogen was used to determine the parameters for the mean free path since Triton's atmosphere is more than 99.9% N_2. Because of this, d was assumed to be equal to N_2's kinetic diameter of 364E-12 m and the mass density profile was converted to number density assuming N_2's molar mass of 28 g/mol.

Instead of calculating the Kn for a given body size, Eq. 3.1 was rearranged to explore required body sizes for different Kn thresholds. Though no sharp boundaries exist between flow regimes, it is accepted that the continuum regime exists when Kn <= 0.01, continuum with slip effects when Kn > 0.01 and Kn <= 0.1, disturbed free molecular flow flow for Kn > 0.1 and Kn <= 10, and free molecular flow when Kn > 10[47]. As the Kn increases, moving from the continuum regime towards free molecular, it is necessary to include kinetic theory in the flow field considerations. Figure 3.4 shows the required body length needed for each flow regime for any given altitude. Figure 3.5 shows the calculated Kn for a LOFTID vehicle with an inflated diameter of 6 m and shows that continuum aerodynamics should be valid for a LOFTID-type vehicle at an altitude of 86 km and below.

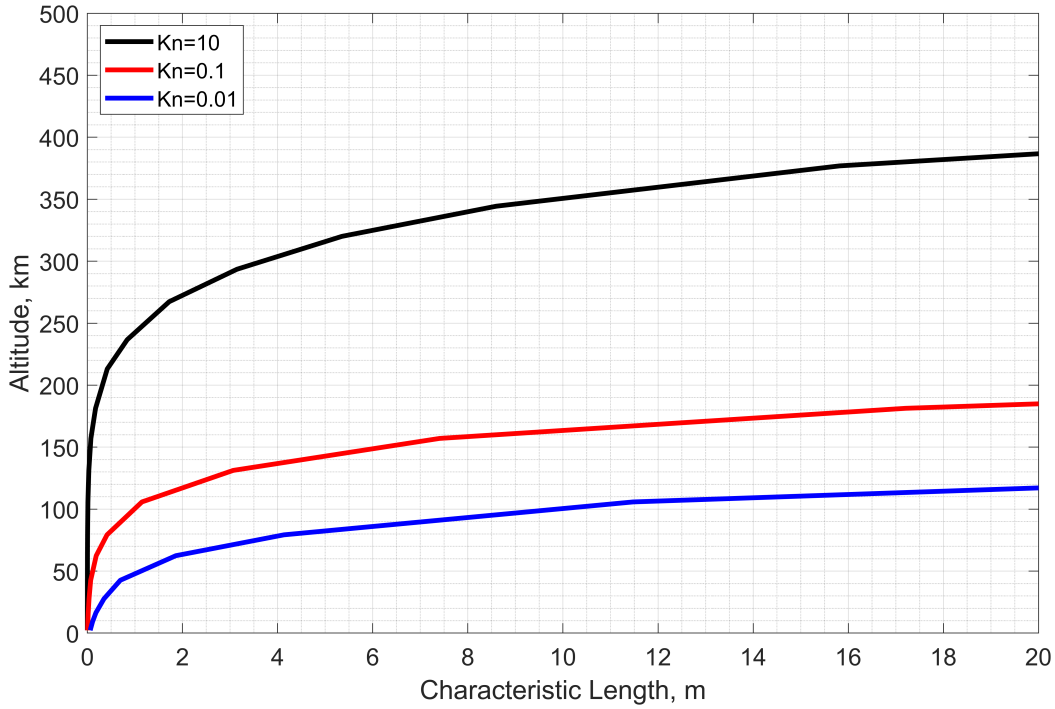


Figure 3.4: Body length required for each flow regime as a function of altitude as defined by lines of constant Kn.

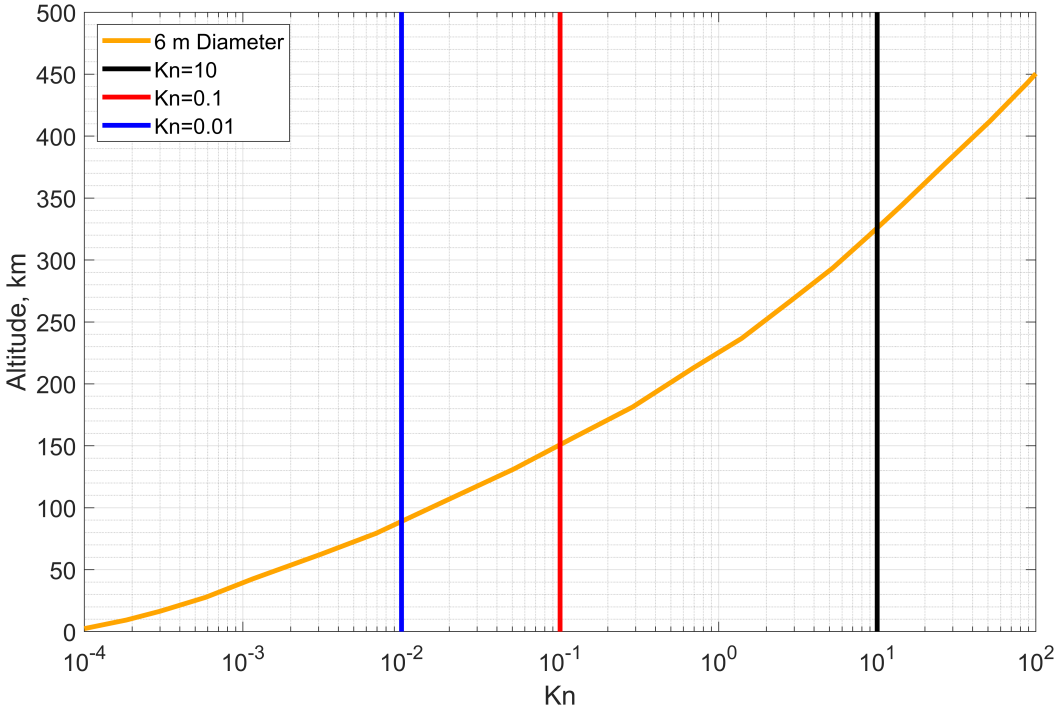


Figure 3.5: Kn bounds for a vehicle with a 6 m diameter.

Chapter 4

Vehicle Considerations

Rigid aeroshells have been the focus of space missions since man first started launching hunks of metal into outer-space and have been vital to the development of the space program. However, recent advancements in other high-speed decelerators have shown the possibility of migrating from rigid aeroshells like the Viking and Pathfinder capsules. These advances come in the form of Deployable Entry Vehicles (DEV) and have been identified as a core technology investment area by NASA's Entry, Descent, and Landing group in 2017[48]. In a whitepaper by Cassell[49], two DEVs are described and include inflatable decelerators and mechanically deployed decelerators. The idea of using an inflatable drag device has been around as early as the 1960's when the Goodyear Company coined the term "ballute" (a portmanteau of balloon and parachute)[50].

4.1 Ballute Background

In 2000, a review by Hall[51] discussed various ballute configurations that had been studied for planetary aerocapture. The designs mentioned include cocoons, clamped, and towed ballutes. Hall suggests that the cocoon type ballutes are undesirable, citing an earlier study by Park[52] where cocoons were given an overall rating of 'Very bad' due to it providing poor navigability, stability and control, radiative heating,

convective heating, and inability to make multiple passes. Another issue for cocoons mentioned by Hall is removing the cocoon during flight can be complicated because the membrane needs to avoid any protruding vehicle components. For these reasons cocoons will not be discussed further for this study.

Towed ballutes in the form of high-speed parachutes[53–55] or inflatable devices[11, 12, 15, 44, 56–59] have been the focus of many previous studies. Using a towed drag-device is advantageous because it can provide significant separation from the body making detachment easier during flight. While having the separation between the spacecraft and towed ballute is an advantage it does introduce some added complications. The first of which is the tether used to bind the ballute to the vehicle. High-fidelity DSMC simulations were completed by Moss[58] showing that for string-like tethers of diameter 1-cm and 1-mm the tethers were subject to higher heating rates and surface temperatures than the rest of the ballute system. In addition to the heating, the ballutes must be correctly sized to avoid shock impingement emanating from the spacecraft. For something like a toroidal ballute this could be done by adjusting the tether length in combination with inner diameter of the torus to ensure the unsteady wake is swallowed by the ballute instead of interacting with the ballute surface. Lastly, the scale of the fully deployed ballute system makes it difficult to conduct ground testing. Experiments matching the velocity and enthalpies at hypersonic or high speeds is already prohibitively expensive when considering only a small test article. Adding a lengthy tether for a towed ballute may make ground testing undesirable or even intractable.

Before moving on to the actual vehicle configuration that is the basis for this study, two other drag techniques from the literature are worth mentioning. The first is by using an aerocapture tether and the second is using magnetohydrodynamics (MHD). The aerocapture tether differs from a towed ballute because instead of the drag device following behind the vehicle the vehicle remains higher in the atmosphere, deploying the drag device on long tether, and allowing it to penetrate deeper into the atmosphere to generate the aerodynamic drag needed to dissipate energy. A comparison study

conducted by Gates[60] showed that in some scenarios a tethered aerocapture can provide more mass savings than a traditional ballute aerocapture but more studies are needed to fully explore the feasibility of using tethers.

Using MHD appears to be an emerging technology that could be used to augment aerodynamic drag[61–63]. The severe aerothermal environment created during the atmospheric traversal can create a plasma enveloping the spacecraft. Reactionary forces to this plasma can be created through the use of powerful onboard (or tethered) electromagnets[61]. Force control through the use of these MHD devices can augment aerodynamic drag by approximately 50%[64] and are of particular interest because they are less dependent on atmospheric density allowing them to be used at high altitudes in rarefied atmospheres[62]. This type of force control would allow the vehicle to dissipate energy higher in the atmosphere where the stagnation point heating rates would be lower. In addition, Kelly[61] mentions the ability to continuously vary the current to the electromagnets and, effectively, continuously modulate the drag augmentation.

4.2 LOFTID Aeroshell

Finally, we arrive to the drag device configuration for the current study which is based on the LOFTID aeroshell. The aeroshell's forebody is a 70° sphere-cone, and when inflated, has a diameter of 6 m[65]. The LOFTID aeroshell was derived from a series of suborbital flights known as the Inflatable Re-Entry Vehicle Experiments (IRVE) and is in a class of vehicles known as Hypersonic Inflatable Aerodynamics Decelerators (HIAD)[65]. A diagram containing the diameter and nose radius of the inflated aeroshell presented by Hollis et. al.[66] is illustrated in Fig. 4.1 . The normal and axial force coefficients digitized from a report by Korzun et. al.[65] is displayed in Fig. 4.2. The normal and axial force coefficients are plotted as a function of Mach number with the colored lines representing constant angle of attack. A note about the force coefficients is the axial force coefficient for angle of attack equal to

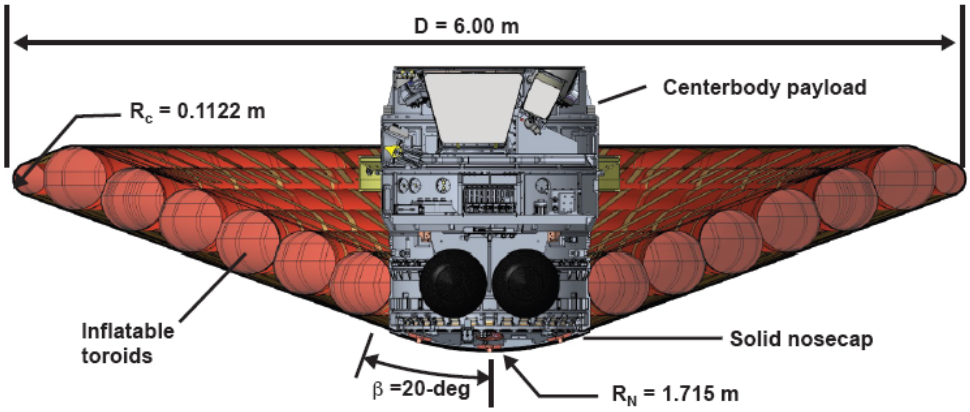


Figure 4.1: Diagram of the inflated LOFTID aeroshell (image from Hollis et. al.[66]).

0 was coincident with the line for angle of attack equal to 2° and the normal force coefficient for 0° angle of attack was 0 for all ranges of Mach. This is why they are indistinguishable in the figures.

The LOFTID RV successfully separated from the United Launch Alliance (ULA) Atlas V rocket during its flight in November 2022. From the trajectory reconstruction by Karlgaard et. al. [67] from separation from the launch vehicle to splashdown, the total flight time of the LOFTID aeroshell was approximately 56 minutes. The aeroshell reached the atmospheric interface at an altitude of 125 km about 31 minutes after separation with an entry velocity of 7.95 km/s and entry angle of -2.29°. During the 6 minutes and 46 seconds after entering the atmosphere the LOFTID aeroshell was subjected to a peak heating of 39.77 W/cm^2, a peak deceleration of 8.98 g's, and a peak dynamic pressure of 2.08 kPa[65]. The RV then ejected the data module, continuing to decelerate until finally deploying the parachute ultimately splashing down in the Pacific Ocean. Both RV and data module were recovered.

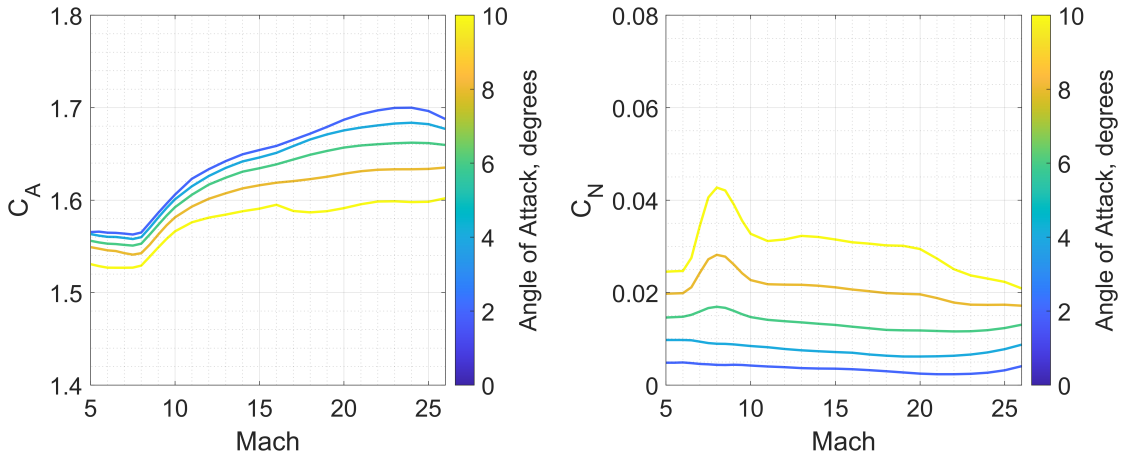


Figure 4.2: Axial and normal force coefficients of the LOFTID RV (digitized from Korzun et. al.[65]).

Table 4.1: LOFTID Vehicle Parameters

Vehicle Design	
Inflated Diameter (m)	6[65]
Cone Half-Angle (degrees)	70[65]
Nose Radius (m)	1.715[65]
Entry Mass (kg)	1100[65]
Max Allowable Heating (W/cm^2)	60[65]
C_D at $\alpha = 0$	1.69[66]

Chapter 5

Methodology

Completing the simulations required the use of multiple off-the-shelf software suites and custom developed codes. These software packages included the previously mentioned MAnE, POST (the Program to Optimize Simulated Trajectories), and SPICE (Spacecraft Planet Instrument C-matrix Events).

5.1 Simulation Setup

Initially, the simulated trajectories through Triton's atmosphere were conducted using the NASA software called POST (The Program to Optimize Simulated Trajectories)[68]. The POST simulations served as the basis for the preliminary study by Brisby and Lyne [23] that considered only non-lifting trajectories. Afterwards it became necessary to develop a program for simulating trajectories which will be discussed later. However, to make the transition to the new code easier it was developed to use similar inputs and models as POST. The following sections present the models used for the simulations and values used for the various parameters, along with any assumptions needed for justification.

5.1.1 Triton Physical Parameters

Due to Triton being nearly spherical, a zonal harmonic model should have little effect on the gravitational acceleration. However, these values were inherited from the previous studies by Ramsey and Lyne [11, 12] so they were used in the current study as well. The value of the J_2 term was 4.9E-05 while J_3-J_8 were 0. In addition to these values being carried over from previous simulations, references for where those values originated could not be located. The gravitational parameter, equatorial radius, and polar radius were set to 1.4278E+3 km^3/s^2, 1352 km, and 1352 km, respectively. Lastly, the rotational velocity was set to 1.2E-05 rad/s because, as mentioned in Chapter 3, Triton is tidally locked in a synchronous orbit about Neptune with a period of ∼5.87 days.

5.1.2 Vehicle Initial Position and Velocity

All simulations began with entry conditions specified at an altitude of 1029 km and a due east, equatorial entry. However, the inertial velocity and flight path angle at the atmospheric interface were varied to conduct parameter sweeps to find favorable outbound conditions. In general, inertial velocities between 3.0 km/s and 14.0 km/s and entry angles between -45.0° and -57.0° were used to explore the parameter space. The initial position for entry was used because it corresponded with the highest altitude from the atmospheric profile that was digitized from the study by Strobel and Zhu [39]. The decision of a due east, equatorial entry was to simplify the trajectories while determining the feasibility of this maneuver. For planning a full mission the atmospheric entry point and heading would depend on the preceding interplanetary trajectory. The velocities were chosen based on the previously mentioned studies[5] while the flight path angle boundaries were selected to provide a range of atmospheric trajectories that would potentially contain the overshoot and undershoot boundaries for an entry corridor width.

5.1.3 Initial Vehicle Orientation

Vehicle parameters were chosen to represent similar performance to what was demonstrated by the LOFTID aeroshell. The mass and reference area were input to be 1100 kg and 28.27 m^2 which match the fully inflated 6 m diameter, 70° sphere-cone geometry[65]. Aerodynamic coefficients were selected based on the continuum axial force coefficients reported by Korzun et. al. [65]. For the non-lifting simulations, the lift and drag coefficients, C_L and C_D, were set to 0.0 and 1.69, respectively. These values assume the aeroshell maintains no angle of attack, sideslip, and bank throughout the atmospheric trajectory. For the lifting simulations the C_L value was input as 0.3 and assumed a 10° angle of attack, 0° sideslip, irrespective of bank angle.

5.1.4 POST Workflow

POST was installed on a Unix server that was housed by the University's IT department and approved users were only permitted to execute the compiled program which meant the only way to interact with the POST software was defining the parameters in the input file. The workflow began by running a single trajectory with the desired input conditions and running a secondary post-processing tool to generate a text file containing the time-history of predetermined variables for the trajectory. The files would then be downloaded from the Unix server for further post-processing that included calculating the aerodynamic heating, determining the turn angle, and extracting the minimum altitude reached. To expedite the process, a bash script was written to loop through the desired velocity and entry angles and generate the trajectory output files. This process was used to complete the simulations with the vehicle at at zero angle of attack, producing no lift. Once the non-lifting trajectories were completed the next thing to do was allow the vehicle to produce lift to begin searching for the corridor width. Early in this process the Unix server on which POST was installed suffered a hardware failure and became unavailable for further simulations.

5.1.5 Code Development

While coordinating the hardware repair, it became clear that the timeline for getting the Unix server back in operation was longer than expected. In the downtime of waiting for repairs the author was able to develop my own trajectory simulation program. While planning how to approach the development of this new code the author decided to use the same models used in POST[69] to ensure the trajectories were being calculated correctly. This included using the Fisher model for calculating the non-spherical gravitational acceleration, a point-mass representation of the aerodynamic forces, and a 4th-Order Runge-Kutta algorithm to propagate the trajectories.

The newly developed program was written in FORTRAN due to its speed and lack of licensing requirement. The code takes as input the initial state vector of the vehicle in the inertial reference frame. At each step during the trajectory a non-spherical gravitational model is used to update the vehicle's state-vector in the inertial reference fame. The aerodynamic forces are calculated first in the body-frame with the user supplied mass, surface area, aerodynamic coefficients (C_D, C_L), and vehicle orientation (current angle of attack, sideslip, and bank angle). These forces were added to the inertial acceleration by first dividing them by the vehicle mass and rotating the components into the inertial reference frame. More information about the logic and equations used for developing the code can be found in the appendix.

After implementing these primary capabilities into my code, comparisons were done with trajectories that had been previously calculated using POST. Figures 5.1 and 5.2 show trajectory comparisons between the two codes. The trajectories shown in Fig. 5.1 represent a shallow atmospheric entry flight path angle of -52.0° and an entry velocity of 5 km/s. These conditions were chosen to result in a trajectory that would be marginally affected by aerodynamic forces. The plots on the top show the flight path when the vehicle orientation is at 10° angle of attack and 180° bank angle, 'Full Lift Down'. The middle plots show the trajectory assuming the vehicle is at 0

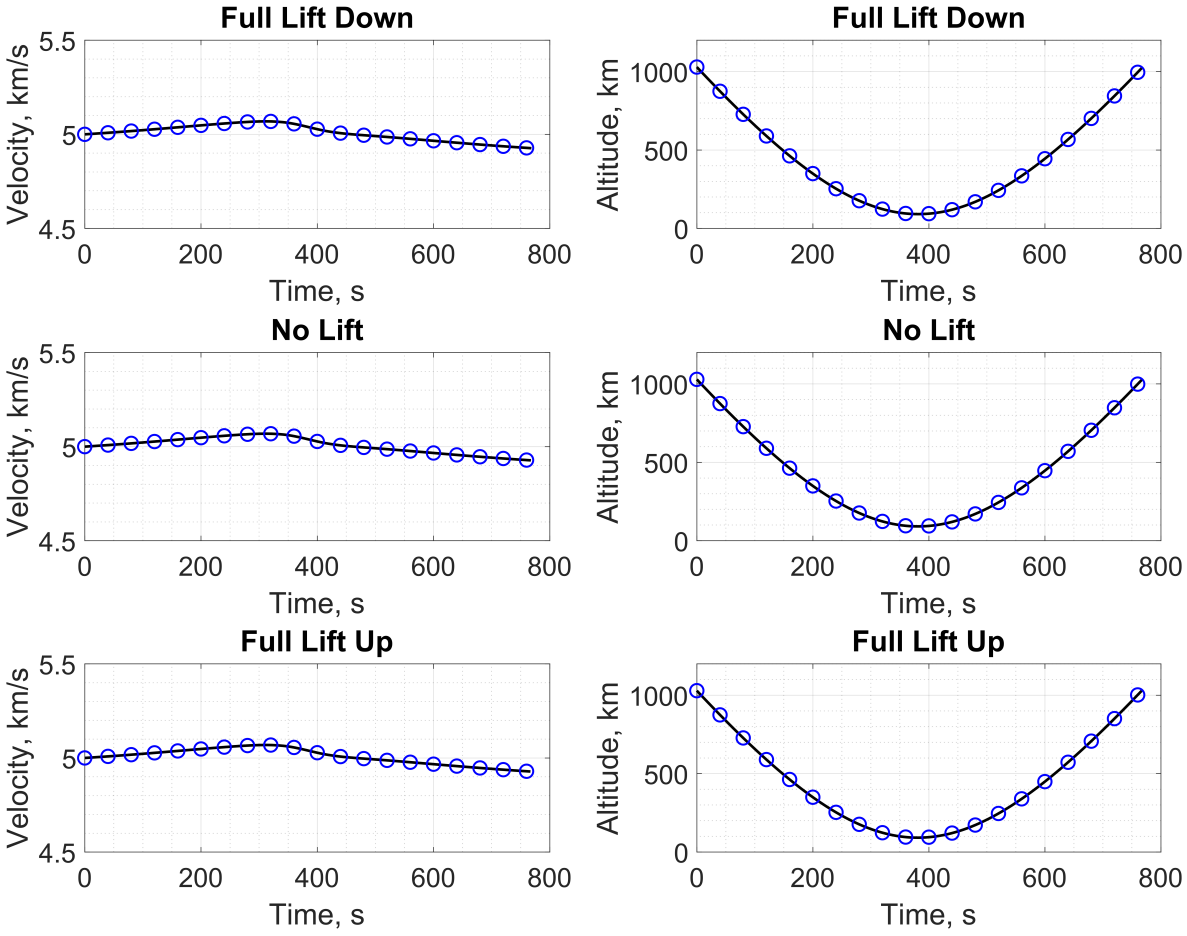


Figure 5.1: Time history plots of velocity and altitude for a vehicle entering Triton's atmosphere at 5 km/s and angle of -52.0°. Solid black lines represent the POST trajectory while the blue circles are what were produced from the newly developed code.

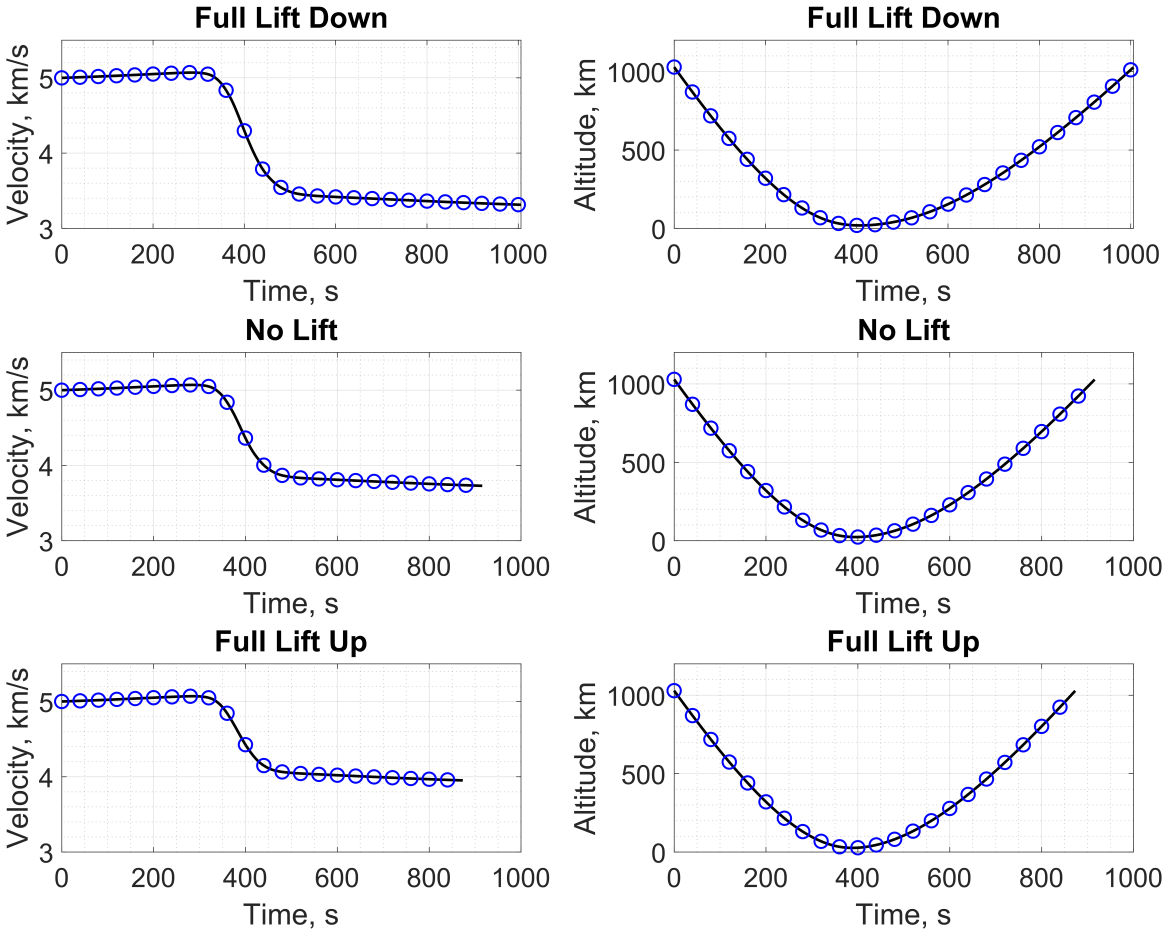


Figure 5.2: Time history plots of velocity and altitude for a vehicle entering Triton's atmosphere at 5 km/s and angle of -54.0°. Solid black lines represent the POST trajectory while the blue circles are what were produced from the newly developed code.

angle of attack, producing no lift. Lastly, the plots on the bottom show the flight path of the vehicle when at 10° angle of attack but 0° bank angle, 'Full Lift Up'. Figure 5.2 shows the flight paths of a vehicle also entering the atmosphere at 5 km/s but at a slightly steeper flight path angle of -54.0°. The velocity and altitude plots show very good agreement suggesting that the new trajectory code is accurately calculating the aerodynamic forces and applying them in the correct directions. A comparison of the inertial accelerations can be found in Fig. 5.3 and shows aerodynamic loads are the dominant contributor to the forces acting on the vehicle for a large portion of the AGA.

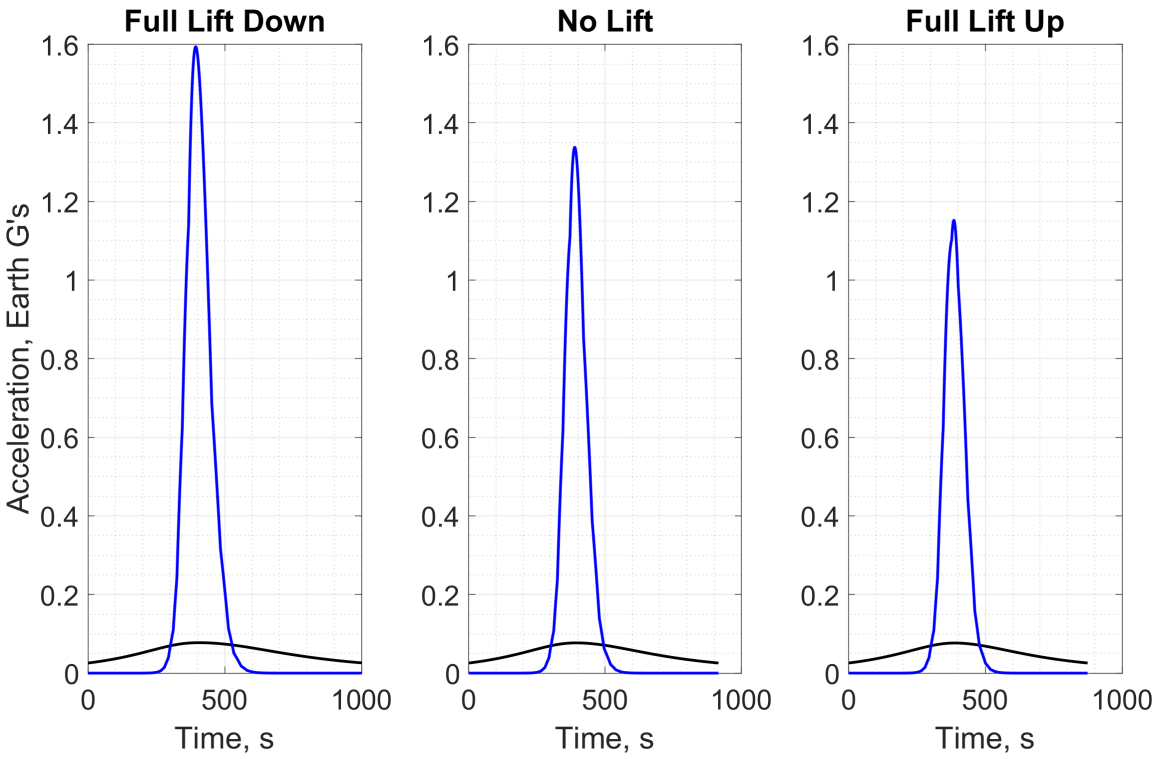


Figure 5.3: Comparison of the components of acceleration in the inertial frame for a vehicle entering Triton's atmosphere at 5 km/s and angle of -54.0°. Black lines represent the gravitational component while the blue line is the aerodynamic component.

It should be noted that no attempt was made during this development to provide a feedback loop to the vehicle for reaching steady-level flight. The trajectories follow only the pre-programmed aerodynamics defined in the input file. After verifying that the trajectories were being calculated correctly using only a single aerodynamic configuration (non-maneuvering, constant mass, and constant surface area) changes were made to allow for simple maneuvering and changes to the vehicle parameters during the flight.

The first of these was to allow the vehicle to perform a banking maneuver at some predetermined altitude during the trajectory. For capsule-type vehicles, cranking the lift vector through applying a bank angle allows the vehicle to adjust its heading while maintaining the magnitude of lift being produced[70]. Currently, only a single banking maneuver can be done and requires the user to specify the total change in the bank angle, duration over which to apply the bank angle, and finally the altitude at which to begin the maneuver.

The second change to the vehicle parameters that can be done during the trajectory is setting an elapsed flight time, after atmospheric entry, for jettisoning any assumed drag devices. This would be similar to releasing a towed-ballute or removal of a drag-skirt as suggested by Cassell for an ADEPT Drag Modulated Aerocapture[49]. This is done through the input file where the user prescribes the time to perform the 'cut' along with the mass and surface area of the vehicle after the cut. It's currently assumed that the drag coefficient remains the same after jettisoning the drag device.

In addition to calculating singular trajectories the code was setup to perform parameter sweeps over a range of entry velocities, entry angles, total bank angle, duration of bank change, and altitude to begin the banking maneuver. When performing the parameter sweep only a subset of the variables are saved as output to reduce the file I/O and hard drive expense. The variables used to perform parameters sweeps are also assumed to be at regular intervals to form a structured table which provides easy interpolation between trajectories. After conducting preliminary simulations the author recognized the need to refactor portions of the code to allow for

multi-threading through the use of OpenMP. Utilizing the multi-threading provided a significant speed up. As a benchmark, using 16 threads on a personal laptop with an AMD Ryzen 7 8840HS processor, the program runs through ∼9-10 thousand trajectories per minute. Of course, this may differ depending on the configuration of the trajectories being run.

5.1.6 Aerodynamic Heating

The peak heating throughout the trajectories was assumed to occur at the stagnation point. While this is not always the location of the most severe heating, it is a good benchmark and is a common metric used when considering atmospheric entry vehicles. Factors that could change where the peak heating occurs are the vehicle orientation and boundary layer transition both of which could be explored in follow-on studies but will require code development or coupling to another software package. The stagnation point convective and radiative heating are calculated over each time step during the simulated trajectory. For each trajectory the code will report the peak convective, radiative, and total heating that occurred during the simulation. In addition, the integrated heat load is updated at every time step to track how much heating occurred over the entire trajectory. Tracking these values can be useful to understand which type of heating has the highest contribution during the flyby. Trajectories can then be altered to ensure the heating constraints are not violated.

The instantaneous stagnation point convective heat rate is calculated at each iteration in the trajectory by using the Sutton-Graves equation[71] (Eq. 5.1)

$$\dot{q_c} = kV_\infty^3\sqrt{\frac{\rho_\infty}{r_n}} \tag{5.1}$$

where ρ_∞ is the freestream density in kg/m^3, V_∞ is the atmosphere relative velocity in m/s, r_n is the nose radius in m, and k is the heat-transfer coefficient derived for a specific atmospheric composition. Since Triton's atmosphere was shown to be over 99% N_2 a value of 1.75E-08 was calculated for k based on the tables from Sutton and

Graves[71]. Equation 5.1 assumes the flow is fully catalytic at the wall and does not include a hot-wall correction term, which can frequently be neglected for hypersonic flows.

To handle the radiative heating an algorithm was implemented into the trajectory code that would interpolate the instantaneous stagnation point radiative heating based on the tabulated values published by Sutton and Hartung[72]. The tables provide calculated values for radiative heating rates for a range of nose radii from 0.05 m to 10 m and velocities between 8 km/s to 18 km/s within Earth's atmosphere corresponding to air densities of 1.841E-02 kg/m^3 to 9.6940E-06 kg/m^3. The radiative heating is only calculated if it is within the range of the table. The range of nose radii encompasses that of the LOFTID aeroshell geometry (1.715 m) and the range of atmospheric density is applicable for Triton up to an altitude of ∼48 km. Admittedly, this is a small range of the actual trajectories due to the applicable ranges of velocity and freestream densities, but the results will show convection as the dominant component of stagnation point heating.

Chapter 6

Results

Numerous trajectory scenarios were simulated to explore the parameter space, searching for combinations of entry conditions, vehicle orientation, and maneuvers that would successfully execute a Triton AGA. The total number of trajectories simulated to construct the following data is in the tens of millions. In order to reasonably present the data from the trajectories it will be separated into the following sections: ballistic, lifting, maneuvering, and jettisoning. In all scenarios the simulations began at the atmospheric interface (altitude of 1029 km) in a due-east equatorial trajectory, with a drag coefficient of 1.69. The ballistic and jettisoning trajectories were simulated with zero lift coefficient because they were axisymmetric bodies flown at 0° angle of attack while the lifting and maneuvering trajectories applied a lift coefficient of 0.3. These aerodynamic coefficients were chosen based on the aerodynamic performance reported by Hollis et. al.[66] for the LOFTID aeroshell at Mach=25 and angle of attack of 10°. The simulated trajectories would terminate once the vehicle reached the atmospheric interface (indicating outbound atmospheric exit) or reached an altitude of 0 km, indicating a surface impact. The following results from each of the parameter sweeps contain only trajectories that do not impact the surface or capture into orbit about Triton. Additionally, the figures will contain

results from trajectories that may violate some of the desired physical constraints but will be used to illustrate the bounds of 'good' trajectories.

Results from the ballistic trajectories will be shown first to establish a baseline for the simplest cases. For the ballistic trajectories, it is assumed that the vehicle flies at an angle of attack of 0°, therefore producing no lift. Following the results from the ballistic trajectories will be the lift-enabled, non-maneuvering trajectories. These trajectories were computed assuming 10° angle of attack to make use of the lift coefficient and maintained a bank angle of either 0° (full lift up) or 180° (full lift down) throughout the entire trajectory. Since the vehicle orientation for these first three parameter sweeps was fixed there exists a 1-to-1 relationship between the prescribed entry conditions and the final state of the trajectories.

The next set of results come from the maneuvering trajectories. All of the banking maneuver trajectories maintain an angle of attack of 10° and begin at a bank angle of 0° (full lift up). Once the vehicle reaches the specified altitude to trigger a banking maneuver, it will begin rotating the lift vector about the relative velocity vector until it reaches a bank angle of 180° (full lift down). The vehicle will remain at 180° bank for the remainder of the trajectory. When the bank maneuver is initiated the roll rate is applied incrementally at each time step until its final orientation is achieved. For this study a roll rate of 18 deg/s was used because it was the roll rate reported in the LOFTID flight reconstruction [67]. The vehicle would enter the atmosphere in a full lift up orientation to avoid penetrating too deep into the atmosphere while enabling a steep entry angle. Then at some point during the trajectory (while still in the atmosphere) the vehicle performs the banking maneuver to change its orientation to fully lifting down. The intent is to leverage the aerodynamic forces to keep the vehicle in the atmosphere longer to dissipate more energy and reach a lower outbound excess speed than it would have without the maneuver. However, one tradeoff of reaching lower outbound excess velocities in the manner is prolonged exposure to the severe aerodynamic heating that accompanies traveling through atmospheres at high speed.

Traditionally, these bank-roll type maneuvers are used to find the undershoot boundary that defines the corridor width for a specific combination of outbound excess velocity and required turn angle. This combination of exit conditions is determined only when the orientation of vehicle, assisting body, and target body are known which requires precise date and time the vehicle arrives to perform the maneuver. Because of the need to develop an in-house capability for simulating the atmospheric trajectory, there wasn't enough time to pinpoint specific arrival conditions. In lieu of having targeted atmospheric exit conditions, the corridor widths are calculated parametrically to present a potential range of corridors that could be achieved.

Trajectories that involve jettisoning the drag device flew at 0° angle of attack which mirrored the conditions of the initial ballistic parameter sweep, but at some prescribed time during the trajectory the vehicle would change its mass and reference surface area. The 'cut time' is defined as input to code along with a new mass and reference surface area. A presentation by Dillman[73] reported the mass of the inflatable structure at 62 kg and flexible thermal protection system and sensors at 106 kg for a total of 168 kg. It was assumed that all 168 kg would be jettisoned during the event. It should be noted that the total mass reported by Dillman[73] was 1190 kg whereas this study used a total mass of 1100 kg because it was reported as the as-flown aeroshell mass[65]. Additionally, the components displayed by Dillman[73] as being stored within the core body of the aeroshell (parachute system, inflation system, centerbody, avionics and sensors) were assumed to remain onboard. The new reference area was assumed to be 1.37 m^2 which is based on the frontal area of the centerbody having a 1.32 m diameter. In the simulations it is assumed that the jettison event happens instantaneously and without any induced fight instabilities. In practice, this technique needs to be vetted thoroughly to ensure that separation of the drag device happens cleanly, i.e., does not catch on any protrusions from the vehicle. Further, a real vehicle will likely experience some flight instabilities due to the sudden change in mass and aerodynamic forces, all of which are neglected in this study.

A final note about how results for the maneuvering and jettison simulations were generated and processed follows. Initially, simulations were completed for various values of bank altitude (for the maneuvering) and cut time (for the jettison). The results would be processed using gridded interpolation. When discontinuities were encountered in the results more simulations were conducted with input parameters (bank altitude or cut time) that would provide refinement to smooth out trends in the results. The assumption with this technique is that the incremental changes in entry conditions is adequately resolved to allow for linear interpolation between datasets. To aid in keeping track of the scenario specifics Table 6.1 has been constructed to outline the basic details of each parameter sweep.

6.1 Ballistic Trajectories

The ballistic trajectories were simulated over a range of atmospheric entry velocities starting at 3 km/s up to 12.98 km/s at an increment of 0.02 km/s while the range of entry angles was from -57° to -50° at an increment of 0.01° and yielded a total

Table 6.1: Range of Entry Conditions

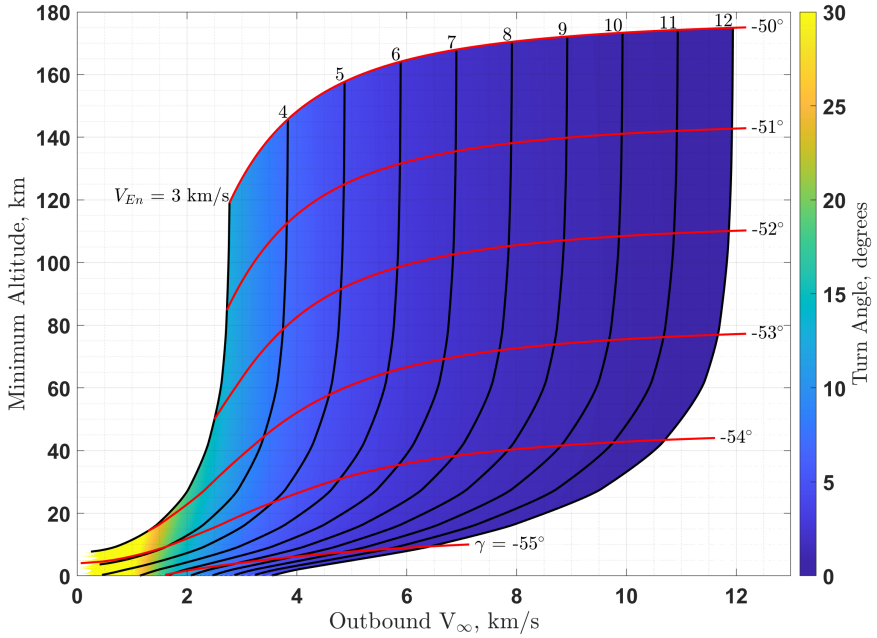
	Ballistic	Full Lift Up	Full Lift Down	Banking	Jettison
V_{En}, km/s	3 to 12.98	3 to 12.98	3 to 12.98	3 to 12.95	3 to 12.95
γ_{En}, degs	-57 to -50	-57 to -50	-57 to -50	-56 to -52	-56 to -52
C_d	1.69	1.69	1.69	1.69	1.69
C_l	0	0.3	0.3	0.3	0
α,degs	0	10	10	10	0
m_i, kg	1100	1100	1100	1100	1100
m_f, kg	1100	1100	1100	1100	932
A_i, m^2	28.27	28.27	28.27	28.27	28.27
A_f, m^2	28.27	28.27	28.27	28.27	1.37
β_i, degs	0	0	180	0	0
β_f, degs	0	0	180	180	0
BC_i	23.11	23.11	23.11	23.11	23.11
BC_f	23.11	23.11	23.11	23.11	404.71
# of Trajs	350,500	350,500	350,500	11,935,960	5,775,120
Total Number of Trajectories = 18,762,580					

of 350,500 trajectory results. The contours shown in Fig. 6.1 illustrate how the outbound hyperbolic velocity, minimum altitude, and turn angle vary with changes in the atmospheric entry conditions. The solid black lines outline different values of atmospheric entry velocity while the solid red lines represent the entry angle. Similar contours are displayed in the following section for the non-maneuvering trajectories.

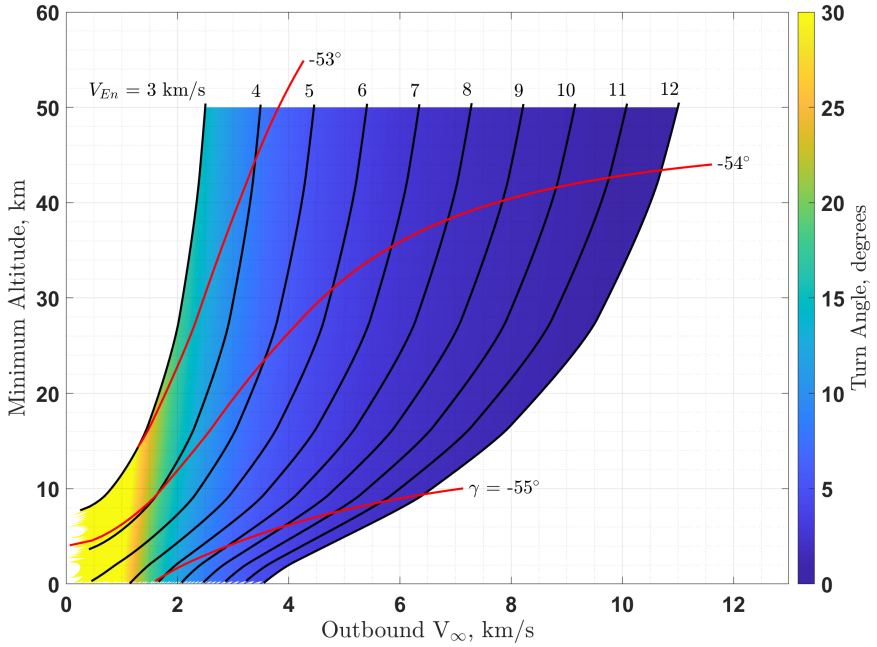
Since this is a lot information to pack into a single figure readers can use the following sample point to ensure they are interpreting the figure correctly. Consider a non-lifting trajectory entering the atmosphere at 9 km/s and an entry angle of -54°. Looking at Fig 6.1 reveals for those entry conditions, the trajectory would penetrate to an altitude of about 40.2 km, have an outbound excess speed of 7.84 km/s, and a turn angle of 1.66°. Examination of Fig. 6.1 shows that an AGA performed ballistically at Triton could produce sufficient energy loss for a wide range of entry conditions without going below 10 km altitude. Figure 6.1b shows that a trajectory with a 3 km/s atmospheric entry velocity and entry angle of -53.12° will have an outbound hyperbolic excess speed of ∼0.8 km/s and achieve a turn angle greater than 30°. Similarly, an entry velocity of 12 km/s can enter at a steeper angle of -54.98° to avoid penetrating below 10 km and reach a hyperbolic excess speed of 6.57 km/s but only achieves a turn angle of 1.74°.

However, when considering the LOFTID heating constraint of 60 W/cm^2, Fig. 6.2 shows a reduction in feasible entry conditions. It suggests that for entry velocities above 9 km/s steep entry angles will subject the vehicle to stagnation point heating rates that would exceed the limits of the heat shield. Furthermore, the steepest entry angle that can be paired with a 9 km/s entry velocity is -54.88° which would produce an outbound velocity of 4.83 km/s and turn angle of 3.13°. Any steeper entry would violate the 10 km minimum altitude threshold.

It should also be mentioned that in Fig. 6.2 there are discontinuities in the contour lines which are more apparent with higher entry velocities. The primary reason for this is due to the method used for generating the density profile. The plot that was manually digitized from Strobel[39] presented the number density on a log scale.



(a) Drag-Only



(b) Drag-Only, Up to 50 km.

Figure 6.1: Ballistic trajectory results showing outbound hyperbolic velocity, minimum altitude, and turn angle for lines of constant entry velocity and entry angle.

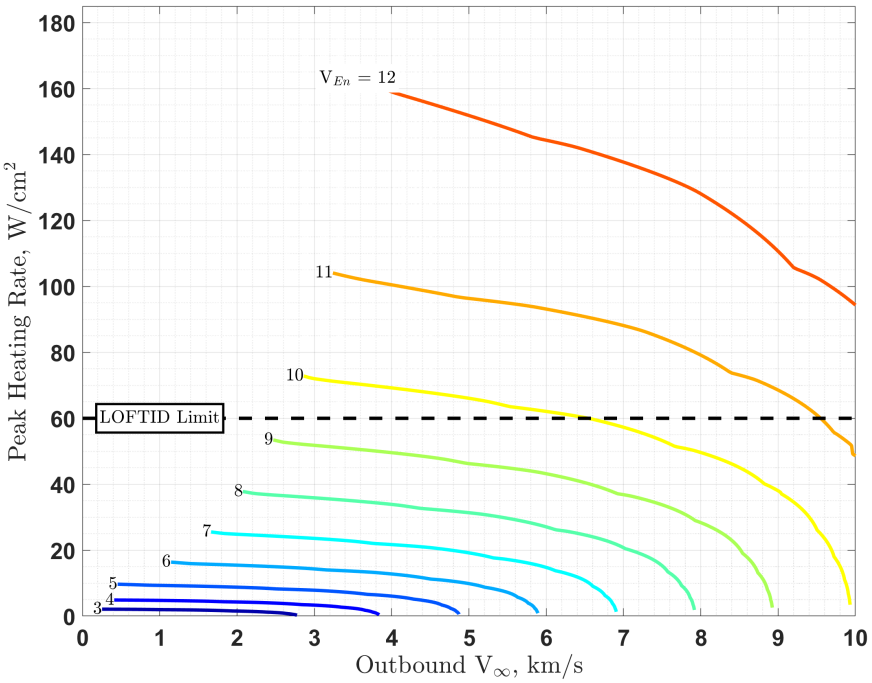


Figure 6.2: Peak heating for the ballistic trajectories.

Smoothing out the density profile should alleviate the discontinuities but will have minimal effect on the overall outcome. The reason the discontinuities seem to be exacerbated at higher entry velocities is due to how the radiative heating is being applied during the trajectories. The radiative heating is only calculated at trajectory points when it is within range of the curve fits derived from the tables presented by Sutton and Hartung[72]. The lowest velocity from the Sutton and Hartung[72] tables that is applicable to Triton's tenuous atmosphere is 9 km/s. When trajectory conditions are not within range of the curve fits the radiative heating component of the peak stagnation point heat rate is computed as 0 W/cm^2. The only simulated trajectories with a potential to have a radiative heating component are those reaching a velocity of 9 km/s or higher.

After producing the stagnation point peak heating rates shown in Fig. 6.2 it was found that the convective heating component is the primary factor in limiting trajectories due to heating constraints. Theoretical heating rates were calculated for a vehicle having a nose radius of 1.715 m (matching the LOFTID aeroshell) over the

range of potential velocities and altitudes using Eq. 5.1 for the convective heat rate and the tables from Sutton and Hartung for the radiative heat rate. These potential heating rates are shown in Fig. 6.3

where the solid lines represent the convective heating component and the dashed lines are the radiative component. By the time the radiative heating rate has reached 1 W/cm^2 the convective heating has already exceeded or nearly exceeded the 60 W/cm^2 constraint.

An additional excursion focused on the how the minimum altitude is affected by changes in ballistic coefficient was completed in preparation for a conference[74] and the adapted results are presented in Fig. 6.4 through Fig. 6.7. Each plot illustrates how higher ballistic coefficients require lower minimum altitudes to reach the desired outbound excess speeds for a number of atmospheric entry velocities. The point at the far right in each plot represents the fully inflated LOFTID aeroshell with a ballistic coefficient of 23.11.

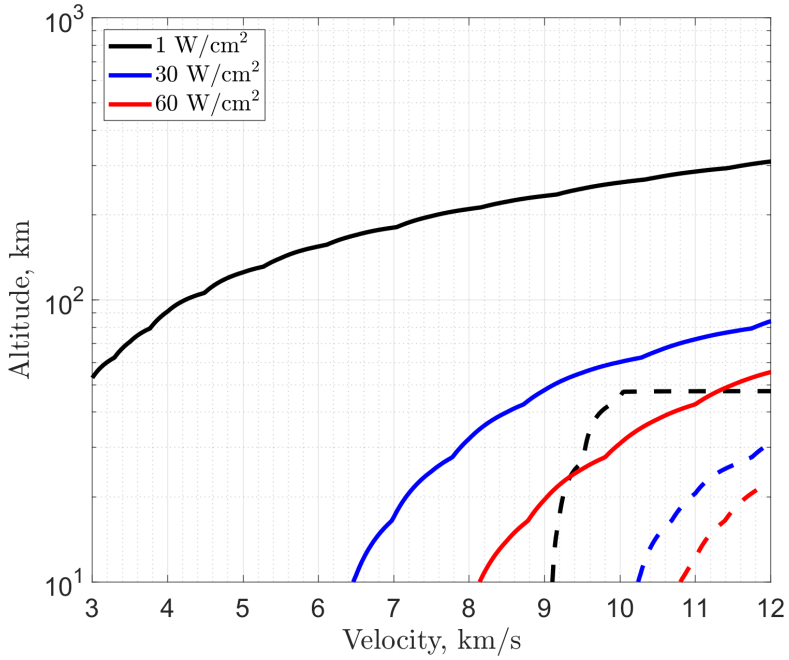


Figure 6.3: Components of the potential peak heating rate in Triton's atmosphere for velocities between 3 km/s and 12 km/s above 10 km altitude.

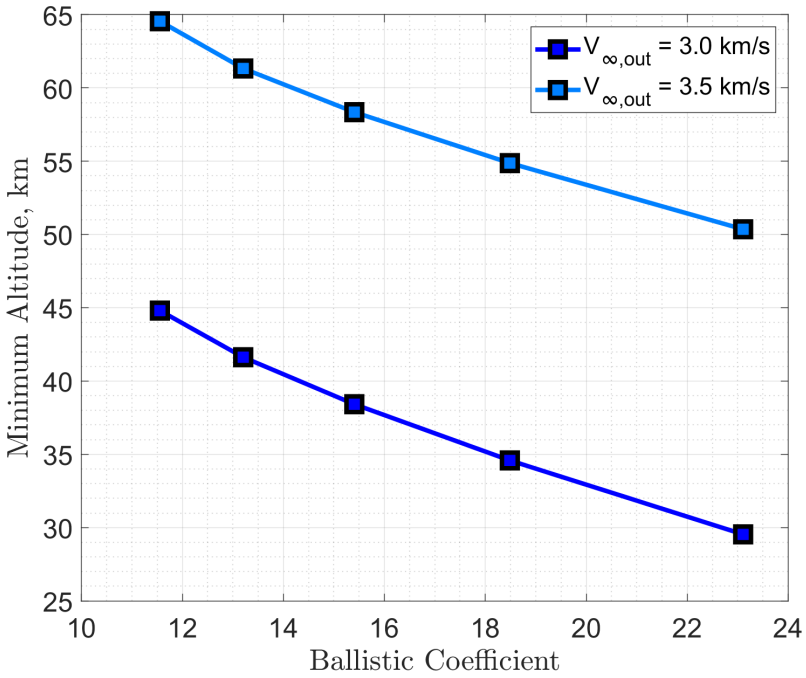


Figure 6.4: Change in minimum altitude as a function of ballistic coefficient for $V_{En} = 4.0$ km/s

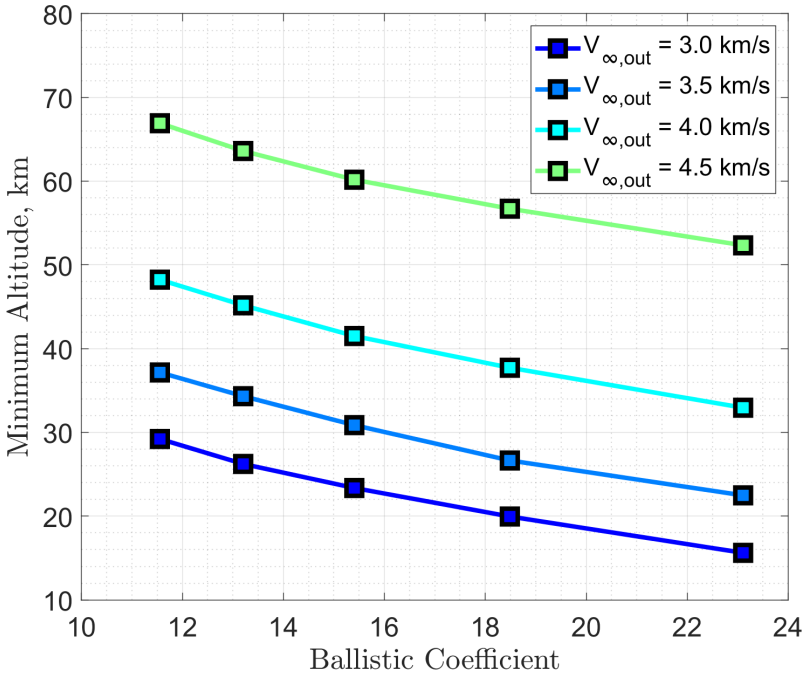


Figure 6.5: Change in minimum altitude as a function of ballistic coefficient for $V_{En} = 5.0$ km/s

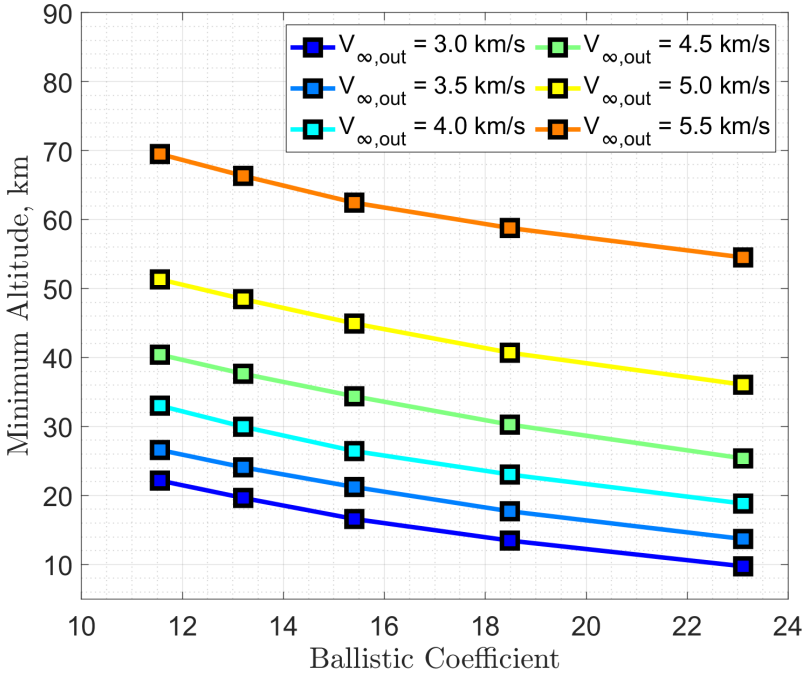


Figure 6.6: Change in minimum altitude as a function of ballistic coefficient for $V_{En} = 6.0$ km/s

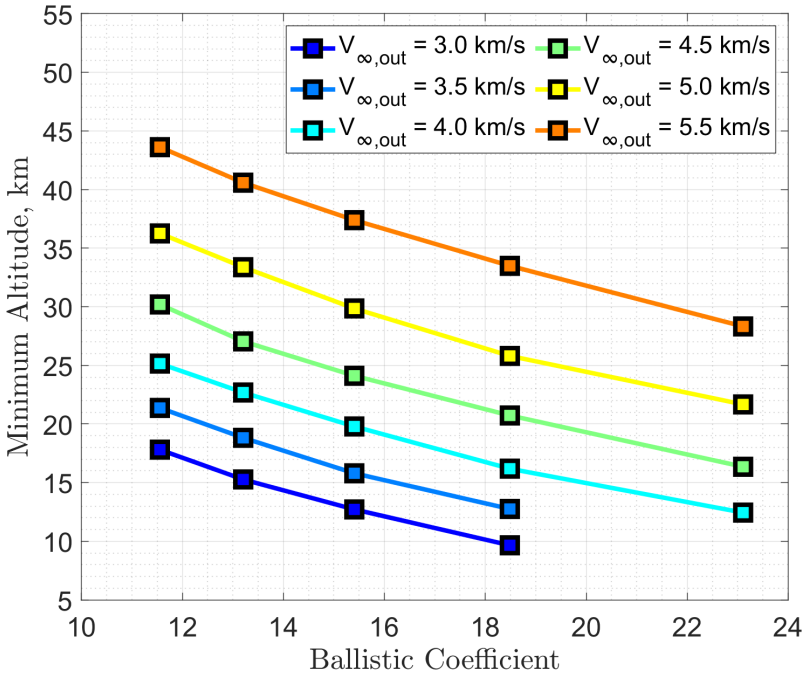


Figure 6.7: Change in minimum altitude as a function of ballistic coefficient for $V_{En} = 7.0$ km/s

6.2 Lifting Trajectories

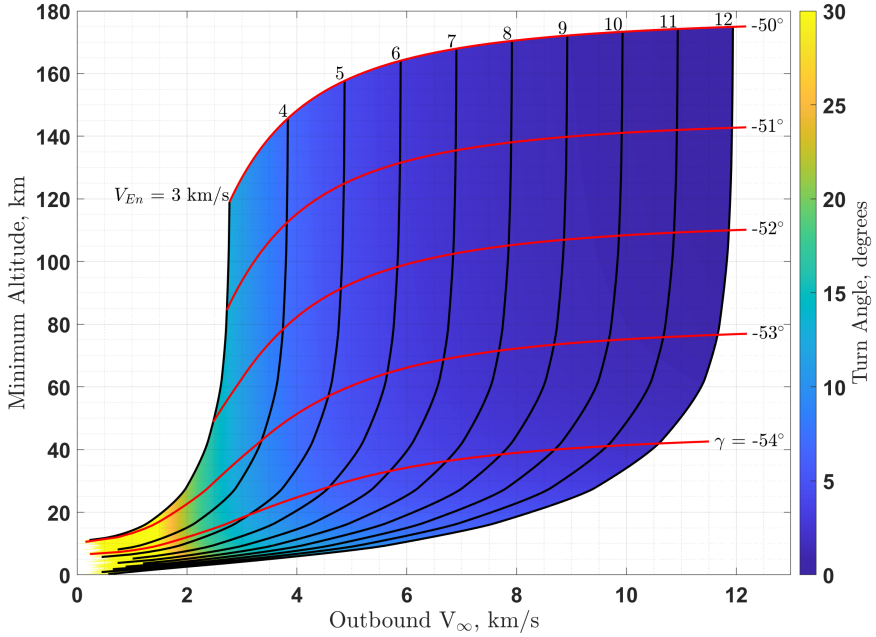
Each of the lifting trajectory parameter sweeps was done over the same range of entry conditions as the ballistic trajectories (V_{En}=[3, 12.98] km/s and γ_{En}=[-57, -50]°). The only difference is these trajectories were flown at a constant angle of attack (α=10°) and bank angle (β=0° for full lift up and β=180° for full lift down). The contours shown in Fig. 6.8 and 6.9 illustrate how the outbound hyperbolic velocity, minimum altitude, and turn angle vary with changes in the atmospheric entry conditions for the non-maneuvering trajectories. The contours look very similar to those constructed for the ballistic trajectories, but in the lower altitudes differences begin to be arise due to higher density and aerodynamic forces.

Using Fig. 6.8, 6.9, and 6.10 it can be determined that trajectories with a given entry velocity can dissipate more energy with a shallower entry angle when in a full lift down configuration than the full lift up configuration (or ballistic). By dissipating more energy the lift down trajectories can reach lower outbound excess speeds, achieve greater turn angles, and be subject to lower peak stagnation point heating.

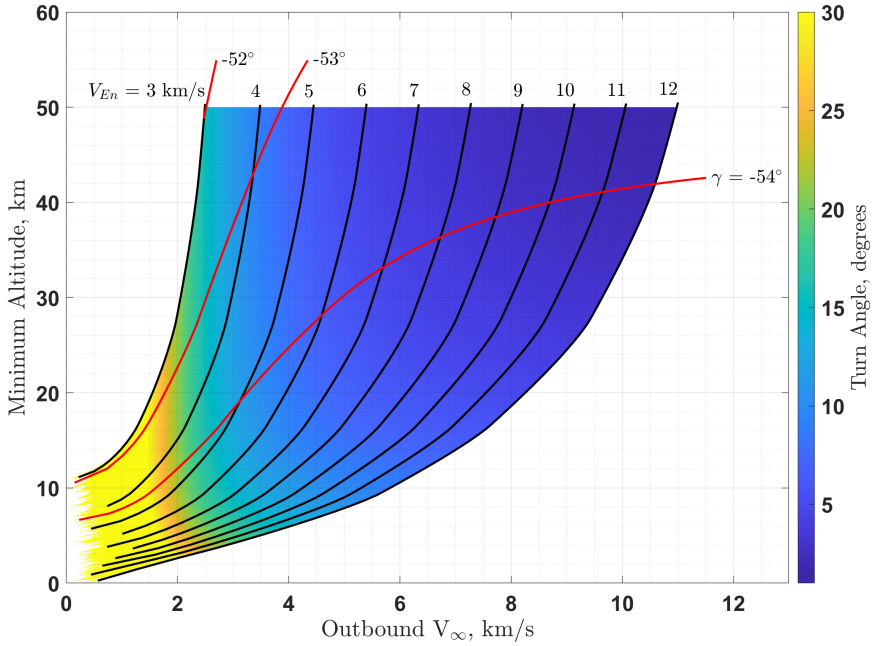
6.3 Maneuvering Trajectories

It is more difficult to summarize the results of the maneuvering trajectories with the contour plots seen previously because the 1-to-1 relationship between entry and exit conditions no longer exists. Each entry condition will have a series of ending conditions based on the timing of the banking maneuver. The plots in Fig. 6.11, 6.12, 6.13, 6.14, 6.15, and 6.16 show the corridor width for specific outbound excess speeds as a function of the entry conditions as defined at an altitude of 1029 km.

The solid black lines represent the overshoot boundary for the targeted outbound excess speed. This is the shallowest a vehicle can enter while at a 180° bank angle and still dissipate enough energy to reach the desired velocity. The solid red line represents the undershoot boundary and is the steepest the vehicle

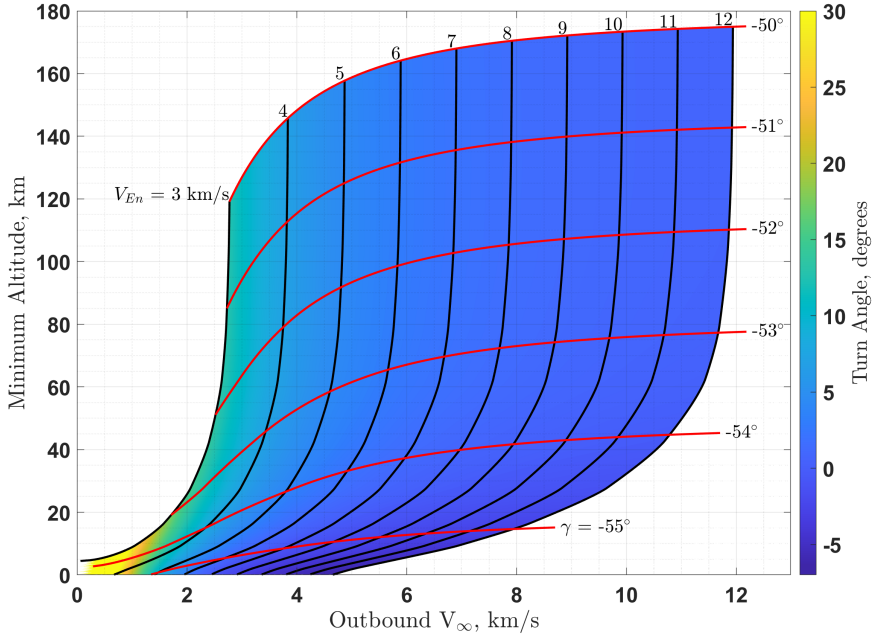


(a) Drag+Lift, Bank of 180°

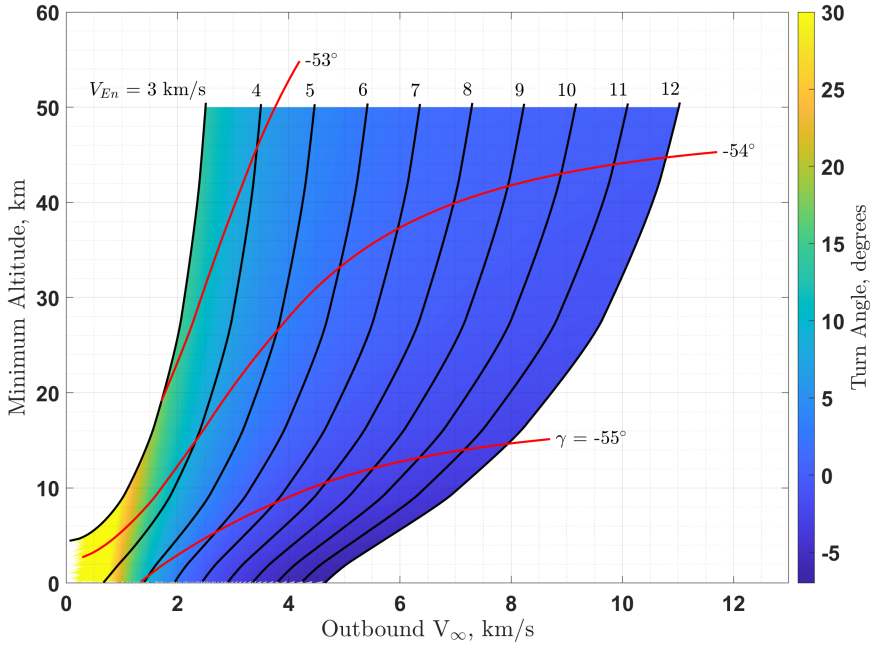


(b) Drag+Lift, Bank of 180°, Up to 50 km.

Figure 6.8: Non-maneuvering, full lift down trajectory results showing outbound hyperbolic velocity, minimum altitude, and turn angle for lines of constant entry velocity and entry angle.

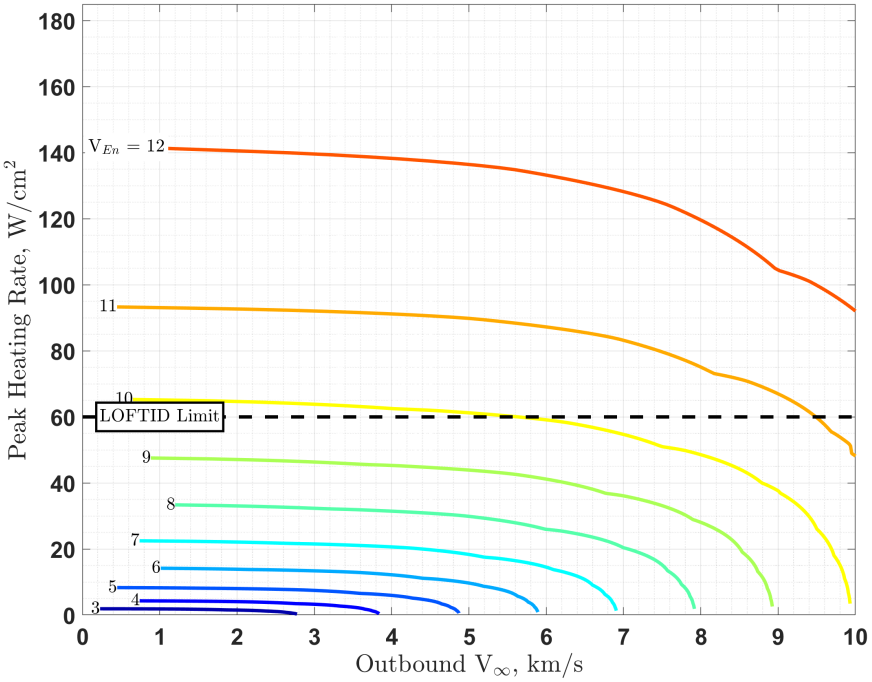


(a) Drag+Lift, Bank of 0°

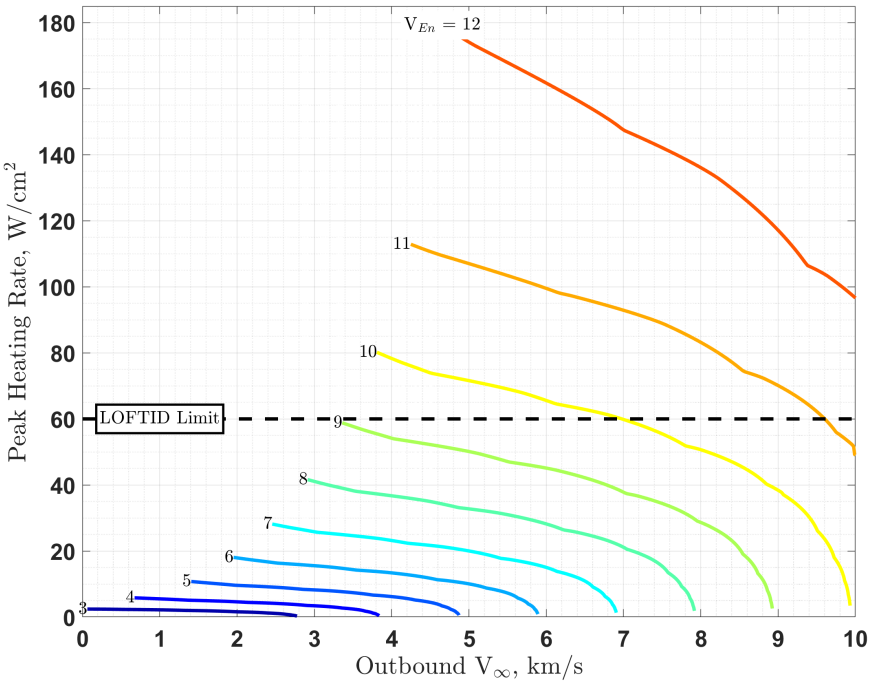


(b) Drag+Lift, Bank of 0°, Up to 50 km.

Figure 6.9: Non-maneuvering, full lift up trajectory results showing outbound hyperbolic velocity, minimum altitude, and turn angle for lines of constant entry velocity and entry angle.

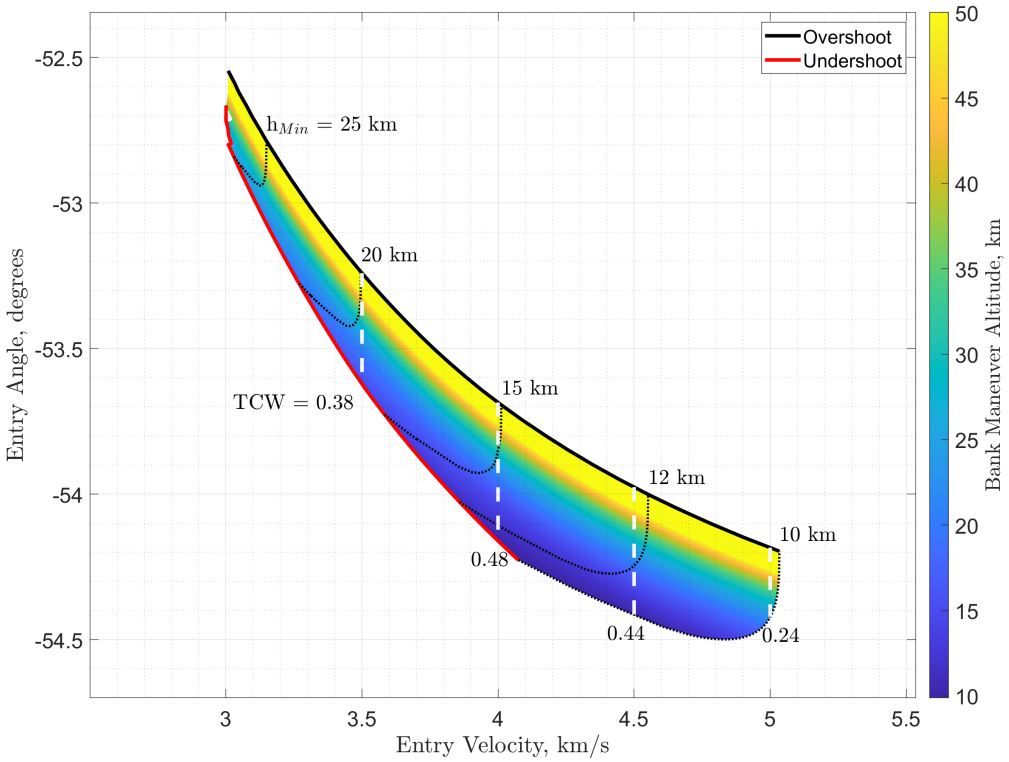


(a) Drag+Lift, Bank of 180°.

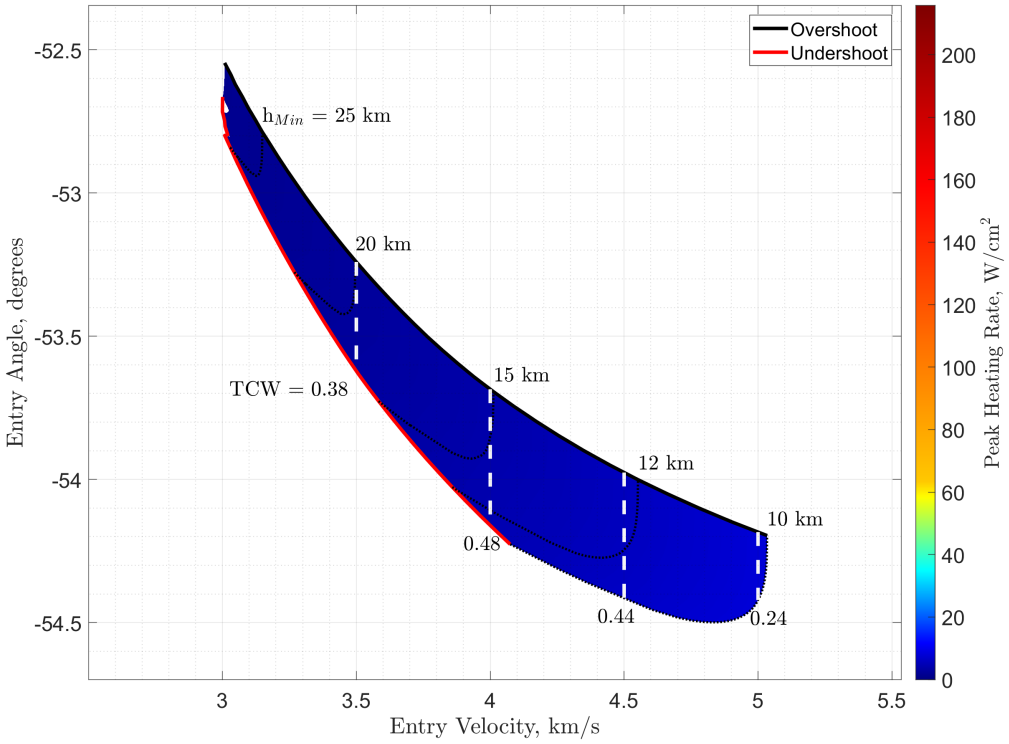


(b) Drag+Lift, Bank of 0°.

Figure 6.10: Non-maneuvering, peak heating.

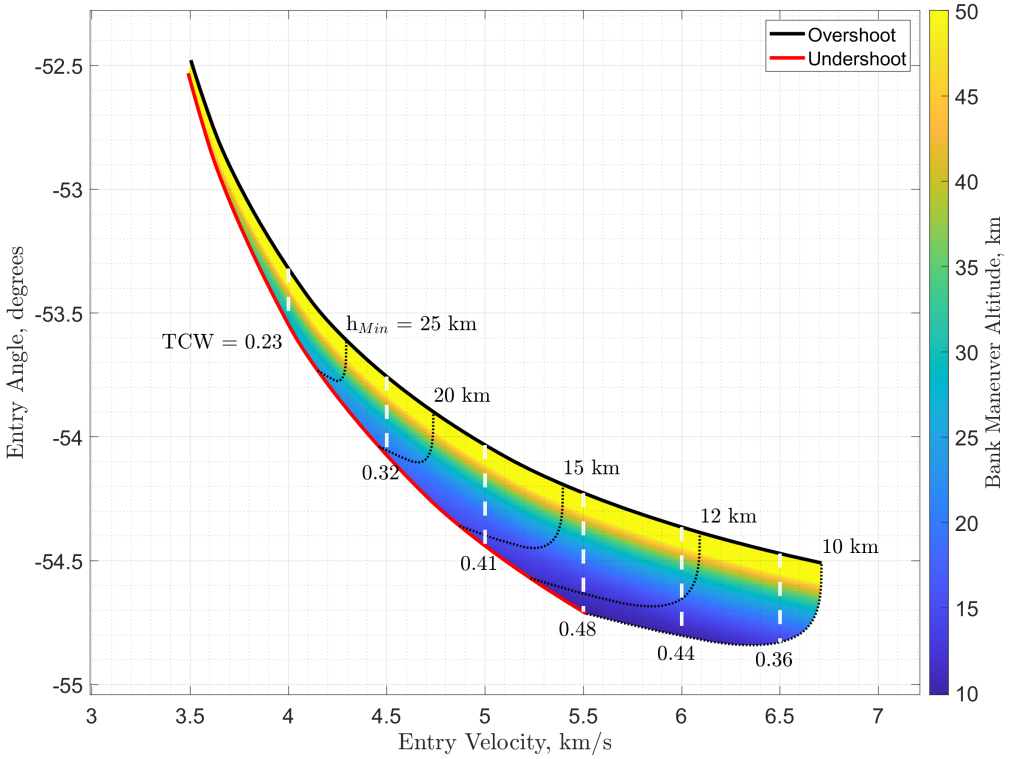


(a) $V_{\infty,out}$ = 2.0 km/s

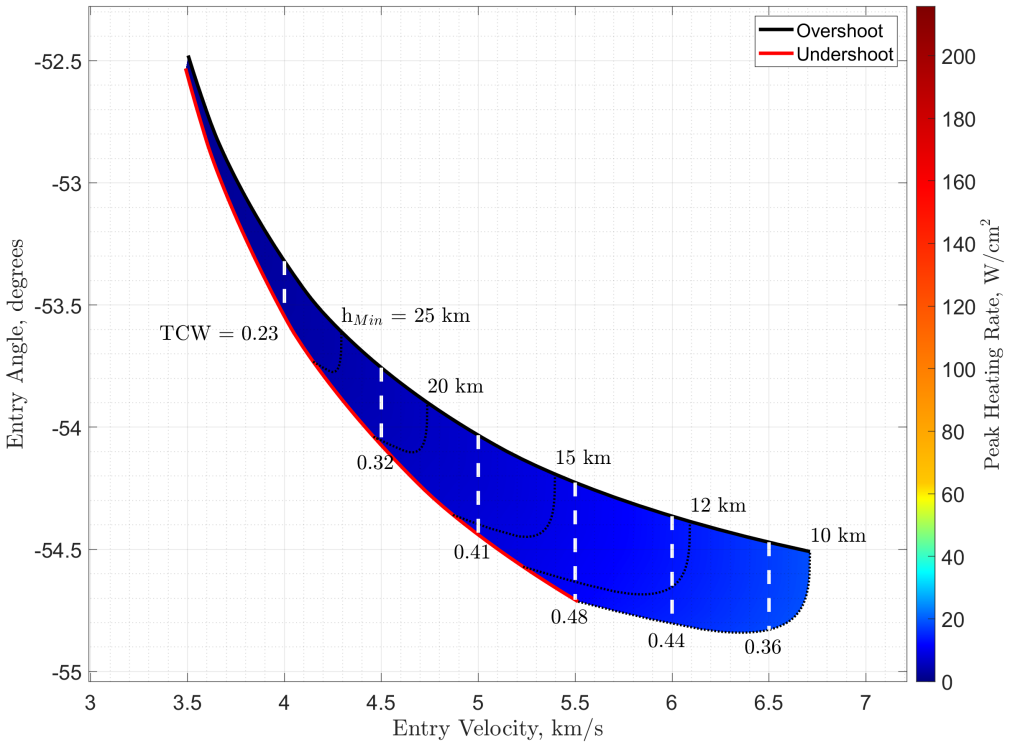


(b) $V_{\infty,out}$ = 2.0 km/s

Figure 6.11: Corridor width for a target outbound excess speed of 2.0 km/s.

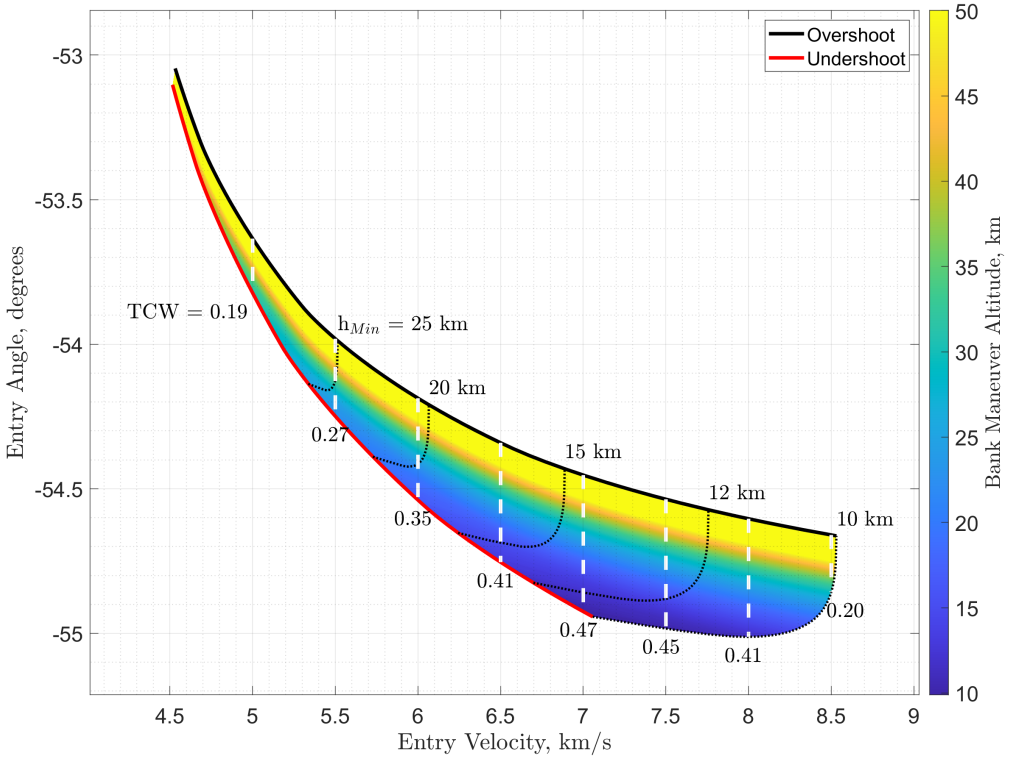


(a) $V_{\infty,out}$ = 3.0 km/s

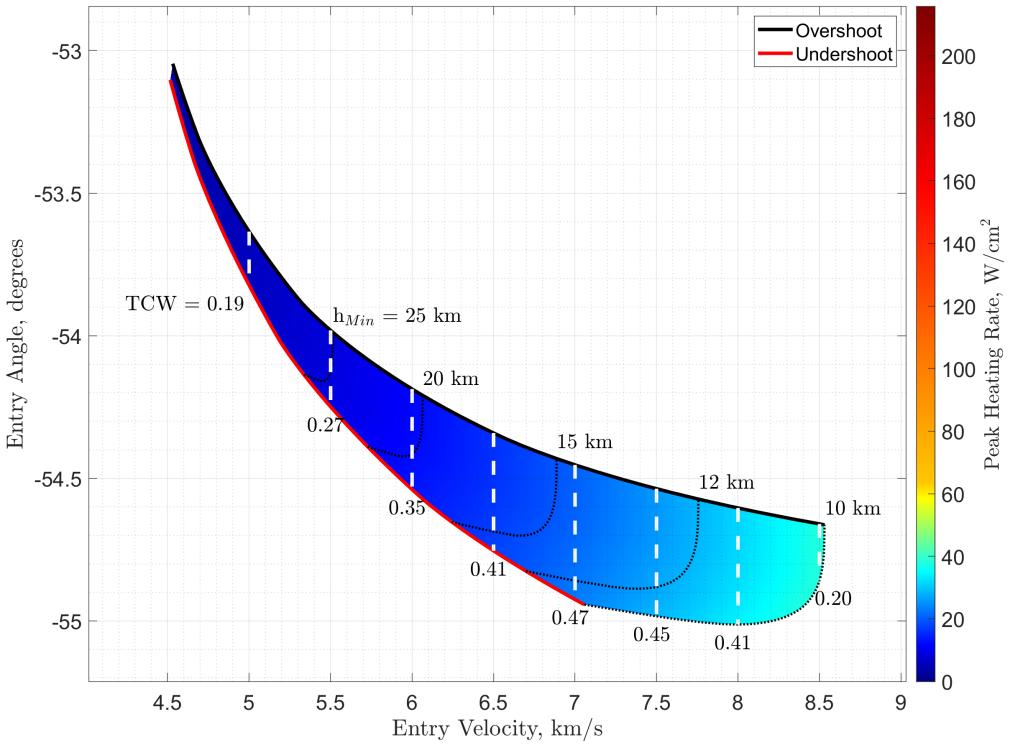


(b) $V_{\infty,out}$ = 3.0 km/s

Figure 6.12: Corridor width for a target outbound excess speed of 3.0 km/s.

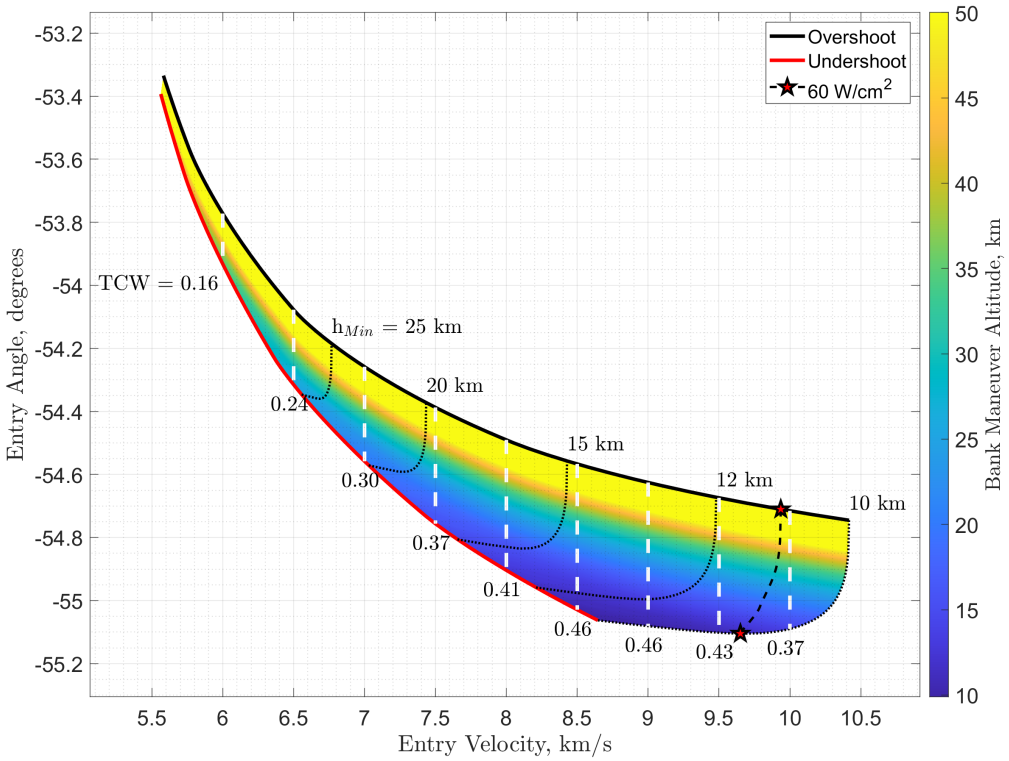


(a) $V_{\infty,out}$ = 4.0 km/s

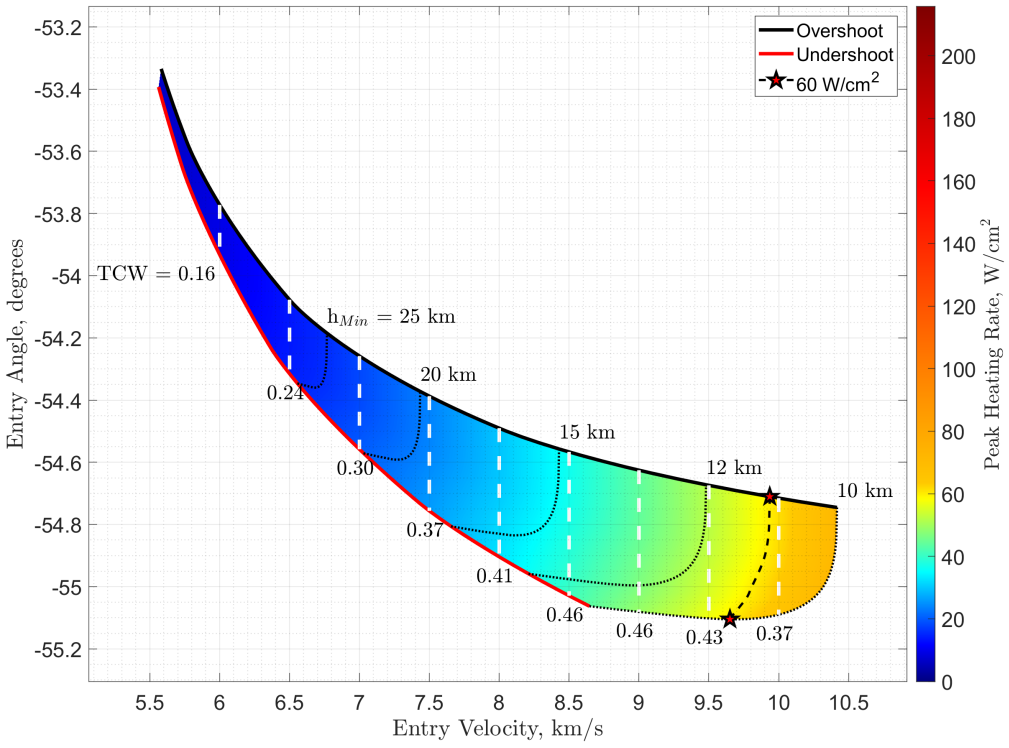


(b) $V_{\infty,out}$ = 4.0 km/s

Figure 6.13: Corridor width for a target outbound excess speed of 4.0 km/s.

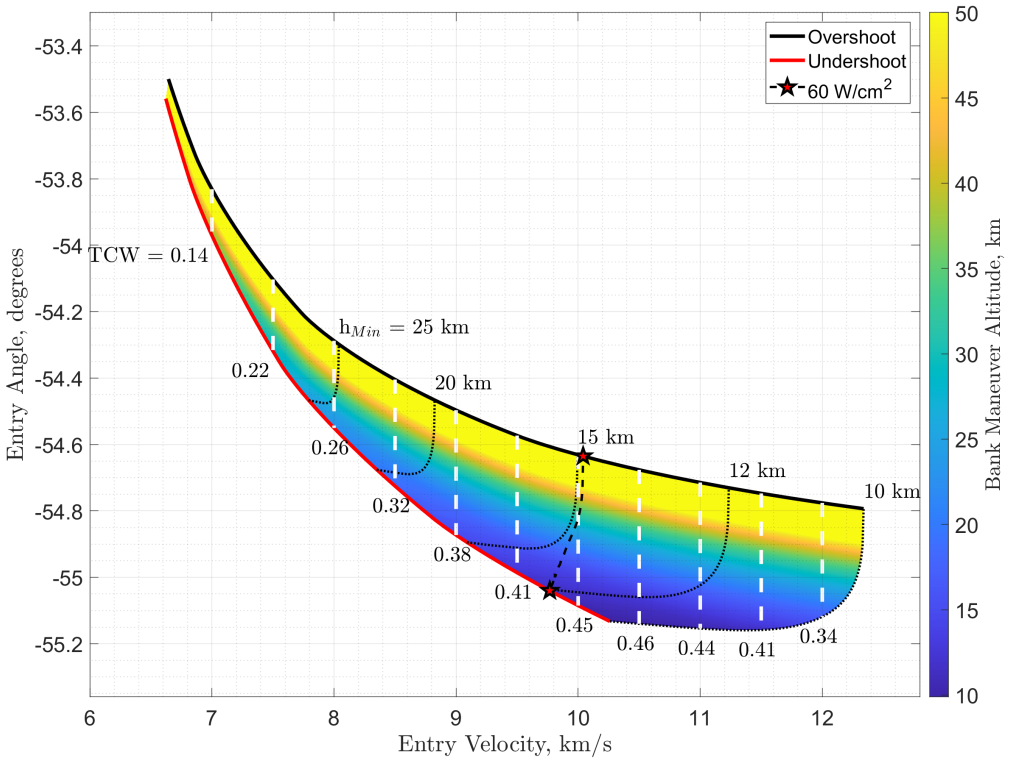


(a) $V_{\infty,out} = 5.0$ km/s

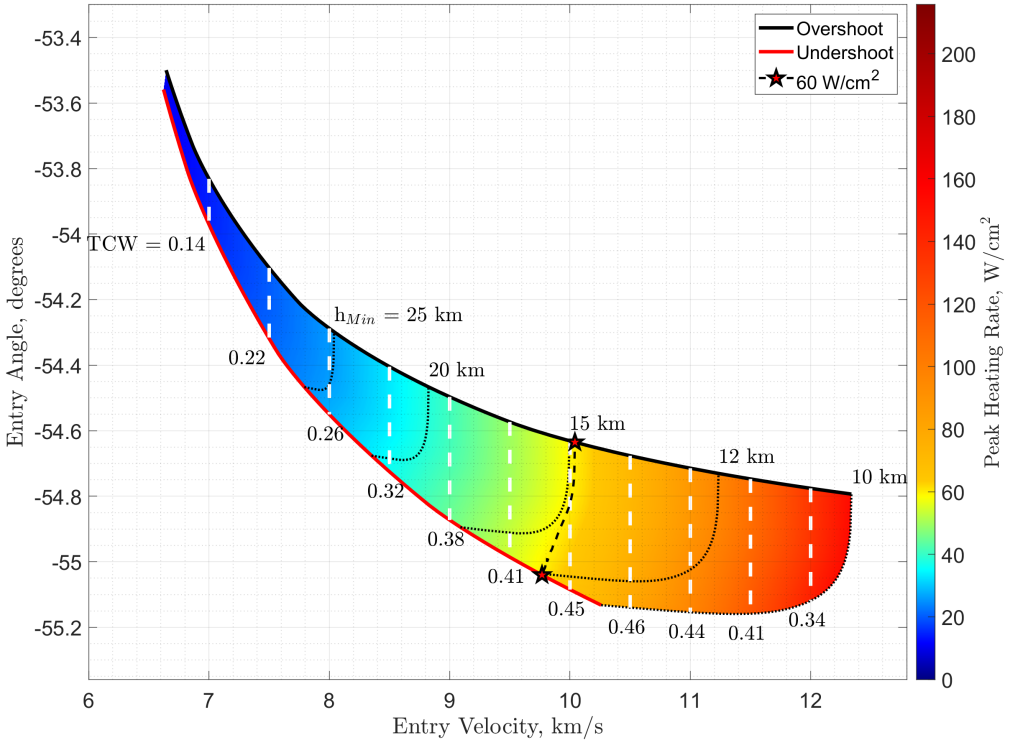


(b) $V_{\infty,out} = 5.0$ km/s

Figure 6.14: Corridor width for a target outbound excess speed of 5.0 km/s.

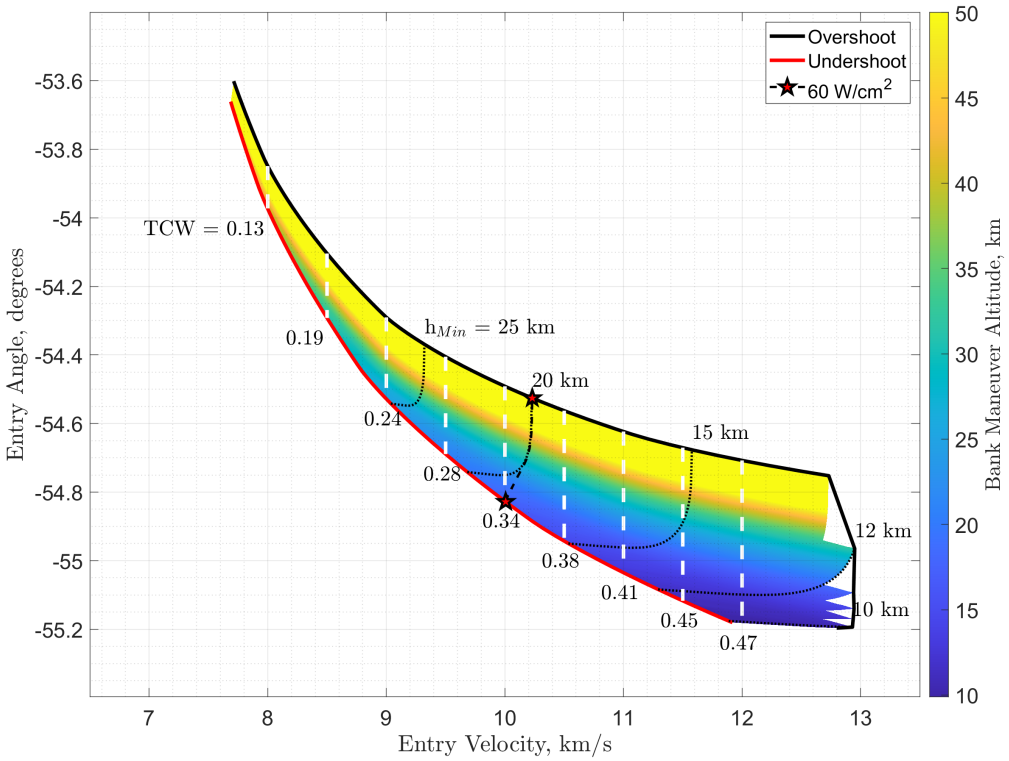


(a) $V_{\infty,out} = 6.0$ km/s

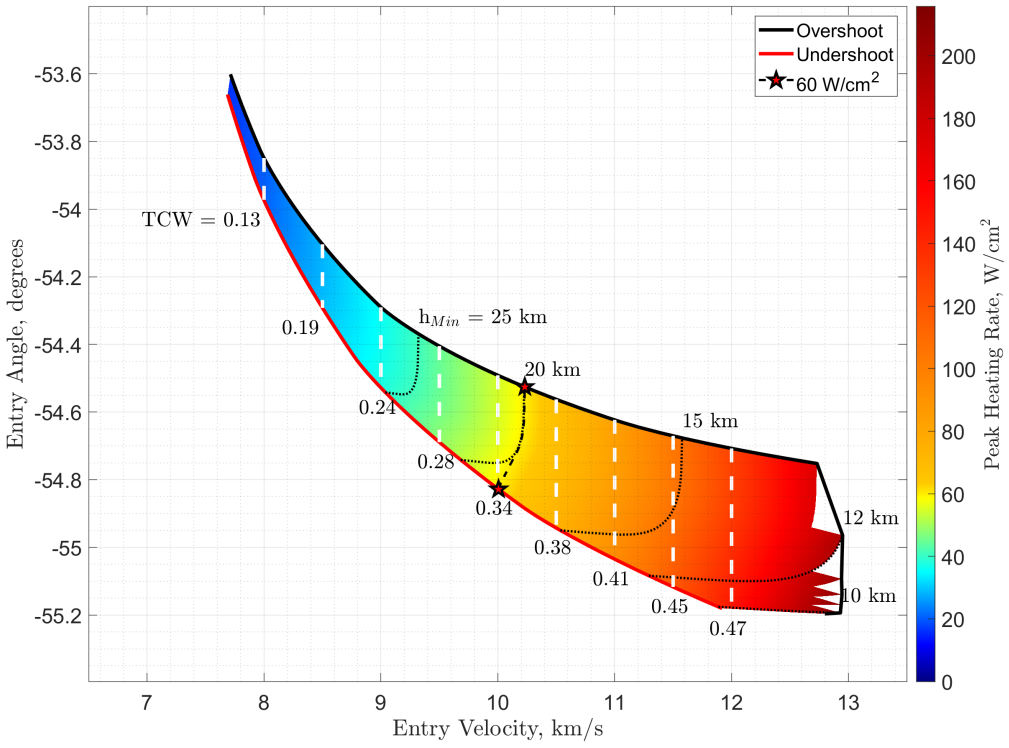


(b) $V_{\infty,out} = 6.0$ km/s

Figure 6.15: Corridor width for a target outbound excess speed of 6.0 km/s.



(a) $V_{\infty,out}$ = 7.0 km/s



(b) $V_{\infty,out}$ = 7.0 km/s

Figure 6.16: Corridor width for a target outbound excess speed of 7.0 km/s.

can enter and still reach the outbound velocity. The dotted black lines indicate different minimum altitude thresholds (with associated altitude label placed above the overshoot boundary). The dashed white lines show potential corridor widths for combinations of desired outbound excess speed and entry velocity (with associated corridor width label placed below the undershoot boundary). The gradient fill seen in Fig. 6.11a - 6.16a represents the altitude at which the bank maneuver was performed while the gradient fill in Fig. 6.11b - 6.16b shows the associated total peak heat rate. In Fig. 6.14, 6.15, and 6.16 there is an extra, black, dashed line (demarcated by red stars outlined in black) that show when the peak stagnation point heat rate exceeds the 60 W/cm^2 constraint of the LOFTID aeroshell.

For entry conditions above the black lines describing the overshoot boundaries, not enough energy dissipation occurs and the outbound excess speed will be too high. Conversely, entry conditions below the red line defining the undershoot boundary dissipate too much energy resulting in an outbound velocity that is too low. Lastly, a combination of entry conditions falling below the dotted black line for the 10 km minimum altitude will produce a trajectory that penetrates too low into the atmosphere, breaking the altitude constraint.

Features near an entry velocity of 3 km/s in Fig. 6.11 and above ∼12.6 km/s in Fig. 6.16 clearly indicate the edge of the parameter sweeps. The jagged edges indicate the boundaries of the entry velocity range and should be neglected. The range of entry conditions need to be extended to resolve the results in those regions.

In general, the lower minimum allowed altitude, the wider the entry corridor. The corridor width as a function of entry velocity for constant outbound excess velocity is plotted in Fig. 6.17. The peaks for the curves was surprisingly similar occurring between ∼0.45° to ∼0.48°. The width of each curve however, increases for increasing outbound velocities indicating higher entry velocities provide better options for meeting corridor requirements.

While these results are encouraging it should be noted that trajectories simulated in this study only reach a corridor width nearly half of the often cited 1° requirement.

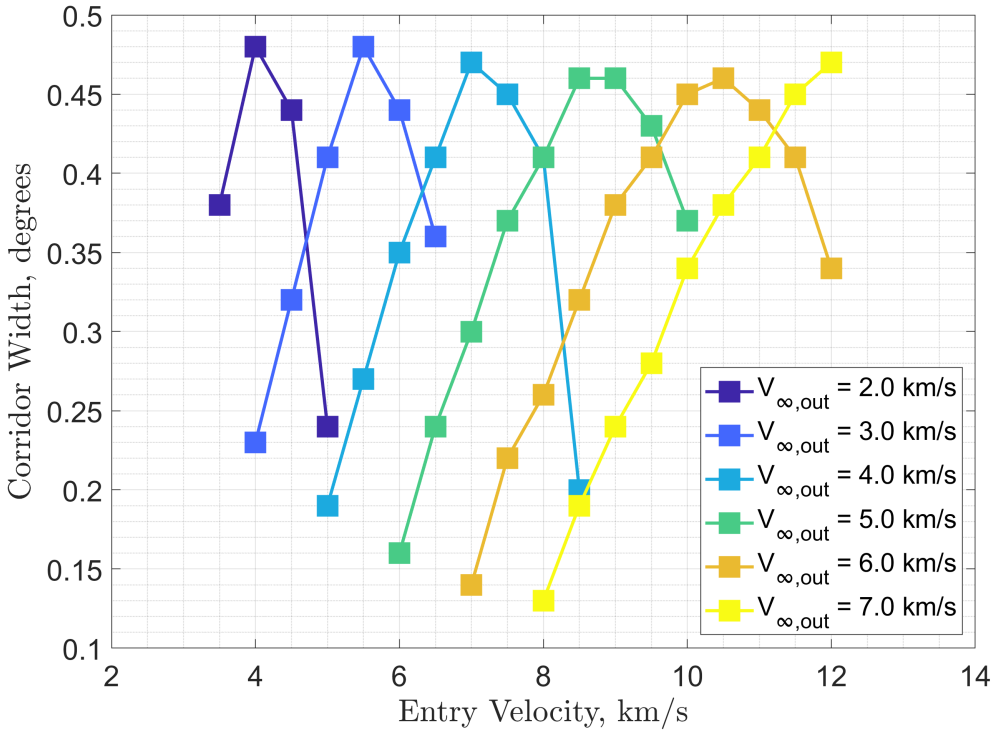


Figure 6.17: Corridor width as a function of atmospheric entry velocity for lines of constant outbound excess speed.

Other aerocapture studies have achieved much larger corridor widths; examples include a width of greater than 4° reported by Lyne[75] for aerocapture at Mars, 2.27° and 3.5° at Neptune and Titan, respectively, reported by Lockwood[5].

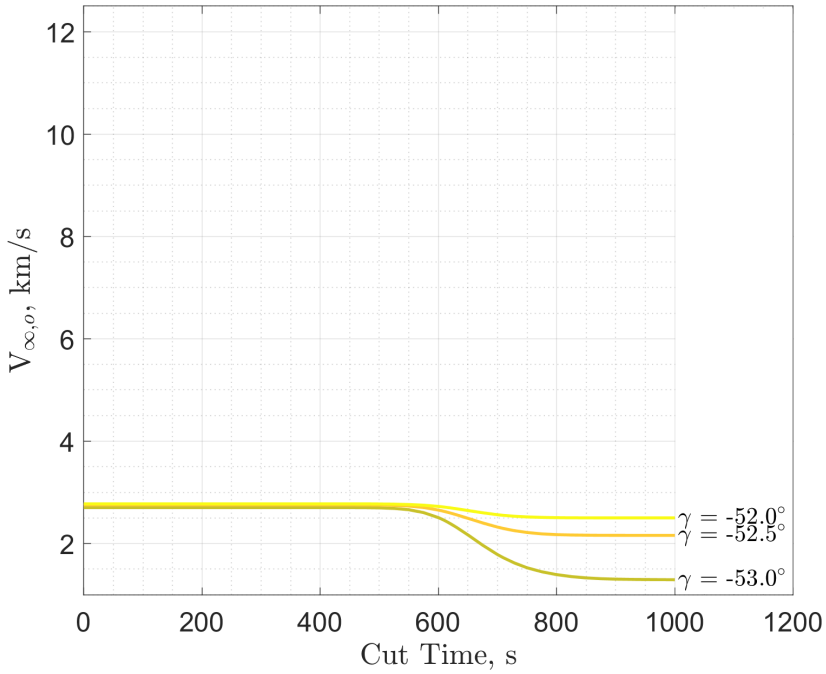
6.4 Jettisoning Trajectories

The jettisoning trajectories covered a range of entry velocities between 3 km/s and 12.95 km/s and entry angles between -56.0° and -52.0°. The range of entry angles was slightly narrowed based on the results from the ballistic trajectories. This was done to focus on trajectories that would most likely be effected by the jettisoning, as well as reducing the computational expense. For each set of entry conditions a cut time was defined that would change the vehicle's mass and surface area instantaneously. Since the cut time was based solely on time elapsed from atmospheric entry, its effect varied widely and required numerous sweeps to be conducted.

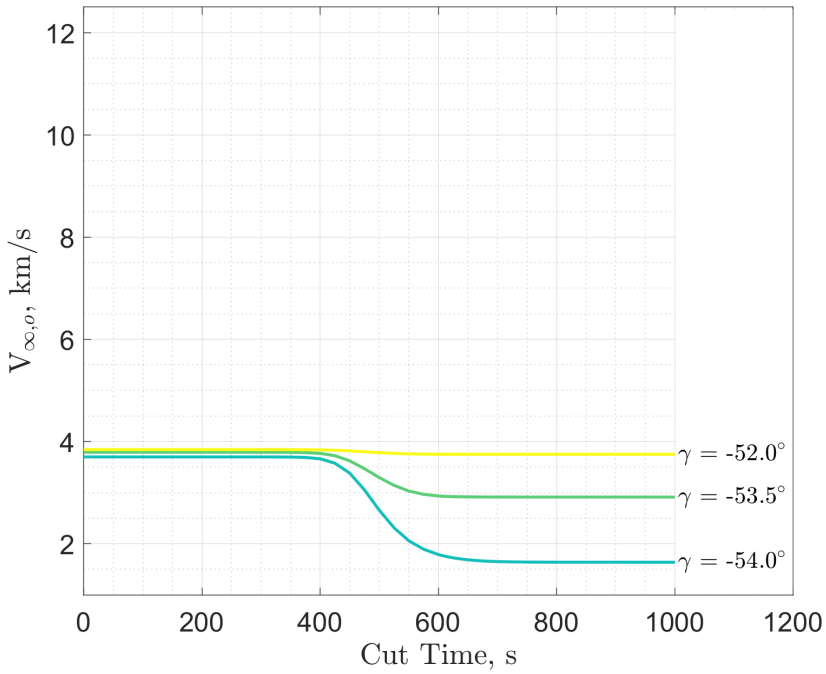
The influence of cut time is illustrated in Fig. 6.18 through 6.22 which show the outbound excess velocity as a function of cut time for specific entry velocities and lines of constant entry angle. Figure 6.23 and 6.24 show the the outbound excess velocity as a function of cut time for specific entry angles and lines of constant entry velocity.

For each combination of entry velocity and entry angle there appear to be three distinct regions. The left region (early cut times) shows a constant outbound velocity representing the maximum outbound energy (or minimum energy dissipation) for those particular entry conditions. The right region (late cut times) shows another portion of constant outbound velocity but represents a minimum outbound energy characterized by the maximum amount of energy dissipation for a set of entry conditions. This is caused by the vehicle having traversed the portion of the atmosphere where the density profile is high enough to cause significant aerodynamic forces before the skirt is released. The middle region (intermediate cut times) occur when the drag device is released lower in the atmosphere where the aerodynamics still has an effect on the trajectory. These three regions show a range of reachable outbound velocities as a function of when the drag device is jettisoned.

The general trends suggest that steep, high velocity entries cause the vehicle to penetrate deeper into the atmosphere allowing more energy dissipation through aerodynamic forces. Shallow, low speed entries don't reach lower altitudes where density is high enough to dissipate energy. These statements appear to be substantiated by the curves shown in Fig. 6.25 which show jettisoning of the drag device has little influence on the minimum altitude achieved. However, as a reminder, all of the jettisoning trajectories have assumed a ballistic trajectory. Future studies should include lifting and maneuvering trajectories to explore how the instantaneous change in aerodynamics effects minimum altitude and energy dissipation.

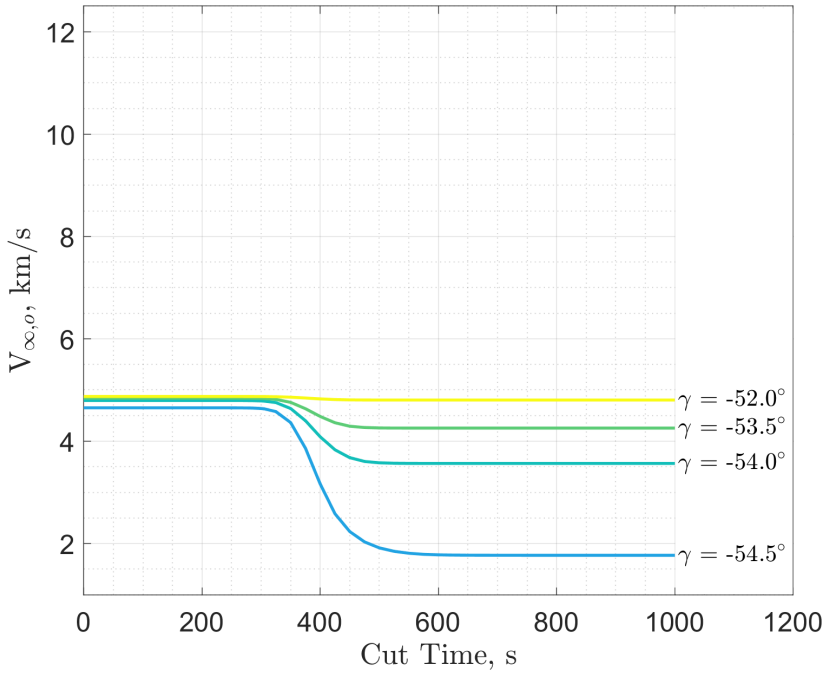


(a) V_{En} = 3.0 km/s

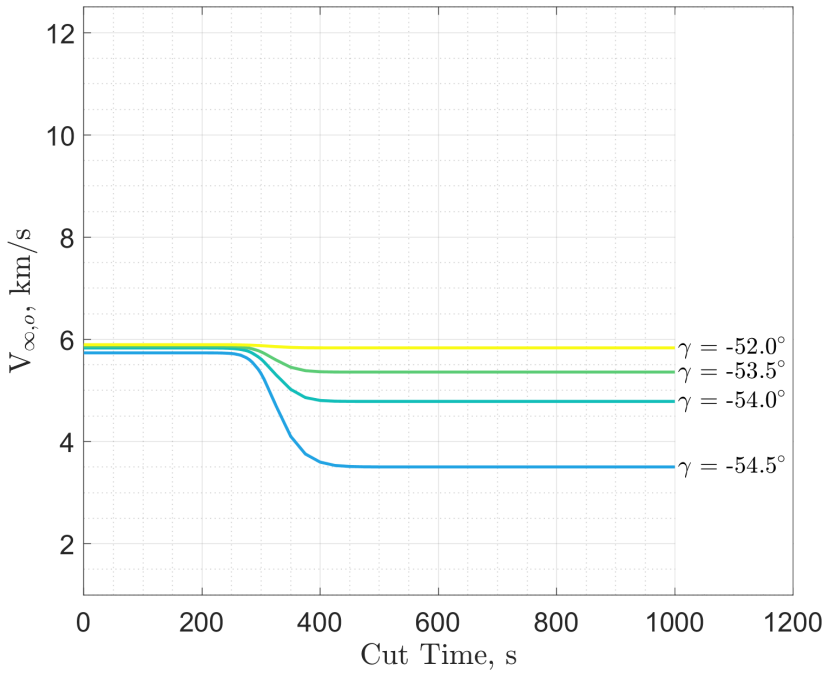


(b) V_{En} = 4.0 km/s

Figure 6.18: Outbound excess velocity as a function of cut time for lines of constant entry angle and entry velocities of 3 and 4 km/s.

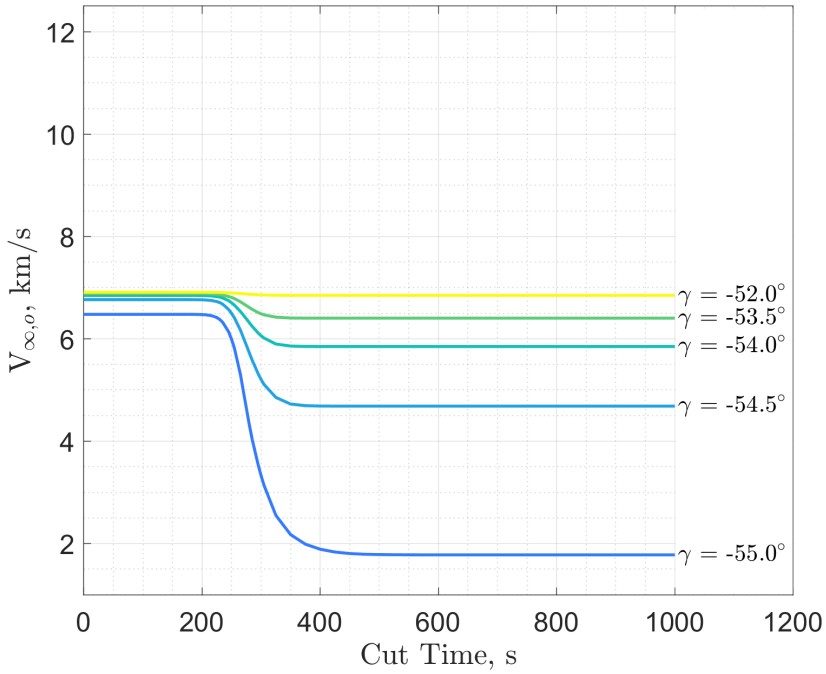


(a) V_{En} = 5.0 km/s

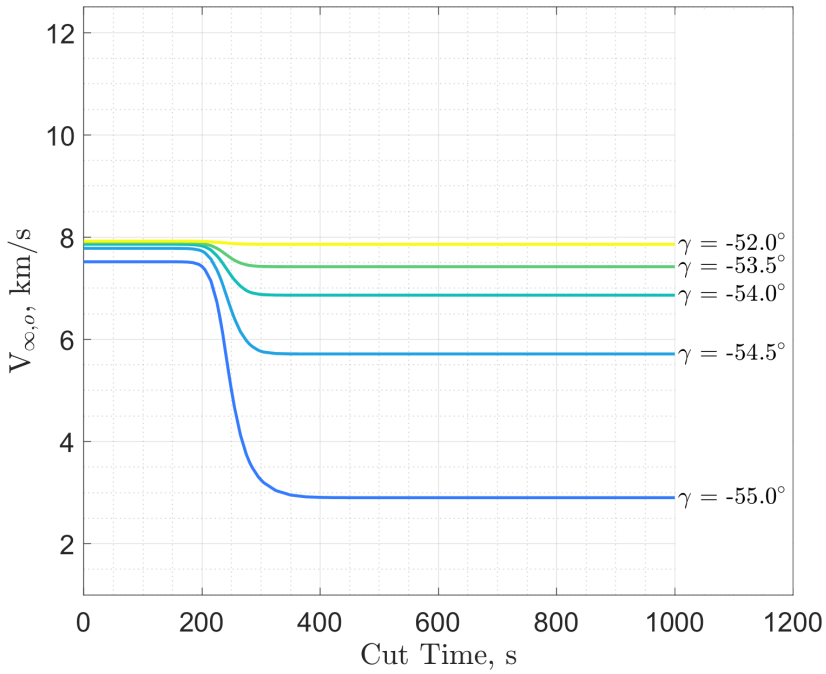


(b) V_{En} = 6.0 km/s

Figure 6.19: Outbound excess velocity as a function of cut time for lines of constant entry angle and entry velocities of 5 and 6 km/s.

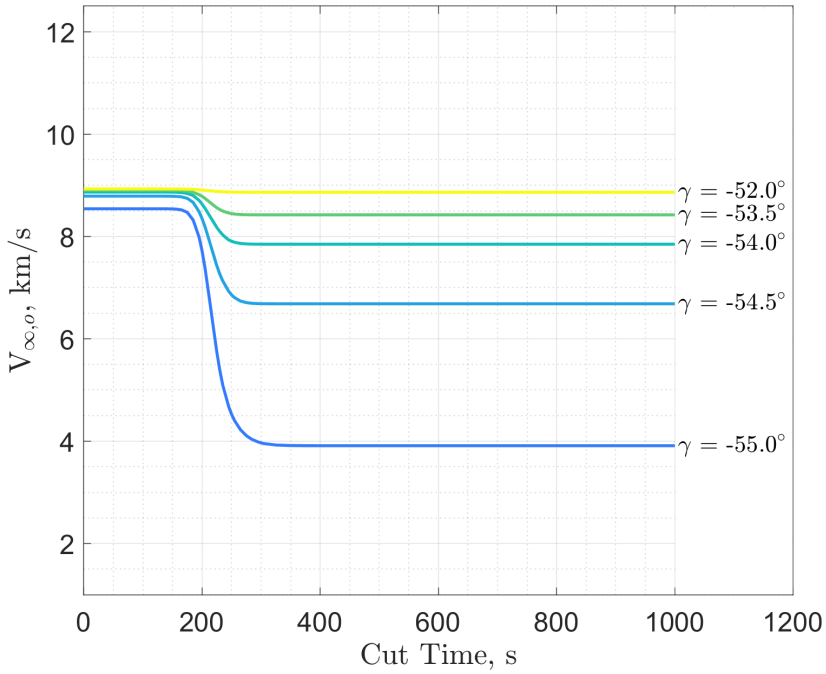


(a) V_{En} = 7.0 km/s

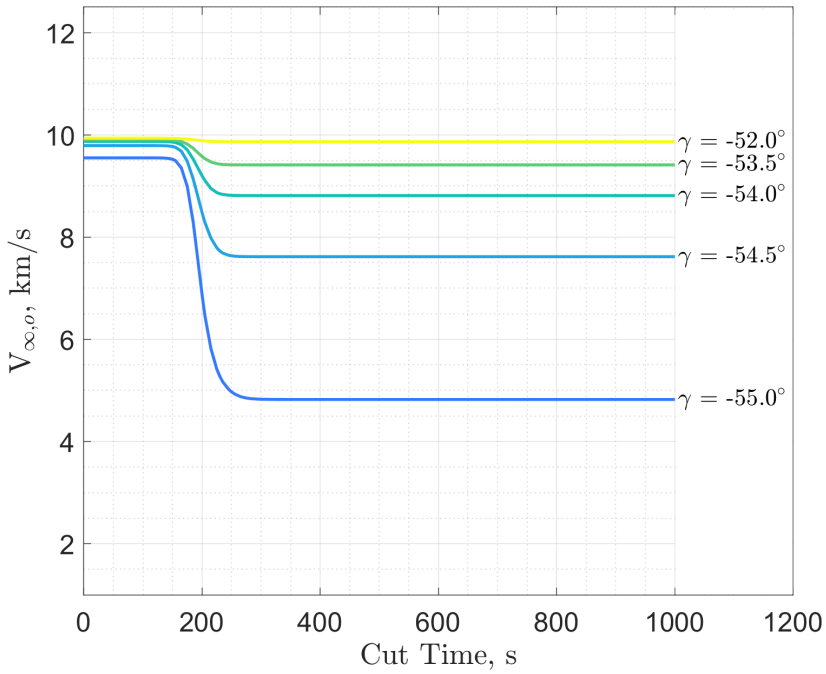


(b) V_{En} = 8.0 km/s

Figure 6.20: Outbound excess velocity as a function of cut time for lines of constant entry angle and entry velocities of 7 and 8 km/s.

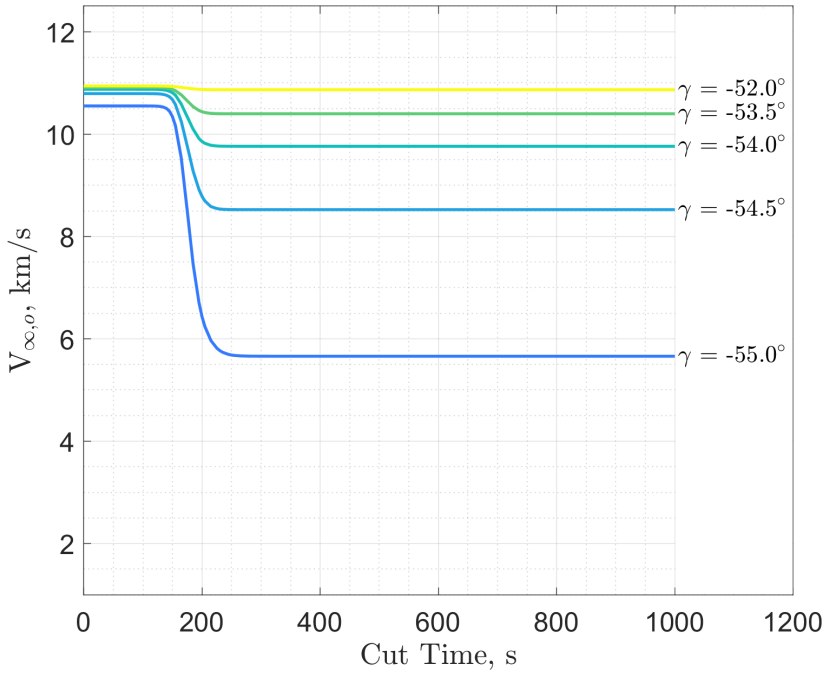


(a) V_{En} = 9.0 km/s

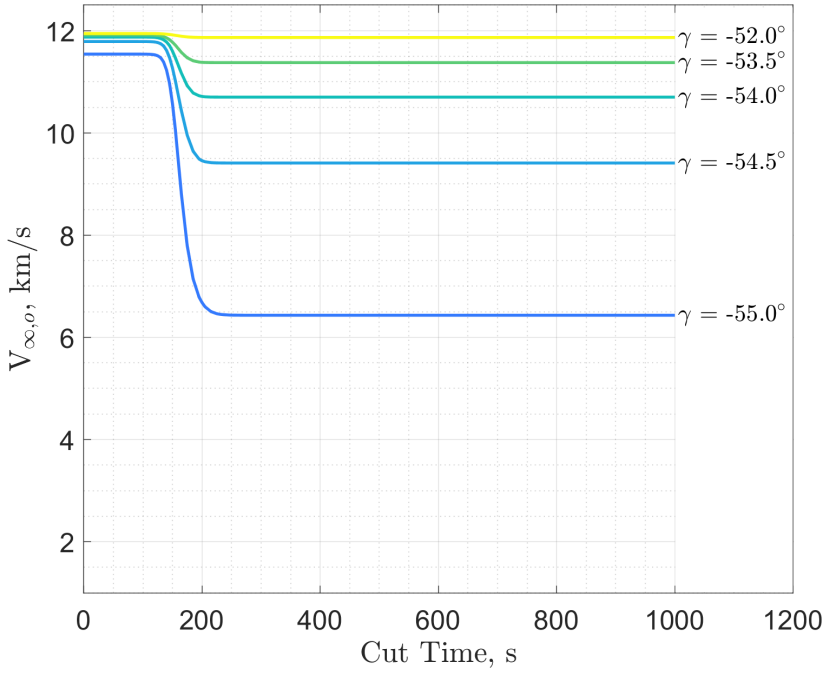


(b) V_{En} = 10.0 km/s

Figure 6.21: Outbound excess velocity as a function of cut time for lines of constant entry angle and entry velocities of 9 and 10 km/s.

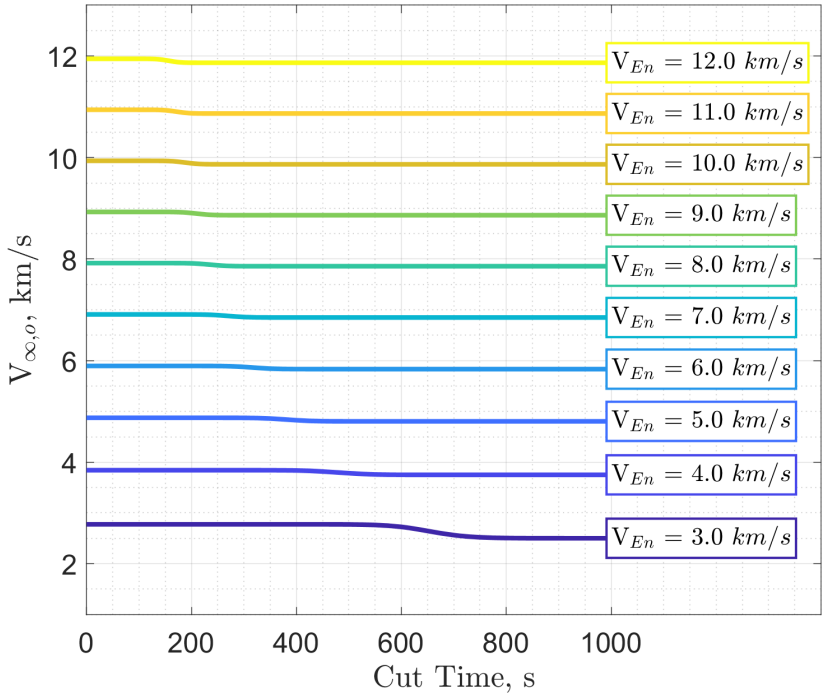


(a) V_{En} = 11.0 km/s

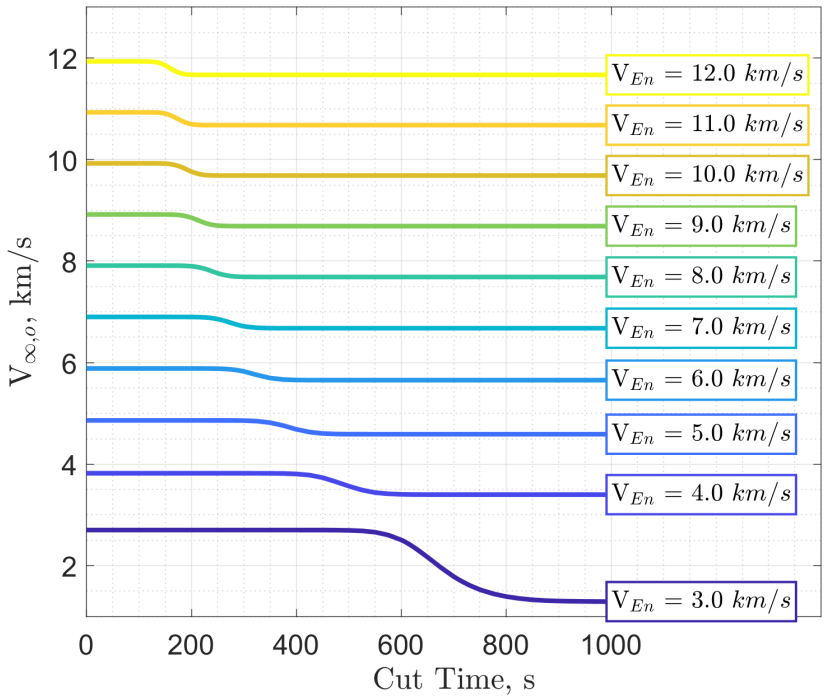


(b) V_{En} = 12.0 km/s

Figure 6.22: Outbound excess velocity as a function of cut time for lines of constant entry angle and entry velocities of 11 and 12 km/s.

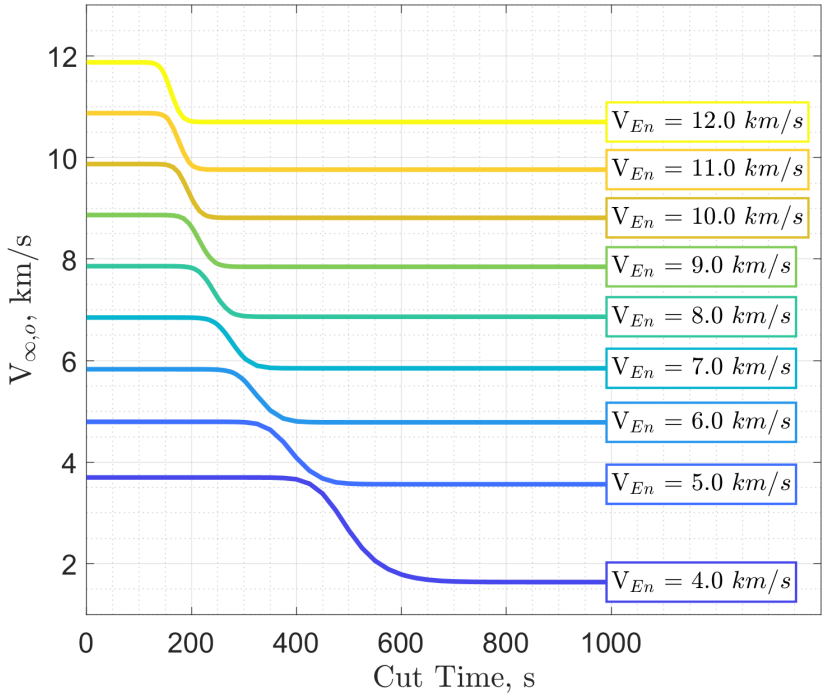


(a) γ_{En} = -52.0°

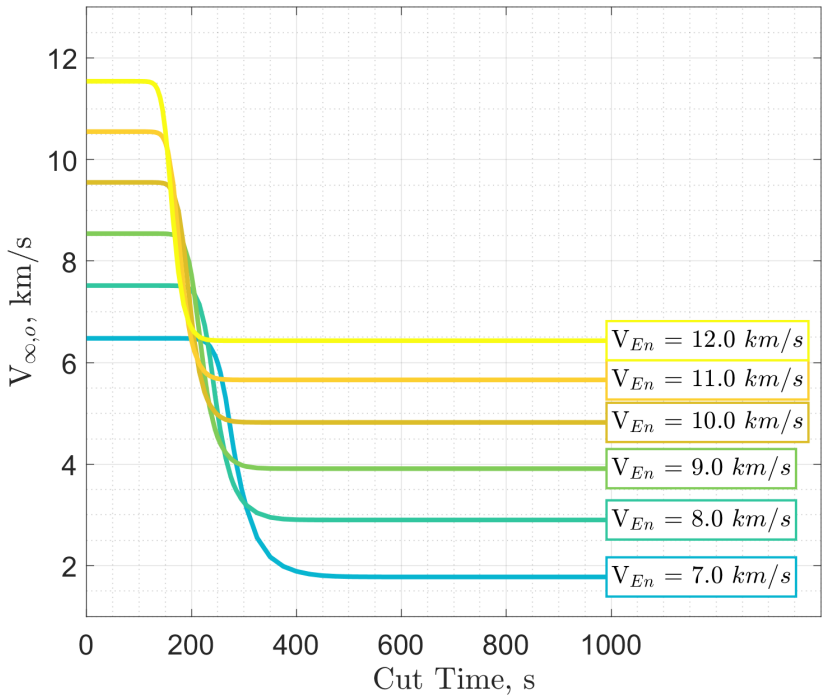


(b) γ_{En} = -53.0°

Figure 6.23: Outbound excess velocity as a function of cut time for lines of constant entry velocity and entry angles of -52.0° and -53.0°.

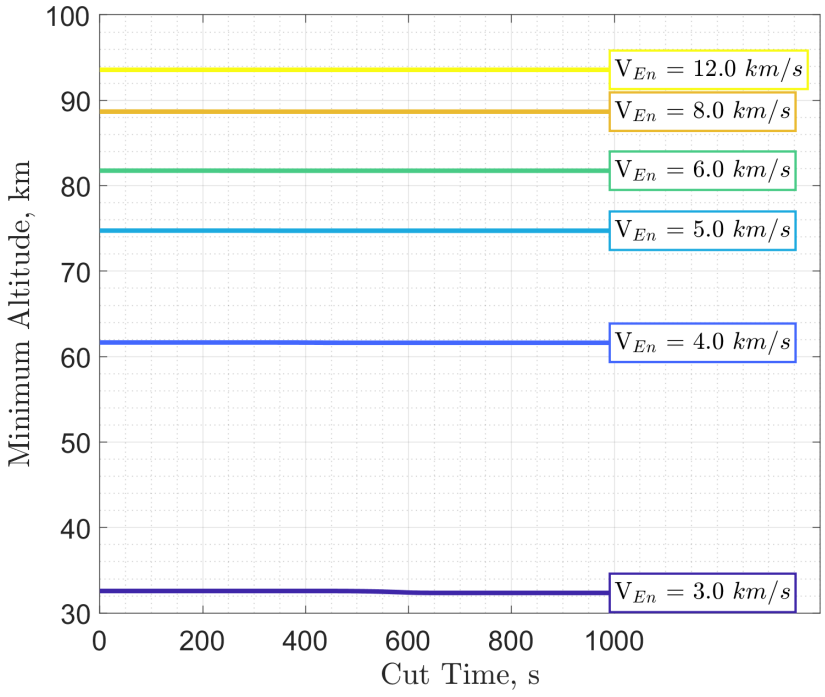


(a) γ_{En} = -54.0°

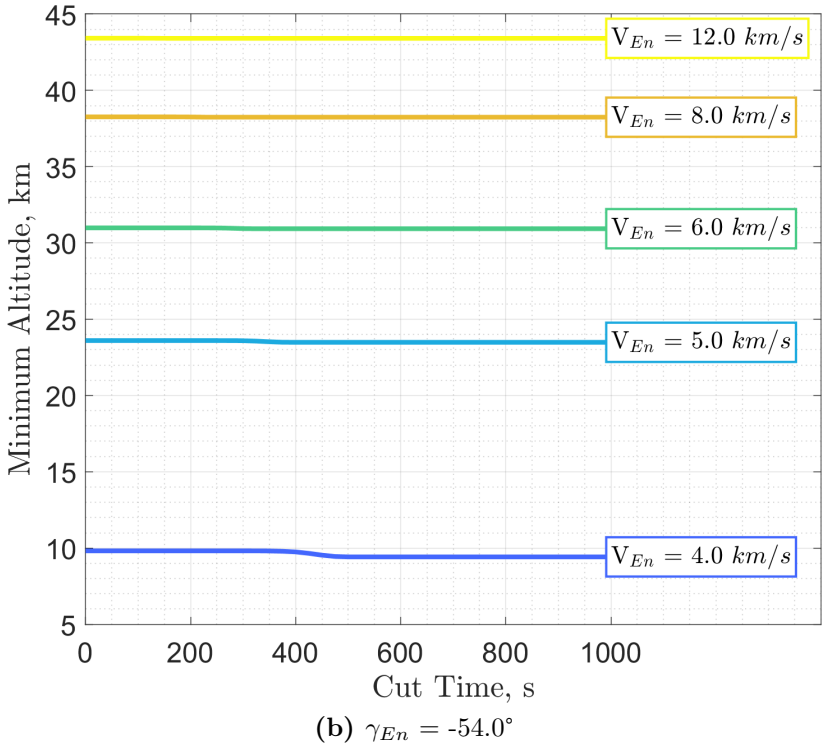


(b) γ_{En} = -55.0°

Figure 6.24: Outbound excess velocity as a function of cut time for lines of constant entry velocity and entry angles of -54.0° and -55.0°.



(a) γ_{En} = -52.5°



(b) γ_{En} = -54.0°

Figure 6.25: Minimum altitude as a function of cut time for lines of constant entry velocity and entry angles of -52.5°and -54.0°.

Chapter 7

Conclusions

Numerical simulations of atmospheric trajectories have been used in the current study to explore the feasibility of a successful AGA maneuver at Triton. Unlike the high ballistic coefficient vehicles with towed ballutes from the previous studies[11, 12, 15], the current research uses a low ballistic coefficient vehicle resembling that of the vehicle used in the LOFTID test. A wide range of entry conditions, bank maneuver altitude, and ballute cut time were used, resulting in millions of atmospheric trajectories. By comparison, the previous study produced only a small fraction of the trajectories on which to base the AGA maneuver.

Additionally, to the author's knowledge, the simulated trajectories contained herein are the first to use the performance characteristics of an inflatable, clamped ballute, which has been flight proven, to dissipate energy in Triton's atmosphere during an AGA maneuver. Also, no other studies were found that used the density profile derived by Strobel[39] to perform an analysis of atmospheric trajectories. Although tenuous, Triton's atmosphere shows the ability to provide significant energy dissipation in without violating minimum altitude or vehicle constraints when atmospheric entry velocities are less than 9.5 km/s. Using a reference atmospheric interface of 1029 km, peak corridor widths are estimated to be $\sim$0.48°.

A primary limitation of the current study is that the results only focused on the Triton centric phase of the trajectory. Without specific arrival and departure conditions in Triton's reference frame it is difficult to determine how much adjustment is needed during the Triton flyby. However, the wide range of trajectories simulated from this research describes Triton's capacity for altering a trajectory and can be used as targeted constraints for planning Earth launch dates and Neptune orbital insertion. The latter is especially important since substantial changes in the Triton-centered arrival excess speed can be effected by small changes in encounter date due to Triton's short orbital period.

Further limitations of the current study lie in the need for more sophisticated aerodynamic manipulation in Triton's atmosphere. Future studies should include GNC routines that provide optimized maneuvering and the ability to combine different drag devices (ballutes + MHD + aerocapture tether). Combined methods of drag augmentation, especially through MHD, have the potential to dissipate energy higher in the atmosphere and experiencing lower peak heating rates.

The body of work presented for this research is encouraging and provides several preliminary findings that warrant continued investigation into the feasibility of performing an AGA maneuver at Triton. Reducing the aforementioned limitations through further studies will help to confirm or refute the feasibility of a Triton AGA maneuver for a Neptune orbital insertion.

Bibliography

[1] Frazier, W., Bearden, D., Mitchell, K. L., Lam, T., Prockter, L., and Dissly, R., "Trident: The Path to Triton on a Discovery Budget," *2020 IEEE Aerospace Conference*, 2020, pp. 1–12. https://doi.org/10.1109/AERO47225.2020.9172502. 2

[2] Rymer, A. M., Runyon, K. D., Clyde, B., Núñez, J. I., Nikoukar, R., Soderlund, K. M., Sayanagi, K., Hofstadter, M., Quick, L. C., Stern, S. A., Becker, T., Hedman, M., Cohen, I., Crary, F., Fortney, J. J., Vertesi, J., Hansen, C., de Pater, I., Paty, C., Spilker, T., Stallard, T., Hospodarsky, G. B., Smith, H. T., Wakeford, H., Moran, S. E., Annex, A., Schenk, P., Ozimek, M., Arrieta, J., McNutt, R. L., Masters, A., Simon, A. A., Ensor, S., Apland, C. T., Bruzzi, J., Patthoff, D. A., Scott, C., Campo, C., Krupiarz, C., Cochrane, C. J., Gantz, C., Rodriguez, D., Gallagher, D., Hurley, D., Crowley, D., Abel, E., Provornikova, E., Turtle, E. P., Clark, G., Wilkes, J., Hunt, J., Roberts, J. H., Rehm, J., Murray, K., Wolfarth, L., Fletcher, L. N., Spilker, L., Martin, E. S., Parisi, M., Norkus, M., Izenberg, N., Stough, R., Vervack, R. J., Mandt, K., Stevenson, K. B., Kijewski, S., Cheng, W., Feldman, J. D., Allen, G., Prabhu, D., Dutta, S., Young, C., and Williams, J., "Neptune Odyssey: A Flagship Concept for the Exploration of the Neptune–Triton System," *The Planetary Science Journal*, Vol. 2, No. 5, 2021, p. 184. https://doi.org/10.3847/PSJ/abf654, URL https://dx.doi.org/10.3847/PSJ/abf654. 2

[3] Hall, J. L., Noca, M. A., and Bailey, R. W., "Cost-Benefit Analysis of the Aerocapture Mission set," *Journal of Spacecraft and Rockets*, Vol. 42, No. 2, 2005, pp. 309–320. https://doi.org/10.2514/1.4118, URL https://doi.org/10.2514/1.4118. 3, 7

[4] Noca, M., and Bailey, R., "Mission trades for aerocapture at Neptune," *40th AIAA/ASME/SAE/ASEE Joint Propulsion Conference and Exhibit*, 2004. 8

[5] Lockwood, M. K., "Neptune Aerocapture Systems Analysis," *AIAA Atmospheric Flight Mechanics Conference and Exhibit*, 2004. https://doi.org/10.2514/6.2004-4951, URL https://doi.org/10.2514/6.2004-4951. 3, 8, 13, 29, 59

[6] Dutta, S., "Aerocapture as an Enhancing Option for Ice Giants Missions," *White Paper*, Vol. 53, No. 4, 2021. https://doi.org/10.3847/25c2cfeb.e8e49d0e, URL https://doi.org/10.3847/25c2cfeb.e8e49d0e.

[7] Spilker, T. R., Adler, M., Arora, N., Beauchamp, P. M., Cutts, J. A., Munk, M. M., Powell, R. W., Braun, R. D., and Wercinski, P. F., "Qualitative Assessment of Aerocapture and Applications to Future Missions," *Journal of Spacecraft and Rockets*, Vol. 56, No. 2, 2019, pp. 536–545. https://doi.org/10.2514/1.a34056. 3, 9

[8] Starr, B., Westhelle, C., and Masciarelli, J., "Aerocapture Performance Analysis for a Neptune-Triton Exploration Mission," *AIAA Atmospheric Flight Mechanics Conference and Exhibit*, American Institute of Aeronautics and Astronautics, Reston, Virigina, 2004.

[9] Girija, A. P., Saikia, S. J., Longuski, J. M., Bhaskaran, S., Smith, M. S., and Cutts, J. A., "Feasibility and performance analysis of Neptune aerocapture using heritage blunt-body aeroshells," *J. Spacecr. Rockets*, Vol. 57, No. 6, 2020, pp. 1186–1203. 8

[10] Girija, A. P., Saikia, S. J., Longuski, J. M., Lu, Y., and Cutts, J. A., "Quantitative assessment of aerocapture and applications to future solar system exploration," *J. Spacecr. Rockets*, Vol. 59, No. 4, 2022, pp. 1074–1095. 3, 8

[11] Ramsey, P., and Lyne, J. E., "An Investigation of Aerogravity Assist at Titan and Triton for Capture into Orbit About Saturn and Neptune," *2nd International Planetary Probe Workshop*, 2004. URL https://ntrs.nasa.gov/citations/20070014620. 3, 9, 18, 20, 24, 29, 69

[12] Ramsey, P., and Lyne, J. E., "A Preliminary Investigation of Aerogravity Assist at Triton for Capture into Orbit About Neptune," *3rd International Planetary Probe Workshop*, 2005. URL https://www.researchgate.net/publication/265325158. 3, 9, 18, 20, 24, 29, 69

[13] Curtis, H. D., "Orbital mechanics for engineering students," *Choice Reviews Online*, Vol. 42, No. 11, 2005, pp. 42–6517. https://doi.org/10.5860/choice.42-6517, URL https://doi.org/10.5860/choice.42-6517. 8

[14] Randolph, J. E., and McRonald, A., "Solar system 'fast mission' trajectories using aerogravity assist," *Journal of Spacecraft and Rockets*, Vol. 29, No. 2, 1992, pp. 223–232. https://doi.org/10.2514/3.26338. 9

[15] Ramsey, P. E., and Lyne, J. E., "Investigation of Titan Aerogravity Assist for Capture into Orbit About Saturn," *Journal of Spacecraft and Rockets*, Vol. 43, No. 1, 2006, pp. 231–233. https://doi.org/10.2514/1.9274. 9, 18, 20, 24, 69

[16] Ramsey, P. E., and Lyne, J. E., "Enceladus Mission Architecture using Titan Aerogravity assist for orbital capture about Saturn," *Journal of Spacecraft and Rockets*, Vol. 45, No. 3, 2008, pp. 635–638. https://doi.org/10.2514/1.31362.

[17] Spilker, T. R., Moeller, R., Borden, C., Smythe, W. D., Lock, R. E., Elliott, J., Wertz, J., and Strange, N., "Analysis of architectures for the scientific exploration

of Enceladus," *IEEE Aerospace Conference*, 2009. https://doi.org/10.1109/aero.2009.4839317, URL https://doi.org/10.1109/aero.2009.4839317.

[18] Arnold, J., Spilker, T. R., Cornelius, D. M., Allen, J., G. A., Brandis, A. M., Saunders, D. A., Qu, M., Powell, R. W., Cable, M. L., and Beck, R. A. S., "Heatshields for Aerogravity Assist Vehicles Whose Deceleration at Titan Saves Mass for Future Flagship Class Exploration of Enceladus," *Bulletin of the American Astronomical Society*, Vol. 53, 2021, p. 382. https://doi.org/10.3847/25c2cfeb.0e2cd545.

[19] Tackett, B., Powell, R., Dutta, S., Lugo, R., and Engel, D., "Guidance and Control Approaches that Enable Titan Aerogravity Assist for an Enceladus Mission," *Bulletin of the American Astronomical Society*, Vol. 53, 2021, p. 489. https://doi.org/10.3847/25c2cfeb.2f67f375.

[20] Lu, Y., and Saikia, S. J., "Titan aerogravity-assist maneuvers for Saturn/Enceladus missions," *Acta Astronautica*, Vol. 176, 2020, pp. 262–275. https://doi.org/10.1016/j.actaastro.2020.06.001, URL https://doi.org/10.1016/j.actaastro.2020.06.001. 9

[21] Horsewood, J. L., "MAnE v3.5," , 2024. URL https://spaceflightsolutions.com/. 10

[22] Horsewood, J. L., "MAnE Mission Analysis Environment for Heliocentric High-Thrust Missions: Mathematical Formulation," , 2013. URL https://spaceflightsolutions.com/. 10

[23] Brisby, J. D., and Lyne, J. E., "Triton Aerogravity assist using a Flight-Proven, inflatable aerobrake for Neptune orbit capture," *Journal of Spacecraft and Rockets*, Vol. 61, No. 4, 2024, pp. 1124–1127. https://doi.org/10.2514/1.a35964, URL https://doi.org/10.2514/1.a35964. 11, 28

[24] Schenk, P., Beddingfield, C. B., Bertrand, T., Bierson, C. J., Beyer, R. A., Bray, V. J., Cruikshank, D. P., Grundy, W. M., Hansen, C. J., Hofgartner, J. D., Martin, E. S., McKinnon, W. B., Moore, J. M., Robbins, S. J., Runyon, K. D., Singer, K. N., Spencer, J. R., Stern, S. A., and Stryk, T., "Triton: Topography and Geology of a Probable Ocean World with Comparison to Pluto and Charon," *Remote Sensing*, Vol. 13, No. 17, 2021, p. 3476. https://doi.org/10.3390/rs13173476, URL https://doi.org/10.3390/rs13173476. 15

[25] NASA/JPL, "Triton," , 2019. URL https://noirlab.edu/public/images/gemini1903a/, [Online; accessed April 7, 2024]. 15, 16

[26] Tyler, G. L., Sweetnam, D. N., Anderson, J. D., Borutzki, S. E., Campbell, J. K., Eshleman, V. R., Gresh, D. L., Gurrola, E. M., Hinson, D. P., Kawashima, N., Kursinski, E. R., Levy, G. S., Lindal, G. F., Lyons, J. R., Marouf, E. A., Rosen, P. A., Simpson, R. A., and Wood, G. E., "Voyager Radio Science Observations of Neptune and Triton," *Science*, Vol. 246, No. 4936, 1989, pp. 1466–1473. https://doi.org/10.1126/science.246.4936.1466, URL http://dx.doi.org/10.1126/science.246.4936.1466. 17

[27] Broadfoot, A. L., Atreya, S. K., Bertaux, J. L., Blamont, J. E., Dessler, A. J., Donahue, T. M., Forrester, W. T., Hall, D. T., Herbert, F., Holberg, J. B., Hunter, D. M., Krasnopolsky, V. A., Linick, S., Lunine, J. I., McConnell, J. C., Moos, H. W., Sandel, B. R., Schneider, N. M., Shemansky, D. E., Smith, G. R., Strobel, D. F., and Yelle, R. V., "Ultraviolet Spectrometer Observations of Neptune and Triton," *Science*, Vol. 246, No. 4936, 1989, pp. 1459–1466. https://doi.org/10.1126/science.246.4936.1459, URL http://dx.doi.org/10.1126/science.246.4936.1459. 17

[28] Zalucha, A. M., and Cook, J., "The Structure and Dynamics of the Atmospheres of Pluto and Triton," *Oxford Research Encyclopedia of Planetary Science*, 2019. https://doi.org/10.1093/acrefore/9780190647926.013.113. 17, 18

[29] Lissauer, J., and Pater, D. I., *Fundamental Planetary Science: Physics, Chemistry and Habitability*, revised ed., Cambridge University Press, 2019. 17

[30] Elliot, J. L., and Olkin, C. B., "PROBING PLANETARY ATMOSPHERES WITH STELLAR OCCULTATIONS," *Annual review of earth and planetary sciences (Print)*, Vol. 24, No. 1, 1996, pp. 89–123. https://doi.org/10.1146/annurev.earth.24.1.89, URL https://doi.org/10.1146/annurev.earth.24.1.89. 17

[31] Yelle, R. V., Lunine, J. I., and Hunten, D. M., "Energy balance and plume dynamics in Triton's lower atmosphere," *Icarus*, Vol. 89, No. 2, 1991, pp. 347–358. https://doi.org/10.1016/0019-1035(91)90182-s, URL https://doi.org/10.1016/0019-1035(91)90182-s. 17

[32] Krasnopolsky, V. A., Sandel, B. R., Herbert, F., and Vervack, R. J., "Temperature, N2, and N density profiles of Triton's atmosphere: Observations and model," *Journal of Geophysical Research: Planets*, Vol. 98, No. E2, 1993, pp. 3065–3078. https://doi.org/10.1029/92je02680. 17

[33] Olkin, C. B., Elliot, J. L., Hammel, H. B., Cooray, A., McDonald, S. W., Foust, J. A., Bosh, A. S., Buie, M. W., Millis, R. L., Wasserman, L. H., Dunham, E. W., Young, L. A., Howell, R. R., Hubbard, W. B., Hill, R. E., Marcialis, R. L., McDonald, J. S., Rank, D. M., Holbrook, J., and Reitsema, H. J., "The Thermal Structure of Triton's Atmosphere: Results from the 1993 and 1995 Occultations," *Icarus*, Vol. 129, No. 1, 1997, pp. 178–201. https://doi.org/10.1006/icar.1997.5757, URL https://doi.org/10.1006/icar.1997.5757. 17, 19

[34] Elliot, J. L., Strobel, D. F., Zhu, X., Stansberry, J., Wasserman, L. H., and Franz, O. G., "The thermal structure of Triton's middle atmosphere," *Icarus*, Vol. 143, No. 2, 2000, pp. 425–428. https://doi.org/10.1006/icar.1999.6312, URL https://doi.org/10.1006/icar.1999.6312. 17, 19

[35] Lellouch, E., De Béh, C., Sicardy, B., Ferron, S., and Käl, H. U., "Detection of CO in Triton's atmosphere and the nature of surface-atmosphere interactions," *Astronomy and Astrophysics*, Vol. 512, 2010, p. L8. https://doi.org/10.1051/0004-6361/201014339, URL https://doi.org/10.1051/0004-6361/201014339.

[36] Elliot, J. L., Person, M. J., and Qu, S., "Analysis of Stellar Occultation Data. II. Inversion, with Application to Pluto and Triton," *The Astronomical Journal*, Vol. 126, No. 2, 2003, pp. 1041–1079. https://doi.org/10.1086/375546, URL http://dx.doi.org/10.1086/375546. 19

[37] Oliveira, J. M., Sicardy, B., Gomes-Jú, A. R., Ortiz, J. L., Strobel, D. F., Bertrand, T., Forget, F., Lellouch, E., Desmars, J., Bérd, D., Doressoundiram, A., Lecacheux, J., Leiva, R., Meza, E., Roques, F., Souami, D., Widemann, T., Santos-Sanz, P., Morales, N., Duffard, R., Fernáez-Valenzuela, E., Castro-Tirado, A. J., Braga-Ribas, F., Morgado, B. E., Assafin, M., Camargo, J., Vieira-Martins, R., Benedetti-Rossi, G., Santos-Filho, S., Banda-Huarca, M. V., Quispe-Huaynasi, F., Pereira, C. L., Rommel, F. L., Margoti, G., Dias-Oliveira, A., Colas, F., Berthier, J., Renner, S., Hueso, R., Péz-Hoyos, S., Sanchez-Lavega, J. F., Agustíand Rojas, Beisker, W., Kretlow, M., Herald, D., Gault, D., Bath, K.-l., Bode, H.-j., Bredner, E., Guhl, K., Haymes, T. V., Hummel, E., Kattentidt, B., KlöO., Pratt, A., Thome, B., Avdellidou, C., Gazeas, K., Karampotsiou, E., Tzouganatos, L., Kardasis, E., Christou, A. A., Xilouris, E. M., Alikakos, I., Gourzelas, A., Liakos, A., Charmandaris, V., Jelík, M., .trobl, J., Eberle, A., Rapp, K., Gäken, B., Klemt, B., Kowollik, S., Bitzer, R., Miller, M., Herzogenrath, G., Frangenberg, D., Brandis, L., Pü., Perdelwitz, V., Piehler, G. M., Riepe, P., Von Poschinger, K., Baruffetti, P., Cenadelli, D., Christille, J.-m., Ciabattari, F., Di Luca, R., Alboresi, D., Leto, G., Sanchez, R. Z., Bruno, P., Occhipinti, G., Morrone, L., Cupolino, L., Noschese, A., Vecchione, A., Scalia, C., and Lo Savio, R., "Constraints on the structure and seasonal variations of Triton.s atmosphere from the 5 October 2017 stellar occultation

and previous observations," *Astronomy and Astrophysics*, Vol. 659, 2022, p. A136. https://doi.org/10.1051/0004-6361/202141443, URL https://doi.org/10.1051/0004-6361/202141443. 18, 19

[38] Yuan, Y., Zhang, C., Fan, L., Fu, X., Fu, Y., Bai, C. H., Gao, X., and Wang, Y., "New constraints on Triton's atmosphere from the 6 October 2022 stellar occultation," *Astronomy and Astrophysics (Print)*, 2024. https://doi.org/10.1051/0004-6361/202348460, URL https://doi.org/10.1051/0004-6361/202348460. 17

[39] Strobel, D. F., and Zhu, X., "Comparative planetary nitrogen atmospheres: Density and thermal structures of Pluto and Triton," *Icarus*, Vol. 291, 2017, pp. 55–64. https://doi.org/10.1016/j.icarus.2017.03.013, URL https://doi.org/10.1016/j.icarus.2017.03.013. 17, 18, 20, 29, 42, 69

[40] Ingersoll, A. P., "Dynamics of Triton's atmosphere," *Nature (London)*, Vol. 344, No. 6264, 1990, pp. 315–317. https://doi.org/10.1038/344315a0, URL https://doi.org/10.1038/344315a0. 17

[41] Bertrand, T., Lellouch, E., Holler, B. J., Young, L. A., Schmitt, B., Oliveira, J. M., Sicardy, B., Forget, F., Grundy, W. M., Merlin, F., Vangvichith, M., Millour, E., Schenk, P., Hansen, C. J., White, O. L., Moore, J. M., Stansberry, J., Oza, A., Dubois, D., Quirico, E., and Cruikshank, D. P., "Volatile transport modeling on Triton with new observational constraints," *Icarus*, Vol. 373, 2022, p. 114764. https://doi.org/10.1016/j.icarus.2021.114764, URL https://doi.org/10.1016/j.icarus.2021.114764. 18

[42] Sicardy, B., Tej, A., Gomes-Junior, A. R., Romanov, F. D., Bertrand, T., Ashok, N. M., Lellouch, E., Morgado, B. E., Assafin, M., Desmars, J., Camargo, J. I. B., Kilic, Y., Ortiz, J. L., Vieira-Martins, R., Braga-Ribas, F., Ninan, J. P., Bhatt, B. C., Kumar, S. P., Swain, V., Sharma, S., Saha, A., Ojha, D. K., Pawar, G., Deshmukh, S., Deshpande, A., Ganesh, S., Jain, J. K., Mathew, S. K.,

Kumar, H., Bhalerao, V., Anupama, G. C., Barway, S., Brandeker, A., Floren, H. G., Olofsson, G., Bruno, G., Mao, Y. M., Ye, R. H., Zou, Q. Y., Sun, Y. K., Shen, Y. Y., Zhao, J. Y., Grishin, D. N., Romanova, L. V., Marchis, F., Fukui, K., Kukita, R., Benedetti-Rossi, G., Santos-Sanz, P., Dhyani, N., Gokhale, A., and Kate, A., "Constraints on Triton atmospheric evolution from occultations: 1989-2022," *arXiv (Cornell University)*, 2024. https://doi.org/10.48550/arxiv.2402.02476, URL https://arxiv.org/abs/2402.02476. 18

[43] Gurrola, E. M., *Interpretation of radar data from the icy Galilean satellites and Triton*, Stanford University, 1995. 19

[44] Ramsey, P., "A Preliminary Investigation of Aerogravity Assist at Triton for Capture into Orbit About Neptune," , 04 2006. 18, 24

[45] Elliot, J., "The Prediction and Observation of the 1997 July 18 Stellar Occultation by Triton: More Evidence for Distortion and Increasing Pressure in Triton's Atmosphere," *Icarus*, Vol. 148, No. 2, 2000, pp. 347–369. https://doi.org/10.1006/icar.2000.6508. 18

[46] Benne, B., Dobrijevic, M., CavaliéThibault, Loison, J.-C., and Hickson, K. M., "A photochemical model of Triton.s atmosphere paired with an uncertainty propagation study," *Astronomy and Astrophysics*, Vol. 667, 2022, p. A169. https://doi.org/10.1051/0004-6361/202244447, URL https://doi.org/10.1051/0004-6361/202244447. 18

[47] Hirschel, E. H., *Basics of Aerothermodynamics*, Springer, 2015. https://doi.org/10.1007/978-3-319-14373-6, URL https://doi.org/10.1007/978-3-319-14373-6. 21

[48] Terrier, D., "NASA STMD Strategic Technology Investment Plan," 2017. URL https://www.nasa.gov/sites/default/files/atoms/files/2017-8-1_stip_final-508ed.pdf. 23

[49] Cassell, A., Cheatwood, N., Hughes, S., Kazemba, C., and Swanson, G., "Deployable entry vehicles for future science and exploration missions," *Bulletin of the AAS*, Vol. 53, No. 4, 2021. https://doi.org/10.3847/25c2cfeb.ed731e3c, URL https://doi.org/10.3847/25c2cfeb.ed731e3c. 23, 35

[50] Nebiker, F. R., "Feasibility Study of an Inflatable Type Stabilization and Deceleration System for High Altitude and High Speed Recovery," Tech. Rep. WADD TR 60-182, 12 1961. 23

[51] Hall, J. L., "A review of ballute technology for planetary aerocapture," *4th IAA Conference of Low Cost Planetary Missions*, 2000. 23

[52] Park, C., "A survey of aerobraking orbital transfer vehicle design concepts," *54th AIAA Aerospace Sciences Meeting*, 1987. https://doi.org/10.2514/6.1987-514, URL https://doi.org/10.2514/6.1987-514. 23

[53] Brandeau, E., Gallon, J. C., Witkowski, A., and Tanner, C. L., *Deployment of the 30.5 meter Parachute on the Supersonic Flight Dynamics Test*, 2016. https://doi.org/10.2514/6.2015-2129, URL https://arc.aiaa.org/doi/abs/10.2514/6.2015-2129. 24

[54] Dutta, S., Karlgaard, C. D., Tynis, J. A., O'Farrell, C., Sonneveldt, B. S., Queen, E. M., Bowes, A. L., Leylek, E. A., and Ivanov, M. C., "Advanced Supersonic Parachute Inflation Research Experiment Preflight trajectory modeling and Postflight Reconstruction," *Journal of Spacecraft and Rockets*, Vol. 57, No. 6, 2020, pp. 1387–1407. https://doi.org/10.2514/1.a34706, URL https://doi.org/10.2514/1.a34706.

[55] Muppidi, S., Norman, J. W. V., O'Farrell, C., Bose, D., and Clark, I. G., *Computational Analysis and Post-Flight Validation of Ballute Aerodynamics*, ???? https://doi.org/10.2514/6.2015-2116, URL https://arc.aiaa.org/doi/abs/10.2514/6.2015-2116. 24

[56] McRonald, A. D., "A Light-Weight Inflatable Hypersonic Drag Device for Planetary Entry," Tech. Rep. 20000074083, 3 2000. 24

[57] Ramsey, P., and Lyne, J. E., "An Investigation of Titan Aerogravity Assist for Capture into Orbit About Saturn," *Astrodynamics Specialists Conference*, American Institute of Aeronautics and Astronautics, 2003. URL https://www.researchgate.net/publication/364396621_AAS_03-644_AN_INVESTIGATION_OF_TITAN_AEROGRAVITY_ASSIST_FOR_CAPTURE_INTO_ORBIT_ABOUT_SATURN.

[58] Moss, J. N., "Direct Simulation Monte Carlo Simulations of ballute aerothermodynamics under hypersonic rarefied conditions," *Journal of Spacecraft and Rockets*, Vol. 44, No. 2, 2007, pp. 289–298. https://doi.org/10.2514/1.22706, URL https://doi.org/10.2514/1.22706. 24

[59] Otsu, H., and Abe, T., "Effect of the Shock Interaction on the Attitude Stability of the Toroidal Ballute for Reentry Vehicle," *29th International Symposium on Shock Waves 1*, edited by R. Bonazza and D. Ranjan, 2015, p. 575. https://doi.org/10.1007/978-3-319-16835-7_91. 24

[60] Gates, K. L., and Longuski, J. M., "Aerocapture ballutes versus aerocapture tethers for exploration of the solar system," *Journal of Spacecraft and Rockets*, Vol. 47, No. 4, 2010, pp. 590–596. https://doi.org/10.2514/1.46603, URL https://doi.org/10.2514/1.46603. 25

[61] Kelly, C. L., "Physics, Performance, and Applications of Plasma Aerocapture," Ph.D. thesis, 2021. URL https://utk.idm.oclc.org/login?url=https://www.proquest.com/dissertations-theses/physics-performance-applications-plasma/docview/2628280676/se-2, copyright - Database copyright ProQuest LLC; ProQuest does not claim copyright in the individual underlying works; Last updated - 2023-03-08. 25

[62] Nguyen, D. N., Dutta, S., Green, J. S., and Ali, H. K., "Performance Analysis of Magnetohydrodynamic Drag Modulation for Actively Controlled Aerocapture at Neptune," *2024 AAS/AIAA Astrodynamicist Specialist Conference*, 2024. URL https://ntrs.nasa.gov/api/citations/20240009435/downloads/AAS_AIAA_2024_DannyNguyen.pdf. 25

[63] Moses, R. W., and Green, J. S., "Magnetohydrodynamics Aerocapture System for Enabling Fast Larger Planetary Science and Human Exploration Missions," *21st International Planetary Probe Workshop*, 2024. URL https://ntrs.nasa.gov/citations/20240005756. 25

[64] Moses, R. W., "Advanced Aerocapture System For Enabling Fast-Larger Planetary Science and Human Exploration Missions to Worlds with Atmospheres," *18th International Planetary Probe Workshop*, 2021. URL https://ntrs.nasa.gov/citations/20240005756. 25

[65] Korzun, A. M., Hollis, B. R., Wise, A. J., Liechty, D. S., and Karlgaard, C. D., "Aerodynamic Performance of the Low-Earth Orbit Flight Test of an Inflatable Decelerator (LOFTID) Technology Demonstration Mission," *AIAA SciTech 2024 Forum*, 2024. https://doi.org/10.2514/6.2024-1500, URL https://doi.org/10.2514/6.2024-1500. 25, 26, 27, 30, 40

[66] Hollis, B. R., Wise, A. J., Liechty, D. S., Korzun, A. M., Thompson, K. B., Rodrigues, N. S., and Rieken, E., "Aerothermodynamic Analyses for the LOFTID Technology Demonstration Mission," *AIAA SciTech 2024 Forum*, 2024. https://doi.org/10.2514/6.2024-1498, URL https://doi.org/10.2514/6.2024-1498. 25, 26, 27, 38

[67] Karlgaard, C. D., Deshmukh, R. G., Dutta, S., Fine, A. L., Hollis, B. R., and Korzun, A. M. a., "Trajectory Trconstruction of the Low-Earth Orbit Flight Test of an Inflatable Decelerator," *AIAA SciTech 2024 Forum*, 2024. https:

//doi.org/10.2514/6.2024-1502, URL https://doi.org/10.2514/6.2024-1502. 26, 39

[68] Brauer, G. L., "Program to Optimize Simulated Trajectories (POST). Volume 3: Programmer's manual," *Martin Marietta Corp. Report*, 1975. 28

[69] Bauer, G. L., Cornick, D. E., Habeger, A. R., Petersen, F. M., and Stevenson, R., "Program to Optimize Simulated Trajectories (POST). Volume 1: Formulation Manual," Tech. Rep. NASA CR-132689, 4 1975. URL https://ntrs.nasa.gov/api/citations/19750024074/downloads/19750024073.pdf. 31, 95

[70] Sforza, P. M., *Spacecraft Flight Mechanics*, Elsevier, 2016, Chap. 8. URL https://app.knovel.com/hotlink/khtml/id:kt010R2J35/manned-spacecraft-design/spacecraft-flight-mechanics. 35

[71] Sutton, K., and Graves, R. A., "A general stagnation-point convective heating equation for arbitrary gas mixtures," Tech. Rep. NASA TR R-376, 11 1971. URL https://ntrs.nasa.gov/api/citations/19720003329/downloads/19720003329.pdf. 36, 37

[72] Sutton, K., and Hartung, L. C., "Equilibrium radiative heating tables for Earth entry," *NASA STI/Recon Technical Report N*, Vol. 90, 1990, pp. 23675–. URL https://ntrs.nasa.gov/api/citations/19900014359/downloads/19900014359.pdf. 37, 44

[73] Dillman, R. A., DiNonna, J. M., Bodkin, R. J., Hughes, S. J., Cheatwood, F. M., Blakeley, H., Akamine, R. L., and Bowes, A., "Planned Orbital Flight Test of a 6m HIAD," *15th International Planetary Probe Workshop*, 2018. 40

[74] Lyne, J. E., Brisby, J. D., and Carroll, A., "Hypersonic Maneuvers in Planetary Mission Design," *11th Edition of the Jornadas da Engenharia Fisica (JEF)*, 2025. 45

[75] Lyne, J. E., "Physiologically constrained aerocapture for manned Mars missions," *STIN*, Vol. 93, 1992, pp. 12720–. URL https://ntrs.nasa.gov/archive/nasa/casi.ntrs.nasa.gov/19930003532.pdf. 59

[76] Bate, R. R., Mueller, D. D., White, J. E., and Saylor, W. W., *Fundamentals of Astrodynamics*, Dover Publications, 2020. 96

Appendix A

Turn Angles

A.1 Pure Gravitation Assist

A gravitational assist, sometimes referred to as a gravitational slingshot, can be an important maneuver when planning for interplanetary trajectories. The maneuver is performed by spacecraft passing near a planet and using the planet's gravitational potential to adjust the vehicle's velocity vector. This method was famously used by the Voyager 2 spacecraft at multiple points during its flight to interstellar space. Figure A.1 shows what a trajectory might look like for a 2-D, gravitational assist occurring along the planet's equator.

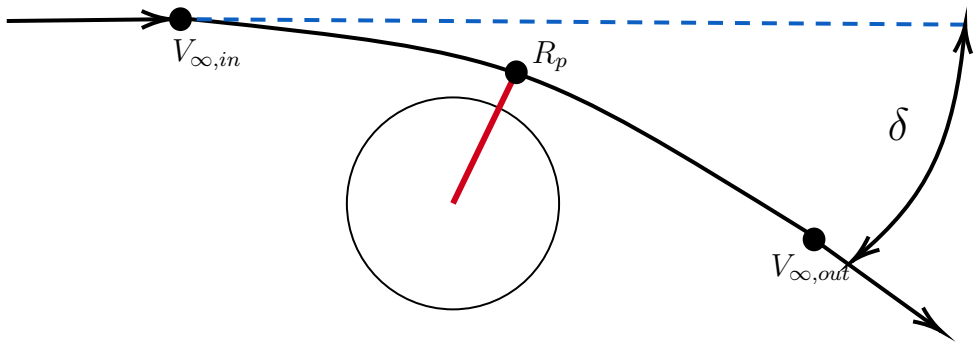


Figure A.1: Turn angle diagram from pure gravitational assist.

In Fig. A.1, the curved, solid, black line shows the trajectory of the vehicle during the flyby, the dashed, blue line shows what the trajectory would have been without the existence of the planet's gravity-well, $V_{\infty,in}$ signifies the velocity at a point infinitely far away, typically at the edge of the planet's sphere of influence, on approach, R_p is the radius of periapse for the hyperbolic trajectory, $V_{\infty,out}$ is the velocity at a point infinitely far away, again at the edge of the sphere of influence, on departure, and δ is the turn angle of the velocity vector.

The achievable turn angle during a gravitational assist can be found by employing Eq. A.1

$$\delta = 180 - 2cos^{-1}\left(\left[1 + \frac{{V_\infty}^2 R_p}{\mu}\right]^{-1}\right) \tag{A.1}$$

where δ is the turn angle, V_∞ is the hyperbolic excess speed as seen by the assisting planet, R_p is the intended periapse radius, and μ is the planet's gravitational parameter. This equation assumes that the approach and departure velocity vectors are coplanar, periapse radius is at least the radius of the target body, and no losses for the trajectory due to drag. This can be very useful in early stages of mission planning when determining a trajectory's feasibility. A contour plot showing turn angle as a function of approach velocity and altitude from Triton's surface is shown in Fig. A.2.

A.2 Aerogravity Assist

A.2.1 2-D, Equatorial Plane

If the pure gravitational assist does not provide adequate adjustment of the velocity vector, the planet's atmosphere can be leveraged to further adjust the turn angle. However, the calculation of the turn angle is no longer as straight-forward because the radius of periapse changes during the atmospheric trajectory. In the case of a non-lifting ballistic entry, atmospheric drag dissipates energy causing a reduction in

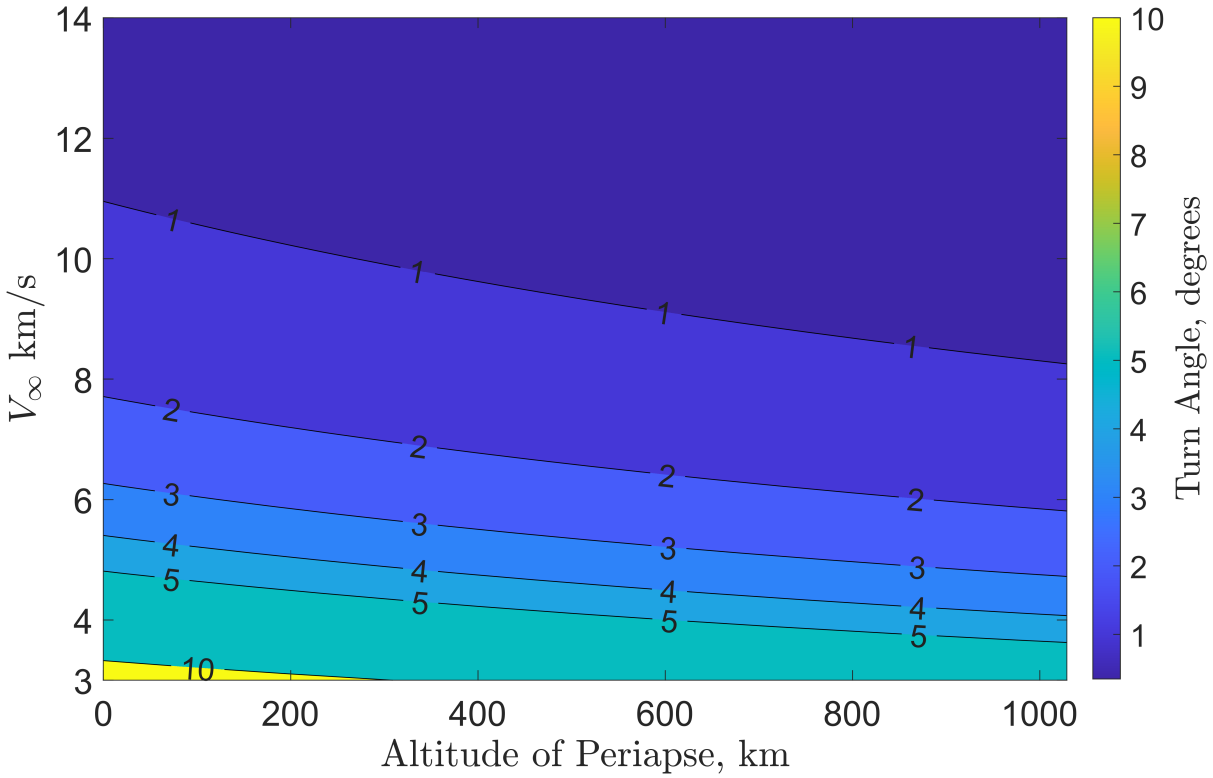


Figure A.2: Contour plot of turn angle (δ) for $h = [0, 1029]\, km$ and $V_\infty = [3, 14]\, \frac{km}{s}$.

periapse radius. The true anomaly at multiple points along the trajectory are needed along with the direction of the radius of periapse for the inbound and outbound legs of the trajectory and lastly, for the 2-D equatorial trajectory, the longitude when entering and exiting the atmospheric interface. Figure A.3 shows a generic, equatorial aerogravity assist where the solid black line represents the vehicle trajectory, $V_{\infty,in}$ and $V_{\infty,out}$ are the inbound and outbound velocity vectors at the edge of the sphere of influence, θ_{En}, ν_{En}, ν_{Ex}, and θ_{Ex} are the longitude and true anomaly when entering and exiting the atmospheric interface, $R_{p,in}$ and $R_{p,out}$ are the direction pointing to the radius of periapse as calculated by the inbound and outbound conditions at the sphere of influence. The true anomaly at atmospheric entry, ν_{En}, is the angle measured from the vector pointing towards the initial radius of periapse, $R_{p,in}$, to a line drawn through the center of the planet, parallel to the outbound velocity vector (red-dashed line). Likewise, ν_{Ex} is measured from the vector point towards the final radius of periapse, $R_{p,out}$, to a line drawn through the center of the planet parallel to the inbound velocity vector (green-dashed line). All of these components combined form Eq. A.2. Again, this expression for turn angle during an AGA assumes a 2-D, equatorial trajectory about the planet.

$$\delta = |\nu_{\infty,i}| - |\nu_{En}| \; + \; (\theta_{Ex} - \theta_{En}) \; + |\nu_{\infty,o}| - |\nu_{Ex}| \; - \; 180 \tag{A.2}$$

A.2.2 Extended to 3-D

Equation A.2 can be extended to 3-D by recognizing that the term $(\theta_{Ex} - \theta_{En})$ is just the central angle between any two points on a sphere. If we let that central angle be written as variable ψ, the central angle can be found using the spherical law of cosines shown in Eq. A.3

$$cos(\psi) = cos(\phi_{En} - \phi_{Ex})cos(\theta_{En})cos(\theta_{Ex}) + sin(\theta_{En})sin(\theta_{Ex}) \tag{A.3}$$

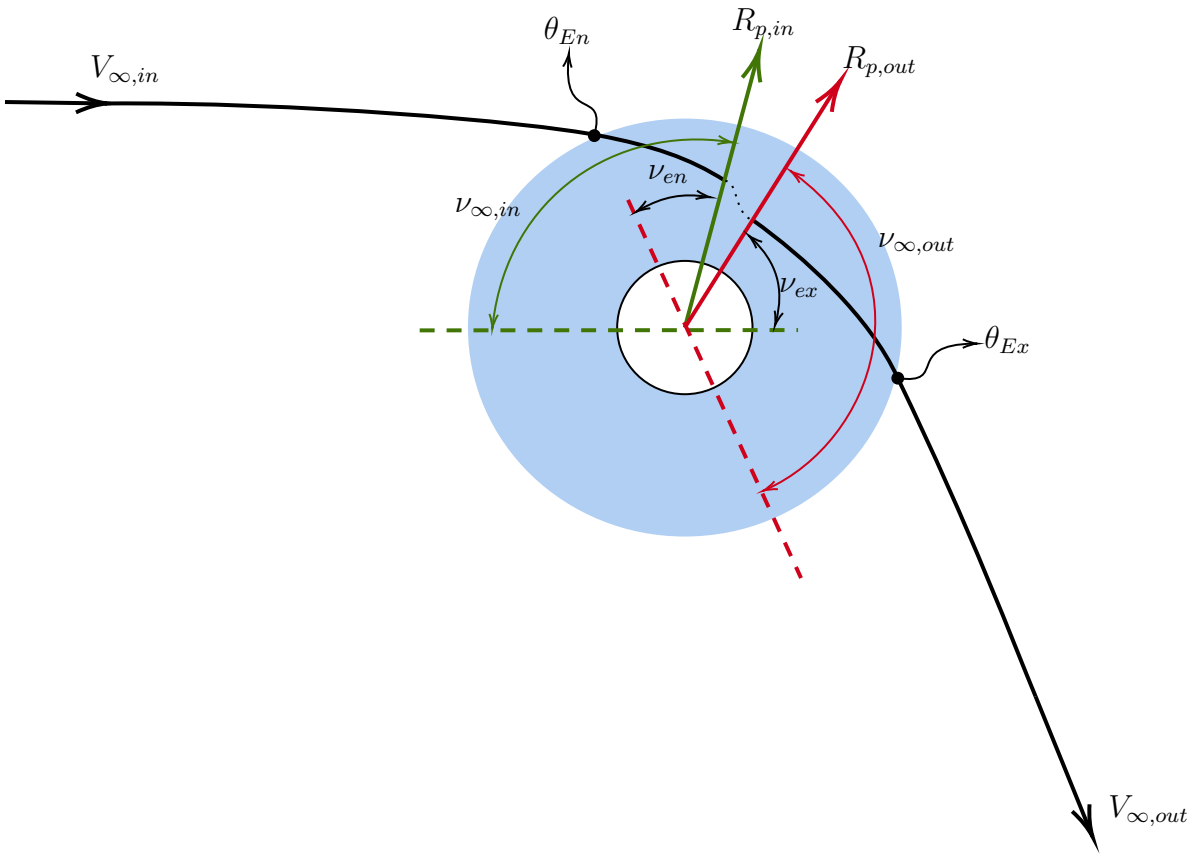


Figure A.3: Turn angle diagram from aerogravity assist.

where ϕ_{En} and ϕ_{Ex} are the latitudes of atmospheric entry and exit while θ_{En} and θ_{Ex} are the longitudes of atmospheric entry and exit. Substituting the arccos of Eq. A.3 for $(\theta_{Ex} - \theta_{En})$ in Eq. A.2 yields Eq. A.4 which allows the turn angle to be calculated for an unpowered trajectory using the planetocentric latitude and longitude.

$$\begin{aligned} \delta = |\nu_{\infty,i}| - |\nu_{En}| \ + |\nu_{\infty,o}| - |\nu_{Ex}| \ - \ 180 \ + \\ + \ cos^{-1}\left[cos(\phi_{En} - \phi_{Ex})cos(\theta_{En})cos(\theta_{Ex}) + sin(\theta_{En})sin(\theta_{Ex})\right] \end{aligned} \tag{A.4}$$

Appendix B

Arrival Velocity

B.1 Neptune and Triton Arrival Velocities

Table B.1: Probe Velocities at Arrival to Neptune System With Respect to Neptune

Velocities in km/s

Excess Speed V_∞	Inertial $V_{@R_{N,Eq}}$ Eq. B.1	$V_{Min@Atmo,En}$ Eq. B.2	$V_{Max@Atmo,En}$ Eq. B.3
4.1	23.85	21.17	26.53
5.1	24.04	21.36	26.72
6.1	24.28	21.60	26.96
7.1	24.55	21.87	27.23
8.1	24.85	22.17	27.53
9.1	25.20	22.52	27.88
10.1	25.58	22.90	28.26
11.1	25.99	23.31	28.67
12.1	26.43	23.75	29.11
13.1	26.90	24.22	29.58
14.1	27.40	24.72	30.08

Table B.2: Probe Velocities at Arrival to Neptune System With Respect to Triton

Velocities in km/s

Inertial $V_{@R_{Tr,Orb}}$ Eq. B.4	$V_{\infty,Min}$ Eq. B.5	$V_{\infty,Max}$ Eq. B.6	$V_{Min@Atmo,En}$ Eq. B.7	$V_{Max@Atmo,En}$ Eq. B.8
7.44	3.05	11.83	3.24	11.88
8.03	3.64	12.42	3.81	12.47
8.70	4.31	13.09	4.45	13.14
9.43	5.04	13.82	5.16	13.86
10.21	5.82	14.60	5.92	14.64
11.02	6.63	15.41	6.72	15.44
11.86	7.47	16.25	7.55	16.28
12.72	8.33	17.11	8.40	17.14
13.60	9.21	17.99	9.27	18.02
14.50	10.11	18.89	10.17	18.92
15.41	11.02	19.80	11.07	19.83

$$V_{@R_{N,Eq}} = \sqrt{V_{\infty}^2 + \frac{2\mu_N}{R_N}} \tag{B.1}$$

$$V_{Min@Atmo,En} = V_{@R_{N,Eq}} - V_{N_{Rotational}} \tag{B.2}$$

$$V_{Max@Atmo,En} = V_{@R_{N,Eq}} + V_{N_{Rotational}} \tag{B.3}$$

$$V_{@R_{Tr,Orb}} = \sqrt{V_{\infty}^2 + \frac{2\mu_N}{R_{Tr,Orb}}} \tag{B.4}$$

$$V_{\infty,Min} = V_{@R_{Tr,Orb}} - V_{Tr,Orb} \tag{B.5}$$

$$V_{\infty,Max} = V_{@R_{Tr,Orb}} + V_{Tr,Orb} \tag{B.6}$$

$$V_{Min@Atmo,En} = \sqrt{V_{\infty,Min} + \frac{2\mu_{Tr}}{R_{Tr,Eq} + H_{Atmo}}} \tag{B.7}$$

$$V_{Max@Atmo,En} = \sqrt{V_{\infty,Max} + \frac{2\mu_{Tr}}{R_{Tr,Eq} + H_{Atmo}}} \tag{B.8}$$

Appendix C

Code Workflow

The initial state vector for the simulations requires the vehicle position in the planetocentric inertial reference frame supplied in polar coordinates as altitude, geocentric latitude, and inertial longitude. The inertial velocity is also input in polar coordinates relative to the local horizontal plane supplied as velocity magnitude, inertial flight path angle, and azimuthal angle. The position and velocity are then converted to cartesian coordinates using C.1 and Eq. C.2

$$\vec{R_I} = R_I \begin{bmatrix} cos(\phi_c)cos(\theta_I) \\ cos(\phi_c)sin(\theta_I) \\ sin(\phi_c) \end{bmatrix} \tag{C.1}$$

$$\vec{V_I} = V_I \begin{bmatrix} cos(\gamma_I)cos(Az_I) \\ cos(\gamma_I)sin(Az_I) \\ -sin(\gamma_I) \end{bmatrix} \tag{C.2}$$

where R_I is the radial distance from the planet center, ϕ_c is the geocentric latitude, θ_I is the inertial longitude, V_I is the velocity magnitude, γ_I is the inertial flight path angle, and Az_I is the inertial azimuthal angle.

The equations of motion used for propagating the trajectory through the atmosphere are shown in Eq. C.3 and Eq. C.4

$$\dot{\vec{R}}_I = \vec{V}_I \tag{C.3}$$

$$\dot{\vec{V}}_I = \vec{A}_I + \vec{G}_I \tag{C.4}$$

where $\dot{\vec{R}}_I$ is the derivative of the position vector, $\vec{V}_I$ is the inertial velocity vector, $\dot{\vec{V}}_I$ is the derivative of the velocity vector, $\vec{A}_I$ is the vehicle acceleration from aerodynamic forces, and $\vec{G}_I$ is the inertial acceleration from gravity. The acceleration from the aerodynamic forces are calculated in the body reference frame using Eq. C.5, Eq. C.6, and Eq. C.7

$$\begin{bmatrix} C_A \\ C_N \end{bmatrix} = \begin{bmatrix} cos(\alpha) & -sin(\alpha) \\ sin(\alpha) & cos(\alpha) \end{bmatrix} \begin{bmatrix} C_D \\ C_L \end{bmatrix} \tag{C.5}$$

$$\vec{F} = \frac{1}{2}\rho_\infty A V_A^2 \begin{bmatrix} -C_A \\ C_Y \\ -C_N \end{bmatrix} \tag{C.6}$$

$$\vec{A_B} = \frac{\vec{F}}{m_{veh}} \tag{C.7}$$

where C_A, C_Y, and C_N are the axial, yaw, and normal aerodynamic force coefficients, C_D and C_L are the coefficients of drag and lift, α is the vehicle angle of attack, $\vec{F}$ is the calculated aerodynamic force vector, ρ_∞ is the freestream density, V_A is the magnitude of the atmosphere relative velocity, A is the vehicle reference surface area, m_{veh} is the vehicle mass and $\vec{A_B}$ is the resulting acceleration vector in the body frame. The series of rotation matrices needed to convert the body frame accelerations to inertial can be found in the POST formulation manual[69]. These equations of motion are numerically integrated using a 4th Order Runge Kutta algorithm until the simulation reaches a desired termination condition (surface impact, maximum

flight time, maximum iteration count, atmospheric exit). Orbital parameters are calculated at the beginning and end of the trajectory using the formulations found in any orbital mechanics textbook[76].

Vita

Wanting more than rural Kentucky had to offer, after high-school, Jakob Brisby moved to Knoxville, Tennessee where he attended the University of Tennessee. Jakob earned undergraduate degrees in both aerospace engineering and mechanical engineering. He then decided to remain at the University of Tennessee to pursue a master of science degree in aerospace engineering with a focus on atmospheric entry of meteors. Immediately following the completion of his master's degree, Jakob took a position Applied Research Associates in Albuquerque, New Mexico where he was a member of a multi-disciplinary group of scientists and engineers developing state-of-the-art software performing analysis focusing on blast environments. However, the desire to achieve a Doctor of Philosophy in Aerospace Engineering lead him back to the University of Tennessee where he focused on high-speed atmospheric trajectories while he maintained his position as part of the computational physics group at Applied Research Associates.